

Utah State University

DigitalCommons@USU

All Graduate Theses and Dissertations

Graduate Studies

5-2012

A 2D Finite Element/1D Fourier Solution to the Fokker-Planck Equation

Joseph Andrew Spencer
Utah State University

Follow this and additional works at: <https://digitalcommons.usu.edu/etd>



Part of the [Physics Commons](#)

Recommended Citation

Spencer, Joseph Andrew, "A 2D Finite Element/1D Fourier Solution to the Fokker-Planck Equation" (2012).
All Graduate Theses and Dissertations. 1257.
<https://digitalcommons.usu.edu/etd/1257>

This Dissertation is brought to you for free and open access by the Graduate Studies at DigitalCommons@USU. It has been accepted for inclusion in All Graduate Theses and Dissertations by an authorized administrator of DigitalCommons@USU. For more information, please contact digitalcommons@usu.edu.



A 2D FINITE ELEMENT/1D FOURIER SOLUTION
TO THE FOKKER-PLANCK EQUATION

by

Joseph Andrew Spencer

A dissertation submitted in partial fulfillment
of the requirements for the degree

of

DOCTOR OF PHILOSOPHY

in

Physics

Approved:

Eric D. Held
Major Professor

W. Farrell Edwards
Committee Member

James T. Wheeler
Committee Member

Robert E. Spall
Committee Member

Charles G. Torre
Committee Member

Mark R. McLellan
Vice President for Research and
Dean of the School of Graduate Studies

UTAH STATE UNIVERSITY
Logan, Utah

2012

Copyright © Joseph Andrew Spencer 2012

All Rights Reserved

ABSTRACT

A 2D finite element/1D Fourier solution
to the Fokker-Planck equation

by

Joseph Andrew Spencer, Doctor of Philosophy
Utah State University, 2012

Major Professor: Dr. Eric D. Held
Department: Physics

A method is proposed for a 2D finite element/1D Fourier solution of the Fokker-Planck (FP) equation describing Coulomb collisions between particles in a fully ionized, spatially homogeneous plasma. A full 3D velocity space dependence is maintained using cylindrical coordinates $(v_{\parallel}, v_{\perp}, \gamma)$. When a magnetic field exists, v_{\parallel} is aligned with it and γ corresponds to gyroangle. Distribution functions are approximated by a Fourier representation in the azimuthal angle, γ , and by a 2D finite element representation in the parallel and perpendicular directions. Two different techniques are used to linearize the FP collision operator: one is referred to as the δf approach and the other is called the Chapman-Enskog-like (CEL) approach. The δf approach uses the test particle operator, whereas the CEL approach uses a combination of fluid equations with a kinetic equation employing both the test particle and field operators. The finite element/Fourier treatment is discussed in detail and applied to both linearization schemes for a number of test applications. The FP equation can be solved in a fully implicit manner allowing large, stable time steps and simulations that arrive quickly at equilibrium solutions. The results of several test problems are discussed, including a calculation of the plasma resistivity/conductivity, the heating and cooling of a test particle distribution, the slowing down of a beam of test particles, the acquisition of

a perpendicular flow for a nonflowing Maxwellian test distribution, and thermalization of plasma species with different temperatures. Robust convergence upon refinement of the finite element/Fourier representation is highlighted.

(122 pages)

PUBLIC ABSTRACT

A 2D Finite Element/1D Fourier Solution
to the Fokker-Planck Equation

Joseph Andrew Spencer

Plasma, the fourth state of matter, is a gas in which a significant portion of the atoms are ionized. It is estimated that more than 99% of the material in the visible universe is in the plasma state. The process that stars, including our sun, combine atomic nuclei and produce large amounts of energy is called thermonuclear fusion. It is anticipated future energy demands will be met by large terrestrial devices harnessing the energy of nuclear fusion. A gas hot enough to produce the number of atomic collisions needed for fusion is necessarily in the plasma state. Therefore, plasmas are of great interest to researchers studying nuclear fusion. Stars are massive enough that the gravitational attraction heats and confines the plasma. Gravitational confinement cannot be used to confine fusion plasmas on Earth. Material containers cause cooling, which prevent a plasma from maintaining the high temperature needed for fusion. Fortunately plasmas have electrical properties, which allow them to be controlled by strong magnetic fields.

Although serious research into controlled thermonuclear fusion began over 60 years ago, only a couple of man-made devices are even close to obtaining more energy from fusion than is put into them. One difficulty lies in understanding the physics of particle collisions. A relative few particle collisions result in the fusion of atomic nuclei, while the vast majority of collisions are understood in terms of the electrostatic force between particles. My work has been to create an a computer code, which can be executed in parallel on supercomputers, to quickly and accurately calculate the evolution of a plasma due to particle collisions. This work explains the physics and mathematics underlying our code, as well as several tests which demonstrate the code is working as expected.

I am very grateful to many people who have contributed to this project. First, I am grateful to my major professor, Eric Held, for providing encouragement, countless hours of time and thoughtful advice, which has led to the accomplishment of many of my goals. He has selflessly given his time in personally educating me, looking for ways to challenge me, and furthering my professional development. His concern for me has led to an employment opportunity, which matches my professional and personal interests and for which I am extremely grateful and excited to begin.

I am also indebted to Jeong-Young Ji, who spent many hours with me answering questions and teaching me about his research, further broadening my view of the subject of plasma physics. Dr. Ji made sure that I received the best education and provided me with powerful advice and examples regarding research methods. I am thankful to my committee members, James Wheeler, Farrell Edwards, Charles Torre, and Robert Spall, for encouragement and valuable advice. I am especially grateful to Dr. Wheeler, who sacrificed many hours of his time while I was just beginning graduate school to teach me about his research. His tutelage engendered autonomy and gave me a strong mathematical background. I appreciate all the educators who put their time into my academic development. I also thank my parents who cultivated my natural creativity and scientific curiosity. I especially thank my wife, Melissa, who has been my companion and supporter all along this journey.

Although the finite element method has not been previously used to solve for the velocity dependent distribution functions of a plasma, all of the machinery required to implement a FEM/Fourier solution to the plasma kinetic equation was provided by the preexisting subroutines found in the NIMROD code. I thank the NIMROD team for allowing the NIMROD code to be adapted in this way. This research is supported by the U.S. DOE under Grant No. DE-FG02-04ER54746.

Joseph Andrew Spencer

CONTENTS

	Page
ABSTRACT	iii
PUBLIC ABSTRACT	v
ACKNOWLEDGMENTS	vi
LIST OF TABLES	ix
LIST OF FIGURES	x
INDEX OF SYMBOLS	xiii
CHAPTER	
1. INTRODUCTION	1
2. THE FOKKER-PLANCK EQUATION	8
The physics of the Fokker-Planck equation	8
Linearizing the Fokker-Planck equation	19
3. NUMERICAL SCHEME	26
Time-discretization	26
A 2D finite element/1D Fourier representation	29
Weak form	39
4. THE TEST PARTICLE OPERATOR	46
Resistivity of an unmagnetized Lorentz plasma	46
Thermalization of test particles	48
Tenuous beam of test particles	55
Perpendicular flow	57
Chapter summary	62
5. THE FIELD OPERATOR	64
Spitzer conductivity	64
Thermalization problem	84
6. CONCLUSION AND FUTURE WORK	88

	viii
REFERENCES	93
APPENDIX.....	95
CURRICULUM VITAE	103

LIST OF TABLES

Table		Page
3.1	Diagram of staggered update of the CEL approach	29
4.1	p -type refinement of the electrical resistivity, η_L , of a Lorentz plasma in response to an electric field, $E = 10^{-5}$ V/m, and the mean pointwise error, ε , cf. Eq. (4.5)	48
4.2	Maintaining a constant cell size, but increasing the velocity domain shows improved conservation in n_{test} and mitigated domain truncation error . . .	55

LIST OF FIGURES

Figure	Page
1.1 Depiction of trajectory of neutral test particle through partially ionized plasma	2
1.2 Depiction of trajectory of charged test particle through partially ionized plasma	2
3.1 Example rectangular grid	33
3.2 Example semicircular grid	33
4.1 The heating of a tenuous Maxwellian ion distribution scattering off of a higher energy, 2.25 keV, Maxwellian ion distribution with $p = 4$	50
4.2 The cooling of a tenuous Maxwellian ion distribution scattering off of a lower energy, 1.125 keV, Maxwellian ion distribution with $p = 4$	50
4.3 The mean error, $\varepsilon(t)$, associated with using a $2^h \times 2^{h+1}$ grid, and $p = 1$, bilinear trial functions showing h -type refinement, with $h_{\max} = 7$	52
4.4 The mean error, $\varepsilon(t)$, associated with using a 16×32 grid and p -order Lagrange polynomial trial functions showing p -type refinement, with $p_{\max} = 7$	52
4.5 The mean error, $\varepsilon(t = 25\tau)$, associated with using a 5×5 grid, and $p = 4$, bilinear trial functions showing time step refinement, using fully implicit, $\theta = 1$, and $\theta = 0.5$ implicit time advance	52
4.6 The finite element representation of the initial condition $F_i(t = 0\tau)$ is well resolved with polynomial degree $p = 3$, and grid resolution 4×8	54
4.7 Test distribution, F_i , at $t = 50\tau$	54
4.8 The evolution of a tenuous beam of electrons scattering off flowing electron and ion Maxwellian backgrounds with $V_{\parallel} = \frac{1}{2}v_{Te}$	56
4.9 The perpendicular flow, $V_{\text{test}\perp}$, and temperature, T_{test} , of an initially unshifted Maxwellian ion test distribution scattering off a flow-shifted Maxwellian field distribution with a flow of (1) $V_{i\perp} = 0.1 v_{Ti}$, and (2) $V_{i\perp} = v_{Ti}$	59
4.10 Ξ_n , calculated from Eq. (4.11) for the two examples in Fig. 4.9	60
4.11 Modified Bessel functions of the first kind, I_n , in Eq. (4.12)	61

5.1	Conductivity coefficient, α , of an unmagnetized plasma, using a 4×12 rectangular grid, and a few different polynomial degrees, over the domain $\Omega = [0, 4] \times [-6, 6]$	68
5.2	Contour plot of the electron kinetic distortion in the conductivity problem, after $400 \mu s$, with no grid packing	68
5.3	Conductivity coefficient, α , of an unmagnetized plasma, using a 4×12 rectangular grid with packing near the $c_{a\perp} = 0$ and $c_{a\parallel} = 0$ axes, and a few different polynomial degrees, over the domain $\Omega = [0, 4] \times [-6, 6]$	69
5.4	Contour plot of the electron kinetic distortion in the conductivity problem, after $400 \mu s$, with grid packing near the axes	70
5.5	Conductivity coefficient, α , of an unmagnetized plasma, using a 6×12 semicircular grid (using packing within 0.1 radius of origin $(c_{a\perp}, c_{a\parallel}) = (0, 0)$), and a few different polynomial degrees, over a semicircular domain Ω with maximum speed of 6 thermal speeds	72
5.6	Contour plot of the electron kinetic distortion in the conductivity problem, after $400 \mu s$	72
5.7	Contour plot of the electron kinetic distortion in the conductivity problem, after $400 \mu s$, showing grid packing near the origin	73
5.8	Momentum conservation for the conduction problem	73
5.9	Contour plot, for the $\gamma = 0$ plane, of the nonshifted Maxwellian used to compute the TR potentials in Figs. A.1 - A.11	76
5.10	Contour plot of relative error, η , of \bar{h}_e^M , defined in Eq. (5.15)	77
5.11	Contour plot of absolute error, ε , of perpendicular component of $\nabla_{\mathbf{c}_e} \bar{h}_e^M$, defined in Eq. (5.16)	77
5.12	Contour plot of relative error, η , of \bar{g}_e^M , defined in Eq. (5.15)	78
5.13	Contour plot of absolute error, ε , of perpendicular component of $\nabla_{\mathbf{c}_e} \bar{g}_e^M$, defined in Eq. (5.16)	78
5.14	Conductivity factor, α , defined in Eq. (5.3), calculated with different weak forms of the field operator, Eqs. (5.17, 5.21 - 5.25)	84
5.15	Thermalization of electrons and ions with different initial temperatures	86

5.16	Contours of electron kinetic distortion, F_e , at particular time steps of the thermalization of electrons and ions with different initial temperatures in Fig. 5.15	87
A.1	Contour plot of \bar{h}_e^M , defined in Eq. (5.11)	97
A.2	Contour plot of \bar{h}_e^M , calculated by our Fokker-Planck code	97
A.3	Contour plot of parallel component of $\nabla_{\mathbf{e}} \bar{h}_e^M$, defined in Eq. (5.12)	98
A.4	Contour plot of parallel component of $\nabla_{\mathbf{e}} \bar{h}_e^M$, calculated by our Fokker-Planck code	98
A.5	Contour plot of perpendicular component of $\nabla_{\mathbf{e}} \bar{h}_e^M$, defined in Eq. (5.12) .	99
A.6	Contour plot of perpendicular component of $\nabla_{\mathbf{e}} \bar{h}_e^M$, calculated by our Fokker-Planck code	99
A.7	Contour plot of \bar{g}_e^M , defined in Eq. (5.13)	100
A.8	Contour plot of \bar{g}_e^M , calculated by our Fokker-Planck code	100
A.9	Contour plots of parallel component of $\nabla_{\mathbf{e}} \bar{g}_e^M$, defined in Eq. (5.14)	101
A.10	Contour plot of parallel component of $\nabla_{\mathbf{e}} \bar{g}_e^M$, calculated by our Fokker-Planck code	101
A.11	Contour plot of perpendicular component of $\nabla_{\mathbf{e}} \bar{g}_e^M$, defined in Eq. (5.14) .	102
A.12	Contour plot of perpendicular component of $\nabla_{\mathbf{e}} \bar{g}_e^M$, calculated by our Fokker-Planck code	102

INDEX OF SYMBOLS

The following list contains all uncommon mathematical symbols used throughout this work with brief descriptions and the page numbers of their first appearance.

Symbol	Page
\mathbf{a}_a	Particle acceleration under the influence of macroscopic forces 11
\mathbf{B}	Macroscopic external magnetic field 11
$\hat{\mathbf{b}}$	Preferred direction in velocity space, usually aligned with an external field . . 29
\mathbf{c}_a	Total particle velocity, normalized by thermal speed, v_{Ta} 29
C_{ab}	Collision operator between species a and b 11
$c_{a\parallel}$	Component of particle velocity parallel to a preferred direction, $\hat{\mathbf{b}}$, normalized by thermal speed, v_{Ta} 30
$c_{a\perp}$	Component of particle velocity perpendicular to a preferred direction, $\hat{\mathbf{b}}$, normalized by thermal speed, v_{Ta} 30
C_{ab}^F	Field operator 24
$C(f_a, f_b)$	Collision operator between species a and b 11
C_{ab}^M	Collision operator acting on two Maxwellians 24
C_{ab}^T	Test particle operator 21
D_b	Diffusion tensor 15
$\frac{D}{Dt}$	Total time derivative 16
D_b^M	Maxwellian diffusion tensor 21
\mathbf{E}	Macroscopic external electric field 11
E	Electric field strength 47
e	Fundamental charge 49
$E(z_b)$	The error function 21
\mathcal{F}	N -particle distribution function defined in the Liouville equation 11
F_a	Test particle distribution or kinetic distortion, depending on the context 19
f_a	Single particle distribution function 9
f_a^M	A Maxwell-Boltzmann distribution, or simply a Maxwellian 12
G	The Chandrasekhar function 21
g_b	One of the Trubnikov-Rosenbluth potentials. h_b being the other 16
\mathbf{h}_a	Heat flux of species a 10
h_b	One of the Trubnikov-Rosenbluth potentials. g_b being the other 16
\mathbf{I}	Identity tensor 10
I	Number of trial functions throughout Ω in the finite element expansion 31
\mathbf{J}	Current density 17
k_B	Boltzmann's constant. $1.3806488 \times 10^{-23} \text{ JK}^{-1}$ 10
L	Number of quadrilateral cells in the finite element representation 31
m_a	Mass of particles of species a 11
mx	Number of finite element cell divisions in the logical x-direction 32

m_y	Number of finite element cell divisions in the logical y-direction	32
N	There are $N + 1$ independent complex Fourier coefficients, $F_{a,n}(c_{a\parallel}, c_{a\perp}, t)$. .	30
n_a	Density of particles of species a	9
$N_{\mathbf{u}}$	There are $N_{\mathbf{u}} + 1$ independent complex Fourier coefficients, \mathbf{u}_n	45
\mathbb{O}	Symbol for a generic differential operator	26
p	Polynomial degree of each one dimensional Lagrange polynomial	32
P_a	Probability distribution function	13
p_a	Scalar pressure of species a	10
Q_a	Collisional heating of species a	12
q_a	Charge of particles of species a	11
Q_{ab}	Collisional energy exchange between species	18
\mathbb{R}	Symbol for the Residual of a differential equation	35
\mathbf{R}_a	Collisional friction on species a	12
\mathbf{R}_{ab}	Collisional friction between species	18
r_{\max}	Upper limit of the impact parameter	15
r_{\min}	Lower limit of the impact parameter	15
T_a	Temperature (in Joules) of fluid of species a . k_B is suppressed	10
\mathbf{u}	Relative velocity between two particles with velocities \mathbf{v} and \mathbf{v}'	15
\mathbf{U}	Landau tensor	15
u	Magnitude of the vector \mathbf{u}	15
\mathbf{v}	Particle velocity	9
\mathbf{V}_a	Flow velocity of fluid of species a	10
v_{\parallel}	Component of particle velocity parallel to a preferred direction, $\hat{\mathbf{b}}$	29
v_{\perp}	Component of particle velocity perpendicular to a preferred direction, $\hat{\mathbf{b}}$	29
v_{Ta}	Thermal speed of species a	12
\mathbf{w}_a	Random particle velocity for species a	10
\mathbf{x}	Particle position	9
Z	Ion charge in units of the fundamental charge	47
\mathbf{z}_b	Random particle velocity normalized by the thermal speed	21
α_i	Lagrange bipolynomial trial functions of the finite element representation . .	31
δf	An approach to linearizing the Coulomb collision operator	19
Δt	Discrete time step	26
$\delta(\mathbf{v})$	Dirac delta function	46
$\Delta_{\mathbf{v}}$	Velocity space Laplacian	16
ε	Mean pointwise error of F_a	48
ε_0	Permittivity of free space	47
$\varepsilon(\mathbf{v})$	Absolute error	76
Φ	Coefficient of initial test distribution	56
$\phi(\mathbf{v})$	A finite element test function	35
γ	Azimuthal angle in cylindrical velocity coordinates	29
Γ_{ab}	Coefficient of Coulomb operator, related to the collision frequency	15
θ	Centering parameter for time discretization scheme	26
η_L	Electrical resistivity of an unmagnetized Lorentz gas	47

		xv
$\eta(\mathbf{v})$	Relative error	76
$\ln \Lambda_{ab}$	The Coulomb logarithm	15
μ	Magnetic moment	49
∇	Spatial gradient	11
$\nabla_{\mathbf{c}_a}$	Gradient in velocity space normalized by the thermal speed	38
$\nabla_{\mathbf{v}}$	Gradient in velocity space	11
$\boldsymbol{\pi}_a$	Viscosity tensor	10
τ	Ion-ion collision time	49
ξ	Pitch angle	33
Ω	Truncated velocity domain over which F_a is approximated	31
Ω_l	Velocity subdomain over which finite element trial functions are defined	31
$\langle \cdot, \cdot \rangle$	Inner product of two functions in velocity space	35

CHAPTER 1

INTRODUCTION

The Fokker-Planck (FP) operator is a bilinear, integro-differential operator that governs the evolution of a fully ionized plasma caused by Coulomb collisions between charged particles. The FP operator plays an important role in many areas of plasma physics including astrophysical plasmas, laser-produced plasmas, and inertial and magnetic confinement. In these types of plasmas, collisions between charged particles usually involve only two particles (binary collisions), as opposed to tertiary or even higher-order interactions. For weakly coupled plasmas the potential energy of a binary interaction is much less than the average kinetic energy of the particles, hence most collisions result in small angle deflections rather than large changes to a particle's velocity vector (see Figs. 1.1 & 1.2). In addition, the Coulomb interaction between two particles in a plasma is screened by the remaining particles. The effective potential for a single particle within a plasma is a Yukawa potential, with a characteristic length called the Debye length, λ_D . This screened potential is a reduction of the the usual Coulomb potential. At distances longer than the Debye length, the potential exponentially decays meaning that binary collisions effectively occur when the two particles are within a few Debye lengths of each other. The resulting interactions between particles appear as random kicks to their velocity vectors, i.e. Brownian motion. The complicated trajectories taken by the particles are then well described by statistical treatments of the behavior.

A statistical account of Coulomb interactions in fully ionized plasmas leads to the FP operator. This operator is part of the kinetic theory of plasmas that accounts for particle position and velocity. It describes the evolution of what is called the single particle distribution function, which is a 7 dimensional quantity (3 spatial dimensions for particle position, 3 dimensions for particle velocity, and 1 time dimension). Because of the high dimensionality, numerical solutions play an important role in discovering new physics. There are

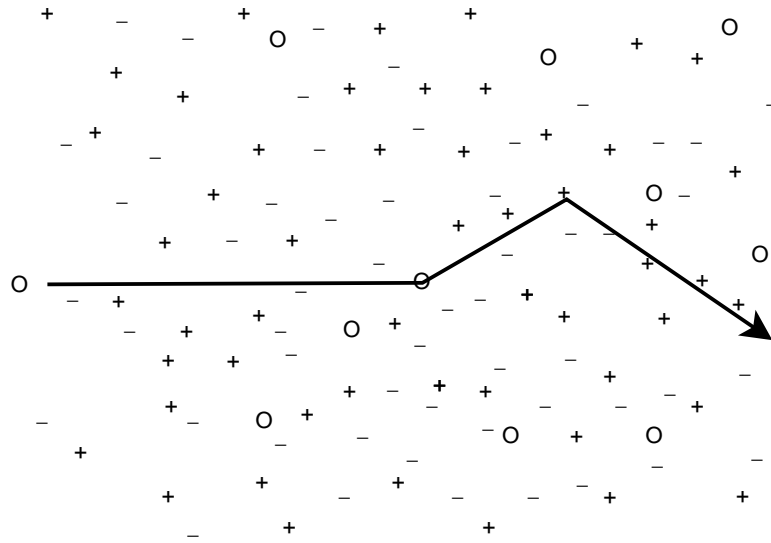


Fig. 1.1: Depiction of trajectory of neutral test particle through partially ionized plasma. Random positions of background electrons are depicted with -, ions with + and neutrals with O. Neutrals take straight line paths between few abrupt atomic collisions.

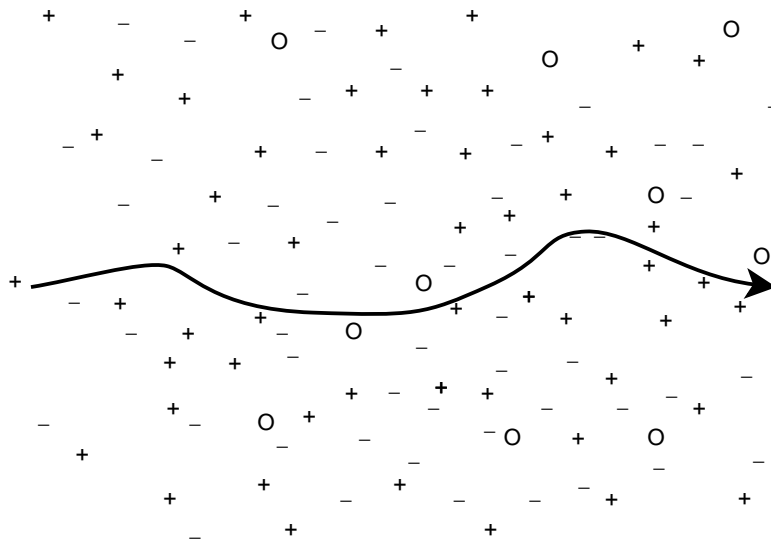


Fig. 1.2: Depiction of trajectory of charged test particle through partially ionized plasma. Random positions of background electrons are depicted with -, ions with + and neutrals with O. Charged particle trajectories are smooth curves dominated by many small-angle collisions with other charged particles.

currently many different methods used to solve the FP equation. A common approach has been to apply finite differencing methods [1, 2, 3]. More recent work has focused on fast multipole methods [4], full Fourier spectral treatments [5], wavelet approximations [6], and spectral collocation methods [7]. The finite volume method, put forth by Xiong et al. [8], will be discussed later for comparison purposes.

Much of the theory in plasma physics seeks to reduce the number of phase space dimensions to avoid the complications involved in the full kinetic description. Yet for a large set of applications, including high-temperature tokamak plasmas and nearly collisionless astrophysical plasmas, it seems the full kinetic description may be just what is needed to provide the accuracy missing from simpler approaches.

Computer codes that solve the FP equation are referred to as Fokker-Planck codes. This work describes the development and application of a Fokker-Planck code which implements the Finite Element Method (FEM) in combination with a Fourier series expansion to represent the velocity dependence of the distribution function. The plasmas under consideration are spatially homogeneous (for simplicity of addressing the velocity dependence). We consider plasmas where collisions between particles are significant and play a comparable role in the dynamics to other physical processes, such as a response to an external field. The formulation we present is for a multispecies plasma with arbitrary masses, but the current algorithm only treats a fully ionized, two species plasma.

The qualities of a successful algorithm are general applicability, numerical efficiency, and preservation of the fundamental conservation properties of the FP operator. An implicit time advance may also be desirable to quickly obtain steady-state solutions. Our algorithm provides a θ -centered implicit time discretization, where for the centering parameter, $0 \leq \theta \leq 1$, the advance can range from fully explicit ($\theta = 0$) to fully implicit ($\theta = 1$). The implicit scheme can be used to take large, stable time steps, Δt , but has first order error in Δt . The Crank-Nicolson method [9] ($\theta = 0.5$) is order $\mathcal{O}(\Delta t^2)$, and can thus be used to

obtain accurate time-dependent solutions.

Although the FEM has been used to treat the spatial dependence of the plasma fluid equations [10], and to solve the neutron transport equation [11], it has not been applied to the numerical solution of the velocity dependent distribution function for plasmas. As shown in refinement tests presented in this work, the convergence properties of the FEM make it desirable for solving the plasma kinetic equation. The algorithm proposed in this paper uses the FEM/Fourier machinery of the NIMROD code [10]. NIMROD is a plasma simulation tool that was written to operate on massively parallel supercomputers and is normally used to solve the plasma fluid equations. NIMROD's data structures, solver capabilities, and parallelism have been adapted to provide a FEM/Fourier analysis on the velocity domain of the FP equation. My work has made use of many preexisting features of the NIMROD code including uniform quadrilateral grids and grid packing, serial and parallel execution, C^0 continuity, and Dirichlet boundary conditions.

In magnetized plasmas distribution functions tend to have a high degree of azimuthal symmetry, with the magnetic field defining the direction of an axis for cylindrical coordinates. Physically this is due to the rapid gyration of particles about magnetic field lines. For this reason, a Fourier series representation is used in the azimuthal direction about this axis, and it is anticipated the angular dependence quickly converges with only a few Fourier terms. The case of large perpendicular flow, however, may require a more extensive Fourier expansion in gyroangle. We consider an example where a flowing background accelerates test particles perpendicular to the axis. Even with perpendicular background flows on the order of the thermal speed, relatively few Fourier terms are required to represent the test distribution.

We begin, in Chapter 2, by discussing the single particle distribution function, its properties and its physical interpretation. The equation that governs the time evolution of the distribution function, called the plasma kinetic equation, is introduced. The term of primary

importance in this work is the Fokker-Planck operator. The general form of this operator is derived from statistical considerations, and then a particular form, called the Coulomb collision operator, is given. The collision operator satisfies physically important conservation laws which are then discussed. Next we derive two linearized forms of the collision operator, which will provide the foundation for the rest of the discussion. The two approaches are referred to as the δf approach, and the Chapman-Enskog-like (CEL) approach. The δf approach uses a linear form of the collision operator called the test particle operator. The CEL approach uses the test particle operator as well as another linear form of the collision operator called the field operator, along with fluid equations for the species densities, temperatures, and flows. Both approaches lead to interesting physical calculations, and both approaches have important uses in modern computational plasma physics.

Chapter 3 gives a detailed description of the numerical scheme used to treat the FP equation. The description begins with the time-discretization scheme and continues with discussion of the Fourier series expansion in the azimuthal direction, and the general theory behind the finite element method. I include a brief accounting of the number of independent unknowns in this representation. This provides a clean way to compare the efficiency of my algorithm with other schemes. Next, the two linearized forms of the collision operator, the test particle operator and the field operator, are treated using the FEM/Fourier scheme.

The next two chapters focus on solving particular problems using my Fokker-Planck code. The code is tested against benchmark calculations, as well as problems designed to utilize the Fourier representation in the azimuthal direction. The results in Chapter 4 are included in a paper submitted to the Journal of Computational Physics, and is currently in the peer review process. A paper with the results in Chapter 5 is in preparation. Chapter 4 looks at problems that involve the test particle operator and utilize the δf approach, while Chapter 5 looks at problems involving both test particle and field operators and utilize the CEL approach. Chapter 4 begins by presenting a calculation of the electrical resistivity of

a plasma. The results are compared to an analytic solution. This problem exhibits a powerful convergence property of the FEM, namely, exponential convergence under refinement of the underlying polynomial degree. The convergence rate of the FEM is one of the primary motivations for conducting research into its use in a Fokker-Planck code. The next benchmark calculation is the thermalization of a tenuous ion plasma with a hotter/cooler background ion plasma. This problem was given in Ref. [8], where the finite volume method, a cousin of the finite element method, is used. Upon comparison, we find our algorithm gives comparable results with far fewer independent unknowns in the underlying representation. In the context of this problem, the property of particle number or density conservation for the collision operator is explored. Fidelity to this property is achieved by our Fokker-Planck code when the velocity domain is large enough. Domain truncation error is shown to decrease as the domain is enlarged, until only the errors inherent in the FEM/Fourier representation are left.

The next problem solved in Chapter 4 is the equilibration of a beam of test particles as it streams through and collides with particles in a background plasma. This problem demonstrates many interesting properties of the collision operator, such as drag that slows the beam down, dispersion or spreading that heats the beam, and diffusion in pitch angle. The beam problem is followed by a problem where test particles initially have zero flow and collisions with particles of a flowing background drag and heat the test particles until equilibrium is reached. This problem is intended to test the Fourier representation by having the background flow perpendicular to the cylindrical axis. The coupling of Fourier modes is explored, and robust convergence is achieved with very few modes.

Chapter 5 examines the results of solving two problems using the CEL approach. First, Chapter 5 reconsiders the conductivity of a plasma. This is similar to the resistivity problem solved in Chapter 4. The difference is that the δf approach does not conserve momentum, while CEL approach conserves particle number, momentum and energy. Results are found

to agree with accepted values of the conductivity, and momentum is conserved up to numerical errors. The source of these errors is explored in detail. Finally, in Chapter 5, a problem is considered where the electrons and ions in a plasma have different initial temperatures. The dynamical problem of energy exchange between the two species until equilibrium is achieved is calculated.

Chapter 6 gives a conclusion to this work, and lists several future efforts, which range from minor improvements of efficiency to major developments, like the addition of spatial dimensions for this Fokker-Planck code. In conclusion, I have had great success in using a finite element/Fourier solution to the Fokker-Planck equation that includes both the test particle and field operators and provides insight into the kinetic properties of fully ionized plasmas.

CHAPTER 2

THE FOKKER-PLANCK EQUATION

The physics of the Fokker-Planck equation

The velocity distribution function

Plasma physics investigates gases, which are hot enough that a significant portion of the particles are ionized. The physics describing the individual motion of charged particles is well known, and in principle could be used to predict the evolution of a plasma. However, calculating the motion of every particle is impractical and undesirable. Impractical because common laboratory plasmas have densities on the order of 10^{20} particles in a cubic meter, thus calculating the trajectory of every particle by taking into account its interaction with every other particle cannot be done even with modern supercomputers. Undesirable because even if a computer could be programmed to give the position and velocity of every single ion and electron, the information content would be overwhelming and further reduction of the results would be required anyway.

Fluid models describe plasmas in terms of spatially smoothed, continuous quantities such as density, flow velocity, and temperature. A simple example of a fluid model is magnetohydrodynamics, or MHD, which treats the plasma as a single, electrically conducting fluid. The two-fluid model is more sophisticated in that it treats the electrons and ions in the plasma as separate fluids.

Historically, gases were thought to be continuous mediums. Today, of course, we know gases are composed of a ridiculously large number of small particles. The development of the kinetic theory of gases, and subsequently statistical mechanics, shortly preceded the discovery of plasmas and the development of the theory describing them. Because of the difficulty in solving the plasma kinetic equation with its seven independent variables (three for particle position, three for particle velocity, and time), plasma fluid models, which

involve only four independent variables (three for position and time) are also useful. However, many fluid models are only applicable within specific regimes of collisionality and magnetic field strengths.

A theory for general collisionality and field strength requires a statistical account of the rapid motion of individual particles, and hence the kinetic theory of ionized gases or plasmas. Today fluid models are understood within the framework of kinetic theory. Plasma kinetic theory is more general, rigorous and informative than plasma fluid models, and more efficient than trying to account for every particle in the system. For these reasons the kinetic theory of gases is a common starting point for modern treatments of the physics of plasmas.

The quantity of primary interest in kinetic theory, and in my research, is the single particle distribution function. The distribution function, $f_a(\mathbf{x}, \mathbf{v}, t)$, is defined so that

$$f_a(\mathbf{x}, \mathbf{v}, t) d\mathbf{x} d\mathbf{v} \quad (2.1)$$

is the probable number of particles, of species a , within an infinitesimal three-dimensional spatial volume, $d\mathbf{x}$, and three-dimensional velocity-space volume, $d\mathbf{v}$, about position \mathbf{x} and velocity \mathbf{v} , at time t . The distribution function is a density of particles in position and velocity space. Therefore, the distribution function may be used to calculate the total density of particles, irrespective of their velocity vectors, using

$$n_a(\mathbf{x}, t) = \int d\mathbf{v} f_a(\mathbf{x}, \mathbf{v}, t). \quad (2.2)$$

In addition to the density, n_a , the distribution function gives information about the location and motion of the particles in the plasma. For instance, at position \mathbf{x} and time t , the density of particles with momentum $m_a \mathbf{v}_0$ is given by $m_a \mathbf{v}_0 f_a(\mathbf{x}, \mathbf{v}_0, t)$, and the density of particles with kinetic energy $\frac{1}{2} m_a v_0^2$ is given by $\frac{1}{2} m_a v_0^2 f_a(\mathbf{x}, \mathbf{v}_0, t)$. Logically, then, the average

momentum density and kinetic energy density of species a are given by

$$n_a^{-1} \int d\mathbf{v} m_a \mathbf{v} f_a(\mathbf{x}, \mathbf{v}, t), \text{ and } n_a^{-1} \int d\mathbf{v} \frac{1}{2} m_a v^2 f_a(\mathbf{x}, \mathbf{v}, t), \quad (2.3)$$

respectively. In fact, the fluid flow, \mathbf{V}_a , the temperature, T_a , and all other fluid quantities of species a are given in terms of velocity moments of the distribution function:

$$\mathbf{V}_a \equiv n_a^{-1} \int d\mathbf{v} \mathbf{v} f_a(\mathbf{x}, \mathbf{v}, t), \quad (2.4)$$

$$T_a \equiv n_a^{-1} \int d\mathbf{v} \frac{1}{3} m_a \mathbf{w}_a^2 f_a(\mathbf{x}, \mathbf{v}, t), \quad (2.5)$$

where $\mathbf{w}_a = \mathbf{v} - \mathbf{V}_a$ is called the random particle velocity. Note that temperatures within this work will be given in units of energy, suppressing Boltzmann's constant, k_B .

Other important moments of the distribution function, which will be used throughout this work, are the scalar pressure, $p_a = n_a T_a$, the heat flux,

$$\mathbf{h}_a = \int d\mathbf{v} \frac{1}{2} m_a w_a^2 \mathbf{w}_a f_a, \quad (2.6)$$

and the viscosity tensor, which is the traceless part of the pressure tensor,

$$\boldsymbol{\pi}_a = m_a \int d\mathbf{v} \left(\mathbf{w}_a \mathbf{w}_a - \frac{w_a^2}{3} \mathbf{l} \right) f_a. \quad (2.7)$$

Here \mathbf{l} is the identity tensor.

The informative capacity of the distribution function comes from the fact that it is defined over the three extra velocity dimensions. This advantage is offset by the computational intensity of solving a partial differential equation in seven dimensions, as opposed to solving small sets of fluid equations (for quantities like n_a , \mathbf{V}_a , T_a) in four dimensions.

The kinetic equation

For any gas, the evolution of f_a is given by the Boltzmann transport equation, also called the kinetic equation,

$$\frac{\partial f_a}{\partial t} + \mathbf{v} \cdot \nabla f_a + \mathbf{a}_a \cdot \nabla_{\mathbf{v}} f_a = \left. \frac{\delta f_a}{\delta t} \right|_{\text{coll}}. \quad (2.8)$$

Here $\nabla = \frac{\partial}{\partial \mathbf{x}}$ and $\nabla_{\mathbf{v}} = \frac{\partial}{\partial \mathbf{v}}$ are gradients in configuration and velocity space, respectively, and \mathbf{a}_a is the acceleration of particles of species a under the influence of macroscopic forces. In the case of fully ionized laboratory plasmas, for a species with charge q_a and mass m_a , forces other than the electromagnetic force, such as gravity can be ignored, and $\mathbf{a}_a = \frac{q_a}{m_a} (\mathbf{E} + \mathbf{v} \times \mathbf{B})$, where \mathbf{E} and \mathbf{B} are the macroscopic electric and magnetic fields acting on the plasma. The quantity, $\left. \frac{\delta f_a}{\delta t} \right|_{\text{coll}}$, on the right side of the kinetic equation is called the collision operator and represents the time rate of change in f_a produced by microscopic forces between individual particles.

The collision operator can be rigorously derived from the Liouville equation for the full N -particle distribution function, \mathcal{F} , defined in phase space, via the BBGKY hierarchy [12]. There is no exact formula for the collision operator, only a sequence of more accurate and less tractable approximations. The key insight Boltzmann had was to assume collisions occur primarily between two particles at a time. This assumption truncates the BBGKY hierarchy, and leads to a bilinear operator, which can be written symbolically as

$$\left. \frac{\delta f_a}{\delta t} \right|_{\text{coll}} = \sum_b C(f_a, f_b). \quad (2.9)$$

The collision operator between species a and b will also appear in the abbreviated form $C_{ab} = C(f_a, f_b)$.

Without loss of generality, it is at this point that fluid models can be tied to kinetic theory. By taking the $\{1, m_a \mathbf{w}_a, \frac{1}{2} m_a w_a^2\}$ velocity moments of Eq. (2.8), the five-moment

fluid equations for a fully ionized, multispecies plasma can be obtained. For reference, they are

$$\frac{\partial n_a}{\partial t} + \nabla \cdot (n_a \mathbf{V}_a) = 0 \quad (2.10)$$

$$m_a n_a \frac{\partial \mathbf{V}_a}{\partial t} + m_a n_a \mathbf{V}_a \cdot \nabla \mathbf{V}_a - n_a q_a (\mathbf{E} + \mathbf{V}_a \times \mathbf{B}) + \nabla p_a + \nabla \cdot \boldsymbol{\pi}_a = \mathbf{R}_a \quad (2.11)$$

$$\frac{3}{2} n_a \frac{\partial T_a}{\partial t} + \frac{3}{2} n_a \mathbf{V}_a \cdot \nabla T_a + n_a T_a \nabla \cdot \mathbf{V}_a + \nabla \cdot \mathbf{h}_a + \nabla \mathbf{V}_a : \boldsymbol{\pi}_a = Q_a \quad (2.12)$$

where the collisional friction,

$$\mathbf{R}_a = \sum_b \int d\mathbf{v} m_a \mathbf{w}_a C_{ab}, \quad (2.13)$$

and collisional heating,

$$Q_a = \sum_b \int d\mathbf{v} \frac{1}{2} m_a w_a^2 C_{ab}. \quad (2.14)$$

One particular distribution function of interest is called the Maxwell-Boltzmann distribution, or Maxwellian:

$$f_a^M(\mathbf{x}, \mathbf{v}, t) = \frac{n_a(\mathbf{x}, t)}{\pi^{3/2} v_{Ta}^3(\mathbf{x}, t)} \exp \left[- \left(\frac{\mathbf{v} - \mathbf{V}_a(\mathbf{x}, t)}{v_{Ta}(\mathbf{x}, t)} \right)^2 \right], \quad (2.15)$$

where the thermal speed,

$$v_{Ta}(\mathbf{x}, t) = \sqrt{\frac{2T_a(\mathbf{x}, t)}{m_a}}. \quad (2.16)$$

It can be shown the Boltzmann collision operator vanishes only when the distribution functions of all species are Maxwellian, with the same temperature and flow velocity. Fluid models are often accurate when the binary collisions are the dominant physical process, keeping the distribution functions very close to a Maxwellian throughout the evolution.

When the magnetic field strength is strong (fusion plasmas), i.e., when the frequency

of the cyclotron motion in the presence of the magnetic field is much greater than the rate at which collisions are occurring, a simplified form of kinetic equation can be derived from averaging over this rapid gyro motion. The resulting lowest-order, kinetic equation describes the evolution of a distribution of guiding centers, which has the advantage of being six dimensional rather than seven.

The algorithm proposed in this work was created with the intention of simulating plasmas where the diffusion, drag, dispersion and other dynamical processes in velocity space related to binary Coulomb collisions are on the same order as other physically interesting processes, such as the plasma's response to an external field. This assumption is physically more realistic for many plasmas as opposed to assuming either the high-collisionality or low-collisionality limit. While many plasmas, even in fusion devices, are very close to Maxwellian, there can be a significant portion of the distribution, which is not, and which cannot be successfully modeled with a gyro-averaged kinetic equation. Where the dynamical evolution of such a plasma is of interest is where the proposed algorithm will be of greatest use.

The Fokker-Planck equation

The motion of a charged particle through a plasma is very complicated, resulting from many collisions with other particles, but the form of the collision operator, $\left. \frac{\delta f_a}{\delta t} \right|_{\text{coll}}$, in Eq. (2.8) must be obtained through statistical analysis. Here it is useful to define a probability distribution function, $P_a(\mathbf{v}, \Delta\mathbf{v})$, where $P_a(\mathbf{v}, \Delta\mathbf{v}) d(\Delta\mathbf{v})$ is the probability, at time t , that a particle of species a , with velocity \mathbf{v} , will undergo several small-angle collision, which will change its velocity by $\Delta\mathbf{v}$ in a short time Δt . We can assume the normalization condition

$$\int P_a(\mathbf{v}, \Delta\mathbf{v}) d(\Delta\mathbf{v}) = 1. \quad (2.17)$$

We also assume this probability does not depend on time explicitly, and it does not depend on the previous random kick, $\Delta \mathbf{v}$, to the particles velocity vector. This is often referred to as a Markov process.

The distribution function, $f_a(\mathbf{x}, \mathbf{v}, t)$, would then evolve as

$$f_a(\mathbf{x}, \mathbf{v}, t) = \int d(\Delta \mathbf{v}) f_a(\mathbf{x}, \mathbf{v} - \Delta \mathbf{v}, t - \Delta t) P_a(\mathbf{v} - \Delta \mathbf{v}, \Delta \mathbf{v}). \quad (2.18)$$

Note, we have also assumed many collisions occur in a time short enough that the particle does not change its spatial location significantly. The time derivative of f_a , due to collisions, would be given by

$$\left. \frac{\delta f_a}{\delta t} \right|_{\text{coll}} = \lim_{\Delta t \rightarrow 0} \frac{f_a(\mathbf{x}, \mathbf{v}, t) - f_a(\mathbf{x}, \mathbf{v}, t - \Delta t)}{\Delta t}. \quad (2.19)$$

By Taylor expanding (2.18), to second order in $\Delta \mathbf{v}$, it can be shown in the limit as $t \rightarrow 0$,

$$\left. \frac{\delta f_a}{\delta t} \right|_{\text{coll}} = -\nabla_{\mathbf{v}} \cdot \left[\left\langle \frac{\Delta \mathbf{v}}{\Delta t} \right\rangle_a f_a \right] + \frac{1}{2} \nabla_{\mathbf{v}} \nabla_{\mathbf{v}} : \left[\left\langle \frac{\Delta \mathbf{v} \Delta \mathbf{v}}{\Delta t} \right\rangle_a f_a \right], \quad (2.20)$$

where

$$\left\langle \frac{\Delta \mathbf{v}}{\Delta t} \right\rangle_a = \frac{1}{\Delta t} \int d(\Delta \mathbf{v}) \Delta \mathbf{v} P_a(\mathbf{v}, \Delta \mathbf{v}), \quad (2.21)$$

and

$$\left\langle \frac{\Delta \mathbf{v} \Delta \mathbf{v}}{\Delta t} \right\rangle_a = \frac{1}{\Delta t} \int d(\Delta \mathbf{v}) \Delta \mathbf{v} \Delta \mathbf{v} P_a(\mathbf{v}, \Delta \mathbf{v}). \quad (2.22)$$

In the context of plasma kinetic theory, Eq. (2.20) is called the Fokker-Planck form of the Coulomb collision operator, $\left\langle \frac{\Delta \mathbf{v}}{\Delta t} \right\rangle_a$ is called the dynamical friction vector and $\left\langle \frac{\Delta \mathbf{v} \Delta \mathbf{v}}{\Delta t} \right\rangle_a$ is called the diffusion tensor. The dynamical friction and the diffusion tensor are referred to as Fokker-Planck coefficients. It is clear, in this form, that these coefficients are average time rates of change in $\Delta \mathbf{v}$ and $\Delta \mathbf{v} \Delta \mathbf{v}$.

Coulomb collision operator

The accuracy of Eq. (2.20) depends on a predominance of collisions that result in small scattering angles. When collisions are simply the result of the Coulomb interaction between two charged particles, the collision operator becomes a bilinear integro-differential operator called the Coulomb collision operator, C_{ab} , which can be written in many equivalent forms. Introducing $\Gamma_{ab} = \frac{q_a^2 q_b^2 \ln \Lambda_{ab}}{4\pi\epsilon_0^2 m_a^2}$ (SI units), where $\ln \Lambda_{ab} = \ln \left(\frac{r_{\max}}{r_{\min}} \right)$ is the Coulomb logarithm and r_{\max} and r_{\min} are upper and lower limits for the impact parameter, one way of writing the Coulomb collision operator is

$$C_{ab} = -\frac{\Gamma_{ab}}{2} \nabla_{\mathbf{v}} \cdot \left[\frac{m_a + m_b}{m_b} (\nabla_{\mathbf{v}} \cdot \mathbf{D}_b) f_a - \nabla_{\mathbf{v}} \cdot (\mathbf{D}_b f_a) \right]. \quad (2.23)$$

Here the diffusion tensor is defined as

$$\mathbf{D}_b(\mathbf{v}, t) = \int d\mathbf{v}' f_b(\mathbf{v}', t) \mathbf{U}, \quad (2.24)$$

with the Landau tensor

$$\mathbf{U} = \frac{u^2 \mathbf{I} - \mathbf{u}\mathbf{u}}{u^3}, \quad (2.25)$$

and $\mathbf{u} = \mathbf{v} - \mathbf{v}'$.

The diffusion tensor and its divergence are related to what are called the Trubnikov-Rosenbluth (TR) potentials [13, 14]:

$$\mathbf{D}_b = \nabla_{\mathbf{v}} \nabla_{\mathbf{v}} g_b, \quad (2.26)$$

$$\nabla_{\mathbf{v}} \cdot \mathbf{D}_b = 2 \nabla_{\mathbf{v}} h_b, \quad (2.27)$$

where g_b and h_b are defined as

$$g_b(\mathbf{v}, t) = \int d\mathbf{v}' f_b(\mathbf{v}', t) u, \quad (2.28)$$

$$h_b(\mathbf{v}, t) = \int d\mathbf{v}' f_b(\mathbf{v}', t) u^{-1}. \quad (2.29)$$

By defining a velocity space Laplacian, $\Delta_{\mathbf{v}} = \nabla_{\mathbf{v}} \cdot \nabla_{\mathbf{v}}$, Eqs. (2.28) and (2.29) can be written in differential form:

$$\Delta_{\mathbf{v}} h_b = -4\pi f_b, \quad (2.30)$$

$$\Delta_{\mathbf{v}} g_b = 2h_b, \quad (2.31)$$

having the same form as Poisson's equation in electrostatics, hence the reason for calling g_b and h_b potentials.

Eqs. (2.23-2.24) can be used to write the collision operator solely in terms of the distribution functions and the scattering tensor, without reference to the diffusion tensor or TR potentials, which is done in the formulation by Landau [15]. Keep in mind all three formulations may be important when considering the best approach for computing the Coulomb operator given any particular application.

By writing the total time derivative found on the left side of Eq. (2.8) as $\frac{D}{Dt} = \frac{\partial}{\partial t} + \mathbf{v} \cdot \nabla + \frac{q_a}{m_a} (\mathbf{E} + \mathbf{v} \times \mathbf{B}) \cdot \nabla_{\mathbf{v}}$, the plasma kinetic equation can be written as:

$$\frac{Df_a}{Dt} = -\nabla_{\mathbf{v}} \cdot \left\{ \sum_b \frac{\Gamma_{ab}}{2} \left[\frac{m_a + m_b}{m_b} (\nabla_{\mathbf{v}} \cdot \mathbf{D}_b) f_a - \nabla_{\mathbf{v}} \cdot (\mathbf{D}_b f_a) \right] \right\}. \quad (2.32)$$

This form of the Coulomb operator demonstrates the evolution of the distribution function along characteristics arises from a divergent current of particles due to collisions - a law of continuity in velocity space. In this form, Eq. (2.32) can also be recognized as the Fokker-

Planck equation in velocity space - the first term on the right hand side of Eq. (2.23), $2\frac{m_a+m_b}{m_b}\nabla_{\mathbf{v}} \cdot \mathbf{D}_b$, is the dynamical friction and governs drag in velocity space [16], and the second term, \mathbf{D}_b , is the diffusion tensor and describes dispersion in velocity space.

By defining charge density as $\rho_c = \sum_a q_a n_a$ (often set to zero under the quasi-neutrality assumption) and current density as $\mathbf{J} = \sum_a q_a n_a \mathbf{V}_a$, the plasma kinetic equation with Maxwell's equations provide a closed system of coupled equations. This system of equations is relevant in many arenas of plasma physics, including space and astrophysical plasmas, laser-produced plasmas, and magnetic confinement plasmas. Because few analytic solutions exist, numerical solutions have an important role in discovering new physics. One important reason for constructing numerical solution is to offset the expense of building experiments, which test new concepts, particularly in the effort to build nuclear fusion devices.

However, solving the Maxwell and plasma kinetic system is a very challenging task. Many schemes have been constructed to simplify this task. One of the main challenges is the distribution function generally depends on seven independent variables, with three spatial coordinates, three velocity coordinates and one time dimension. Modern super computers, with parallel processing, may have a real chance of solving such a complex system. Much of the theory in plasma physics seeks to reduce the number of phase space dimensions to avoid the complications involved with approaching the full kinetic description. Nevertheless it seems the full kinetic description may be needed to provide the accuracy missing from simpler approaches.

My research has involved developing and implementing an algorithm to solve a linearized form of Eq. (2.32) acting on a spatially homogeneous distribution function. Algorithms, which focus on solving the evolution of the velocity distribution function due to the Coulomb collision operator of Eq. (2.32), such as the algorithm proposed in this work, are called Fokker-Planck codes. The Fokker-Planck code that was developed over the course

of this research project provides an important step toward a code that can solve the full kinetic equation in a reasonable amount of time.

Conservation laws

Before moving on, it is important to recognize certain fundamental properties of the Coulomb collision operator, which will be of particular interest in what follows. It can be shown for arbitrary distributions f_a and f_b ,

$$\int d\mathbf{v} C(f_a, f_b) = 0, \quad (2.33)$$

$$\int d\mathbf{v} \mathbf{v} [m_a C(f_a, f_b) + m_b C(f_b, f_a)] = 0, \quad (2.34)$$

$$\int d\mathbf{v} \frac{1}{2} v^2 [m_a C(f_a, f_b) + m_b C(f_b, f_a)] = 0. \quad (2.35)$$

These three equations have important physical interpretations. Equation (2.33) states Coulomb collisions cannot create or destroy particles. Equation (2.34) states the total momentum is conserved. Equation (2.35) states the total energy is conserved. Preserving these three laws are of fundamental importance when constructing any numerical solution to Eq. (2.32).

By defining the collisional friction and collisional energy exchange between species as

$$\mathbf{R}_{ab} = \int d\mathbf{v} m_a \mathbf{v} C_{ab} \quad (2.36)$$

and

$$Q_{ab} = \int d\mathbf{v} \frac{1}{2} m_a v^2 C_{ab}, \quad (2.37)$$

Eqs. (2.34 & 2.35) can be written in an especially compact form:

$$\mathbf{R}_{ab} = -\mathbf{R}_{ba}, \quad (2.38)$$

$$Q_{ab} = -Q_{ba} - \mathbf{R}_{ba} \cdot (\mathbf{V}_b - \mathbf{V}_a). \quad (2.39)$$

Linearizing the Fokker-Planck equation

Since the Coulomb collision operator is nonlinear in the distribution functions, cf. Eq. (2.23), it is desirable when constructing a Fokker-Planck code to first linearize the collision operator in some way. Many plasmas of interest, both astrophysical and in the laboratory, come very close to being described as Maxwellian, and it is appropriate to linearize the collision operator by considering small perturbations away from a Maxwellian. However, there is not a unique way of doing this. In order to build up from simple to more complicated formulations, I chose to use two different approaches to linearize, which I refer to as δf -linearization and Chapman-Enskog-like (CEL) linearization.

The δf approach assumes the distribution functions can be decomposed into static Maxwellian backgrounds (all in thermal equilibrium with one another) and a small deviations away from this:

$$f_a(\mathbf{v}, t) = f_a^{\text{M}}(\mathbf{v}) + F_a(\mathbf{v}, t), \quad (2.40)$$

where $F_a/f_a^{\text{M}} \ll 1$. Importantly, the Maxwellian composes the bulk of the distribution function, and is static. The background Maxwellians, f_a^{M} , are called field particles, while the small deviations, F_a , are called test particles. By small deviation, it is meant the test particles are so tenuous that binary collisions between them may be ignored and evolution of the field distributions is negligible. This assumption, of course, bears consideration when obtaining results.

The CEL approach defines an evolving Maxwellian, (which may also be termed field particles,)

$$f_a^{\text{M}} = n_a \left(\frac{m_a}{2\pi T_a} \right)^{3/2} \exp \left[-\frac{m_a (\mathbf{v} - \mathbf{V}_a)^2}{2T_a} \right], \quad (2.41)$$

which is built from the time-dependent Maxwellian moments of the full distribution func-

tion,

$$n_a = \int d\mathbf{v} f_a, \quad (2.42)$$

$$\mathbf{V}_a = n_a^{-1} \int d\mathbf{v} \mathbf{v} f_a, \quad (2.43)$$

$$T_a = n_a^{-1} \int d\mathbf{v} \frac{1}{3} m_a \mathbf{v}^2 f_a, \quad (2.44)$$

for all times throughout the evolution of the plasma. The difference between the full distribution function and this Maxwellian is conventionally called the kinetic distortion,

$$F_a(\mathbf{v}, t) = f_a(\mathbf{v}, t) - f_a^{\text{M}}(\mathbf{v}, t). \quad (2.45)$$

Note, the kinetic distortion is not assumed to be small at this point, nor are the Maxwellians of different species assumed to ever be in equilibrium. This construction is fully general in that no ordering is necessary between the evolution equations for f_a^{M} and F_a , in [17].

The important differences between this assumption and the assumption of the δf -linearization scheme are: (1) the Maxwellian background is allowed to evolve in time, and (2) this decomposition is exclusive meaning the Maxwellian moments of the kinetic distortion vanish. These two different linearization schemes lead to very different collision operators, as will be shown in the discussion that follows. A wide variety of alternative linearization schemes exist, including the diffusion approximation [18]. However, the benefits of choosing these two particular schemes will become clear as we discuss the resulting collision operators in the following subsections.

δf -linearization

Under the δf -linearization scheme, cf. Eq. (2.40), the kinetic equation becomes

$$\frac{DF_a}{Dt} = \sum_b C(F_a, f_b^M) = - \sum_b \frac{\Gamma_{ab}}{2} \nabla_{\mathbf{v}} \cdot \left(\frac{m_a}{m_b} F_a \nabla_{\mathbf{v}} \cdot \mathbf{D}_b^M - \mathbf{D}_b^M \cdot \nabla_{\mathbf{v}} F_a \right), \quad (2.46)$$

where $\mathbf{D}_b^M(\mathbf{v}) \equiv \int d\mathbf{v}' f_b^M(\mathbf{v}') \mathbf{U}$ is the Maxwellian diffusion tensor. The term on the right side of the equation is called the test particle operator, abbreviated in this text as $C_{ab}^T = C(F_a, f_b^M)$. Note the collision operator $C(f_a^M, f_b^M)$ does not appear in Eq. (2.46) because all field distributions have the same flow velocity and temperature, by assumption, and the collision operator $C(F_a, F_b)$ is neglected since it involves the two small distributions, F_a and F_b .

Using

$$\nabla_{\mathbf{v}} \cdot \mathbf{D}_b^M = - \frac{2}{v_{Tb}} \mathbf{z}_b \cdot \mathbf{D}_b^M, \quad (2.47)$$

where $\mathbf{z}_b = \mathbf{w}_b/v_{Tb}$ is the random particle velocity normalized by the thermal speed, Eq. (2.46) simplifies to

$$\frac{DF_a}{Dt} = \sum_b \frac{\Gamma_{ab}}{2} \nabla_{\mathbf{v}} \cdot \left[\left(\frac{2}{v_{Tb}} \frac{m_a}{m_b} \mathbf{z}_b F_a + \nabla_{\mathbf{v}} F_a \right) \cdot \mathbf{D}_b^M \right]. \quad (2.48)$$

Substituting f_b^M into Eq. (2.24) yields an analytic form for the diffusion tensor

$$\mathbf{D}_b^M = \frac{n_b}{v_{Tb}} \left[\frac{3G(z_b) - E(z_b)}{z_b^3} \mathbf{z}_b \mathbf{z}_b + \frac{E(z_b) - G(z_b)}{z_b} \mathbf{I} \right], \quad (2.49)$$

where $G(z_b) = \frac{E(z_b)}{2z_b^2} - \frac{e^{-z_b^2}}{\sqrt{\pi}z_b}$ is the Chandrasekhar function [16] and $E(z_b) = \frac{2}{\sqrt{\pi}} \int_0^{z_b} dx e^{-x^2}$ is the error function. Note, by keeping a finite background flow, \mathbf{V}_b , in \mathbf{z}_b , we can examine test particle distributions scattering off background distributions flowing in the lab frame.

The simplicity of the test particle operator comes from analytically computing integrals of Maxwellian distribution functions. This turns the kinetic equation for F_a into a partial differential equation, which is much easier to deal with than the full integro-differential operator of the full collision operator. For this reason the test particle operator was chosen to be coded first. However, there are errors incurred in using this operator, which will be discussed in the subsection, Conservation laws revisited.

The CEL equation

In this subsection, evolution equations for f_a^M and F_a , (Eq. (2.45)), are constructed, and a hybrid set of kinetic and fluid equations is obtained. Note the fluid equations, Eqs. (2.10 - 2.12), were derived for a general distribution function. Since the Maxwellian, f_a^M , (Eq. (2.41)) , is built from the Maxwellian moments of f_a , it follows the fluid equations completely describe the evolution of f_a^M . For a spatially homogeneous plasma, the five-moment fluid equations can be written as

$$\frac{\partial n_a}{\partial t} = 0, \quad (2.50)$$

$$\frac{\partial \mathbf{V}_a}{\partial t} = \frac{q_a}{m_a} (\mathbf{E} + \mathbf{V}_a \times \mathbf{B}) + \frac{1}{m_a n_a} \sum_b \mathbf{R}_{ab}, \quad (2.51)$$

$$\frac{\partial T_a}{\partial t} = \frac{2}{3n_a} \sum_b Q_{ab}. \quad (2.52)$$

The collisional friction, \mathbf{R}_{ab} , and collisional energy exchange, Q_{ab} , given in Eqs. (2.36 & 2.37) are defined in terms of the full distribution function, and provide closure for the fluid theory.

The time derivative of f_a^M can be written as

$$\frac{Df_a^M}{Dt} = \frac{Dn_a}{Dt} \frac{\partial f_a^M}{\partial n_a} + \frac{D\mathbf{V}_a}{Dt} \cdot \frac{\partial f_a^M}{\partial \mathbf{V}_a} + \frac{Dv_{Ta}}{Dt} \frac{\partial f_a^M}{\partial v_{Ta}} + \frac{D\mathbf{v}}{Dt} \cdot \frac{\partial f_a^M}{\partial \mathbf{v}}. \quad (2.53)$$

This expression is simplified using Eqs. (2.50-2.52):

$$\frac{Df_a^M}{Dt} = \frac{2f_a^M}{m_a n_a v_{Ta}} \sum_b \left[\mathbf{z}_a \cdot \mathbf{R}_{ab} + v_{Ta}^{-1} \left(\frac{2}{3} z_a^2 - 1 \right) Q_{ab} \right]. \quad (2.54)$$

Substituting this expression into Eq. (2.32) yields

$$\frac{DF_a}{Dt} = \sum_b \left\{ C_{ab} - \frac{2f_a^M}{m_a n_a v_{Ta}} \left[\mathbf{z}_a \cdot \mathbf{R}_{ab} + v_{Ta}^{-1} \left(\frac{2}{3} z_a^2 - 1 \right) Q_{ab} \right] \right\}. \quad (2.55)$$

This equation is the Chapman-Enskog-like (CEL) kinetic equation, introduced in [17]. Here, however, all spatial dependency have been removed. The CEL equation governs the evolution of the kinetic distortion, while Eqs. (2.50-2.52) govern the evolution of the Maxwellian part of the distribution function. If the macroscopic electric and magnetic fields are given as sources, then this set of equations constitute a closed system of coupled equations. The fluid equations are closed by solving for the kinetic distortion, and the kinetic distortion evolves according to the kinetic equation, Eq. (2.55). The method, which will be used to approximate the kinetic distortion, is the 1D Fourier + 2D Finite element representation described later.

The linearized CEL equation

At this point Eq. (2.55) is fully general, with no assumptions about ordering the kinetic distortion relative to the Maxwellian. While it is possible to construct a fully nonlinear solution to the CEL kinetic equation, this work is focused on solving linearized forms of the collision operator. The plasmas considered in this work are assumed to have such tenuous kinetic distortions that binary collisions between them may be ignored. This assumption yields a collision operator linear in the kinetic distortion:

$$C_{ab} \approx C_{ab}^M + C_{ab}^T + C_{ab}^F, \quad (2.56)$$

where $C_{ab}^M = C(f_a^M, f_b^M)$, $C_{ab}^T = C(F_a, f_b^M)$, and the field operator, $C_{ab}^F = C(F_a, f_b^M)$. As in the subsection, δf -linearization, we refer to C_{ab}^T as the test particle operator, which was given previously. While it is possible to write C_{ab}^M in a similar way, and perform further simplifications, it is more practical to add the Maxwellian distribution to the kinetic distortion and use the test particle operator to compute $C(f_a, f_b^M) = C_{ab}^M + C_{ab}^T$.

The field operator does not simplify like the test particle operator because the diffusion tensor of a generic kinetic distortion does not take a specific analytic form. Therefore, the diffusion tensor or TR potentials must be computed numerically. Since these integrals must be computed over the entire velocity domain, the field operator is much more computationally expensive than the test particle operator.

Conservation laws revisited

Recall Eqs. (2.38 & 2.39) are a statement that Coulomb collisions must conserve momentum and energy, respectively. Incidentally, these properties imply that $\mathbf{R}_{aa} = 0$ and $Q_{aa} = 0$, and hence, are skipped in the calculation. In order to simplify the following discussion, I must define a few more symbols. The collisional friction or collisional energy exchange with a superscript M, T, or F are computed using the collision operator with the corresponding superscript. For example, \mathbf{R}_{ab}^T will be understood to be the collisional friction the field particles exert on the test particles (i.e., the test particle operator, C_{ab}^T , is used).

A principle reason for developing the CEL equation, Eq. (2.55), is that a kinetic equation using the test particle operator alone is not capable of conserving momentum and energy, since $\mathbf{R}_{ab}^T = -\mathbf{R}_{ba}^F$, and $Q_{ab}^T = -Q_{ba}^F - \mathbf{R}_{ba}^F \cdot (\mathbf{V}_b - \mathbf{V}_a)$. In the δf -linearization scheme, the test particle friction and energy exchange are finite, but the field terms are necessarily zero, and are never used to evolve the static Maxwellian backgrounds. The CEL approach has exactly the necessary terms present to preserve these conservation laws.

However, the differences in how the test particle operator and field operator are calculated (e.g., the test particle operator is a differential operator, whereas the field operator is an integro-differential operator) can lead to numerical errors that spoil these conservation properties in poorly resolved simulations. Thus, although the CEL approach analytically guarantees conservation of momentum and energy, numerical errors can spoil exact conservation. These matters will be discussed in detail in Chapter 5.

CHAPTER 3

NUMERICAL SCHEME

In this chapter, we discuss the general approach for approximating solutions to initial value problems involving Eq. (2.32). The temporal discretization and treatment of the time derivative are first discussed. Next the discretization of the velocity domain using the finite element method in combination with a Fourier series expansion is explained. A common argument justifying the use of the finite element method, based on a variational principle, is summarized. This leads to the construction of an algebraic system of equations approximating Eq. (2.32). C^0 continuity of the solution requires converting this system of algebraic equations to the so-called weak form. Exact details of how this is done for the two linearized forms of the collision operator are discussed at the end of this chapter.

Time-discretization

We approximate the time derivative in Eq. (2.32) using first order finite differencing. More precisely, a semi-implicit time-discretization scheme [9] with centering parameter $0 \leq \theta \leq 1$ is used to advance Eq. (2.32) over time step $\Delta t = t^{k+1} - t^k$. This is explained in the following way. Consider a differential equation of the form

$$\frac{\partial f}{\partial t} = \mathbb{O}(f), \tag{3.1}$$

where \mathbb{O} is some linear velocity-space (integro-)differential operator. Recall that we are considering spatially homogeneous plasmas such that the total time derivative, $\frac{D}{Dt}$, may be replaced by the partial derivative, $\frac{\partial}{\partial t}$, in the left side of Eqs. (2.46 & 2.55). For problems with external fields, the acceleration term within $\frac{D}{Dt}$ will appear explicitly as a source term on the right side and will not affect the time-discretization scheme. Therefore, the Fokker-Planck equations resulting from either the δf approach, or the CEL approach take the form of Eq. (3.1).

A θ -centered, time-discretized form of Eq. (3.1) is written as

$$\Delta f - \theta \Delta t \mathbb{O}(\Delta f) = \Delta t \mathbb{O}(f^k), \quad (3.2)$$

where $f^k = f(t^k)$, and $\Delta f \equiv f^{k+1} - f^k$. To solve for the evolution of f , one solves this equation for Δf and adds this to the solution at the previous time step. When $\theta = 0$, the time advance is fully explicit, meaning Δf is solved for explicitly in terms of the solution at the previous time step. When $\theta = 1$, the time advance is fully implicit, meaning that f^{k+1} , which appears in $\mathbb{O}(\Delta f)$ on the left side of Eq. (3.2), is solved for implicitly.

The fully explicit solution has the disadvantage of being numerically unstable under certain conditions, forcing the time steps to be small. A fully implicit equation is unconditionally stable, and can be used to jump quickly to an equilibrium solution. In taking large time steps, however, the time evolution will not be accurately resolved, and the solution accumulates errors on the order of Δt . Once equilibrium is reached, however, these errors are due strictly to the velocity space representation. When $\theta = \frac{1}{2}$, the solution is also unconditionally stable, and the error is second order in Δt , giving more accurate time evolution for small time steps than the fully implicit method. This amounts to a trapezoidal rule for the time-discretization. Error accumulation due to time-discretization will be demonstrated in some of the example problems discussed later. Since any one of these centering parameters may be useful, depending on the situation, it is important to construct a solution which keeps the centering parameter generic.

Applying this scheme to the test particle operator of the δf approach yields

$$\Delta F_a - \theta \Delta t \sum_b C(\Delta F_a, f_b^M) = \Delta t \sum_b C(F_a^k, f_b^M), \quad (3.3)$$

where the Maxwellians are simply the initial Maxwellians, $f_b^M(t = 0)$.

For the CEL equation two subtleties exist regarding this time-discretization scheme.

First, the field operator in Eq. (2.56) is a summation of collision operators acting on kinetic distortions of different species, F_b . If these terms are to be treated implicitly, then all kinetic distortions must be advanced simultaneously. Alternatively, a staggered approach that solves for a single F_a at a time may be taken. This approach treats the field operator terms for unlike species explicitly. Our algorithm has been designed to handle either case. Second, the right hand side of Eq. (2.55) is dependent upon the Maxwellian moments, n_a , \mathbf{V}_a , and T_a . An implicit treatment of these quantities would require both F_a and the Maxwellian moments to be advanced simultaneously. For simplicity, F_a and f_a^M will be advanced in a time staggered fashion, allowing Eq. (2.55) to be advanced independent of Eqs. (2.50-2.52). However, this means that the collision term, C_{ab}^M , as well as

$$\mathbf{R}_{ab}^M = \int d\mathbf{v} m_a \mathbf{v} C_{ab}^M, \quad \text{and} \quad Q_{ab}^M = T_a \int d\mathbf{v} z_a^2 C_{ab}^M \quad (3.4)$$

must be treated explicitly.

With these considerations, the time discretized form of Eq. 2.55 is written as:

$$\begin{aligned} \Delta F_a - \theta \Delta t \sum_b \left\{ \Delta C_{ab} - \frac{2f_a^M}{m_a n_a v_{Ta}} \left[\mathbf{z}_a \cdot \Delta \mathbf{R}_{ab} + v_{Ta}^{-1} \left(\frac{2}{3} z_a^2 - 1 \right) \Delta Q_{ab} \right] \right\} \\ = \Delta t \sum_b \left\{ C_{ab} - \frac{2f_a^M}{m_a n_a v_{Ta}} \left[\mathbf{z}_a \cdot \mathbf{R}_{ab} + v_{Ta}^{-1} \left(\frac{2}{3} z_a^2 - 1 \right) Q_{ab} \right] \right\}, \end{aligned} \quad (3.5)$$

where all quantities on the right side are calculated using $F_a(\mathbf{v}, t^k)$ and $f_b^M(\mathbf{v}, t^{k+1/2})$, and all quantities on the left side are calculated using ΔF_a and $f_b^M(\mathbf{v}, t^{k+1/2})$. Table (3.1) diagrams the process by which the fluid and kinetic quantities are updated in a staggered fashion. As stated previously, C_{ab}^M , \mathbf{R}_{ab}^M , and Q_{ab}^M are included on the right side of Eq. (3.5), but not the left side. By setting $\theta = 1$, Eq. (3.5) becomes fully implicit in all terms except those involving C_{ab}^M , \mathbf{R}_{ab}^M and Q_{ab}^M . By setting $\theta = 0$, Eq. (3.5) becomes fully explicit. Our algorithm's task is to solve Eq. (3.5) for ΔF_a , and add it to the solution at the previous time

Table 3.1: Diagram of staggered update of the CEL approach. Shown are the updated quantities, the order in which they are calculated, and the equations used in their update.

Time step	k	$k + \frac{1}{2}$	$k + 1$
Equation used	Eq. (3.5)	Eqs. (2.50 - 2.52)	Eq. (3.5)
Quantity updated	F_a	$\longrightarrow f_a^M(n_a, \mathbf{V}_a, T_a)$	$\longrightarrow F_a$

step, $F_a(\mathbf{v}, t^k)$. The fact that collisions between Maxwellians, C_{ab}^M , are treated explicitly may limit the size of Δt for a numerically stable time advance, however, the extent to which this is true is presently unclear.

Equations (3.3 & 3.5) are the paramount equations of this work, and the primary function of my Fokker-Planck code is to solve these two equations. The remaining text of this work focuses on my numerical treatment, and its application to various problems of interest.

A 2D finite element/1D Fourier representation

This section describes in detail the expansion used to construct a numerical approximation to F_a . First, the cylindrical velocity space coordinate system is explained and a Fourier series is defined to handle the azimuthal direction. The remaining two velocity dimensions use a finite element representation.

Azimuthal Fourier expansion

Cylindrical coordinates $(v_{\parallel}, v_{\perp}, \gamma)$ are chosen such that v_{\parallel} is the component of a particle's velocity parallel to a preferred direction $\hat{\mathbf{b}}$, v_{\perp} is the component of a particle's velocity directed radially perpendicular to $\hat{\mathbf{b}}$ and γ is the azimuthal angle defined relative to another vector field perpendicular to $\hat{\mathbf{b}}$. Additionally, each distribution function is defined over coordinates normalized by that species thermal speed, $\mathbf{c}_a = \mathbf{v}/v_{Ta}$. This coordinate system permits a Fourier series representation of the distribution function in the azimuthal direc-

tion:

$$F_a(\mathbf{c}_a, t) = \sum_{n=-N}^N F_{a,n}(c_{a\parallel}, c_{a\perp}, t) e^{in\gamma}, \quad (3.6)$$

where $F_{a,-n}(c_{a\parallel}, c_{a\perp}, t) = F_{a,n}^*(c_{a\parallel}, c_{a\perp}, t)$ for the real quantity F_a .

If $\hat{\mathbf{b}}$ is parallel to a magnetic field, v_{\parallel} is the velocity along the field and γ is gyroangle. For plasmas in the presence of a strong magnetic field, rapid convergence in the periodic γ -direction is expected, hence the distribution function would be well approximated with only a few Fourier terms. Indeed, most Fokker-Planck codes use the gyroaveraged form of the Fokker-Planck operator [8], basically solving for $F_{a,0}(c_{a\parallel}, c_{a\perp}, t)$ only. However, distributions with a finite flow perpendicular to the $\hat{\mathbf{b}}$ axis must have at least the $n = 1$ Fourier modes, and mode coupling in the Fokker-Planck equation necessitates the use of higher order harmonics. Such a problem is considered in Chapter 4 where robust convergence in the Fourier representation is achieved even in extreme cases of perpendicular flows on the order of thermal speeds.

Note, since the velocity space is scaled by thermal speeds, which are changing in the CEL approach, the time derivative in the kinetic distortion is calculated as

$$\frac{\partial F_a}{\partial t} = \frac{\partial F_a}{\partial t} \Big|_{v_{Ta}} + \frac{\partial v_{Ta}}{\partial t} \frac{\partial F_a}{\partial v_{Ta}}, \quad (3.7)$$

where the first term is the total time derivative holding the thermal speed constant, and the second term corrects for an evolving grid. Using the temperature fluid equation, and simplifying, this second term becomes

$$\frac{\partial v_{Ta}}{\partial t} \frac{\partial F_a}{\partial v_{Ta}} = \frac{2}{3m_a n_a v_{Ta}^2} Q_a \mathbf{c}_a \cdot \nabla_{\mathbf{c}_a} F_a. \quad (3.8)$$

This term is taken to the right side of the CEL kinetic equation, and treated in a similar way to the terms involving the collisional friction and energy exchange.

Finite element representation

For $|\mathbf{c}_a| = \frac{|\mathbf{v}|}{v_{Ta}} \gg 1$, we assume the velocity space distribution function approaches zero, causing every term in the kinetic equation to vanish. This implies the velocity domain can be truncated at sufficiently high velocities. The errors introduced by using a finite domain for velocity space are referred to as domain truncation errors. By breaking this truncated velocity domain, Ω , into L contiguous subdomains, Ω_l , such that $\bigcup_{l=1}^L \Omega_l = \Omega$, the Fourier coefficients in Eq. (3.6) may be approximated by a finite element basis representation

$$F_{a,n}(c_{a\parallel}, c_{a\perp}, t) = \sum_{i=1}^I F_{a,n,i}(t) \alpha_i(c_{a\parallel}, c_{a\perp}), \quad (3.9)$$

where the α_i are I piecewise bipolynomial trial functions defined over only one Ω_l , vanishing elsewhere. A Lagrange quadrilateral expansion is used, meaning the α_i are Lagrange bipolynomials with equispaced nodes defined over the unit square and mapped bilinearly to quadrilaterals, Ω_l . Since only one polynomial takes on a value of unity on a particular node, and the rest vanish, the coefficients, $F_{a,n,i}$, represent the value of $F_{a,n}$ at the nodes. Additionally, C^0 continuity is enforced across Ω , meaning that nodes along cell boundaries, $\partial\Omega_l$, overlap, and the coefficients, which represent values there must be equivalent. However, the first derivatives at these nodes are independent, and hence efforts must be taken in the formulation to avoid second order derivatives of the kinetic distortion. Finally, since cylindrical coordinates are being used, regularity along the axis ($|\mathbf{c}_a| = 0$) is enforced by setting all coefficients $F_{a,n,i}$ with $n > 0$ to zero.

Combining Eqs. (3.9 & 3.6) yields the full representation of F_a :

$$F_a(\mathbf{c}_a, t^k) = \sum_{n=-N}^N \sum_{i=1}^I F_{a,n,i}^k \alpha_i(c_{a\parallel}, c_{a\perp}) e^{in\gamma}. \quad (3.10)$$

In the language of the finite element method, the functions used in this series expansion, $\alpha_i e^{in\gamma}$, are called trial functions.

Degrees of freedom

It is important, when comparing this representation to other numerical solutions (such as finite difference or finite volume schemes), to count the number of independent coefficients, $F_{a,n,i}$, in this representation. This is referred to as the degrees of freedom of the representation. While it may seem like there are $I \times (2N + 1)$ degrees of freedom, this is a slight over count. It was previously mentioned that C^0 continuity will be enforced over the domain Ω . This, as well as the regularity condition along the cylindrical axis, reduces the degrees of freedom.

The Lagrange bipolynomials, α_i , are constructed by taking all possible products of one dimensional Lagrange polynomials of a particular order, p . Therefore, the number of nodes within a single cell, Ω_l , is $(p + 1)^2$. The domain is broken into m_x cells in the perpendicular direction, and m_y cells in the parallel direction, yielding a total of $m_x \times m_y$ cells. Therefore, $I = (p + 1)^2 \times m_x \times m_y$. Redundancy along cell boundaries gives $p^2 \times m_x \times m_y + p(m_x + m_y) + 1$ degrees of freedom.

Before the regularity condition is taken into account, we must discuss the parametric mapping from logical space to velocity space. It is wise not to use the real coordinates in the labeling of the Lagrange bipolynomials, α_i . In fact, we expand the coordinates themselves in the 2D finite element basis:

$$c_{a\parallel} = \sum_{i=1}^I c_{a\parallel,i} \alpha_i(x, y), \quad (3.11)$$

$$c_{a\perp} = \sum_{i=1}^I c_{a\perp,i} \alpha_i(x, y). \quad (3.12)$$

One advantage of using a mapping from logical space (a unit square for each cell) to real space is the reuse of data structures storing the bipolynomials, as well as the abscissa, weights and Jacobians used in performing numerical quadrature. Having this extra layer of abstraction means the real space coordinates are not tied to the geometry of the grid used

to partition the domain. This permits constructing two different types of grids (rectangular and semicircular) for different applications. Examples of these two grids are given in Figs. (3.1 & 3.2). The beauty of this mapping is the Fokker-Planck code, written in cylindrical coordinates, does not need to be rewritten to use the semicircular grid.

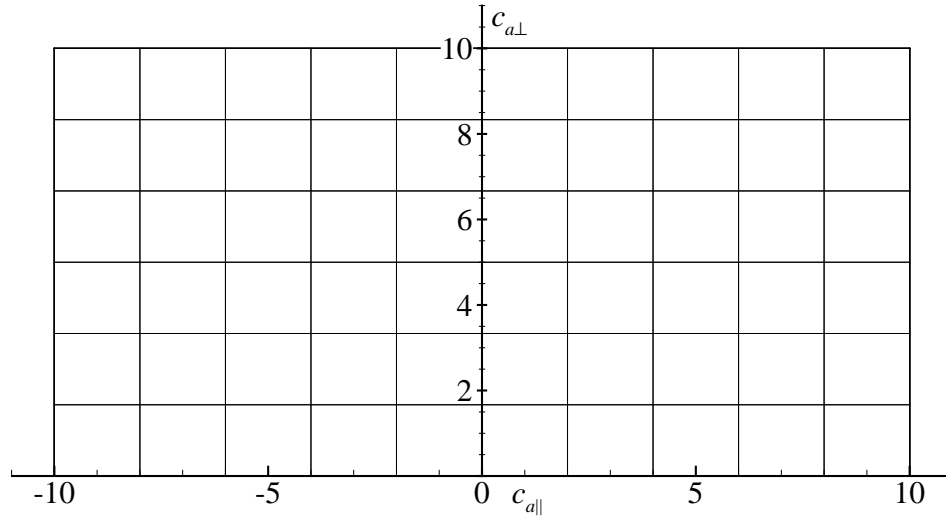


Fig. 3.1: Example rectangular grid. Here $m_x = 6$ and $m_y = 10$. The logical x-direction corresponds to $c_{a\perp}$ and the logical y-direction corresponds to $c_{a\parallel}$.

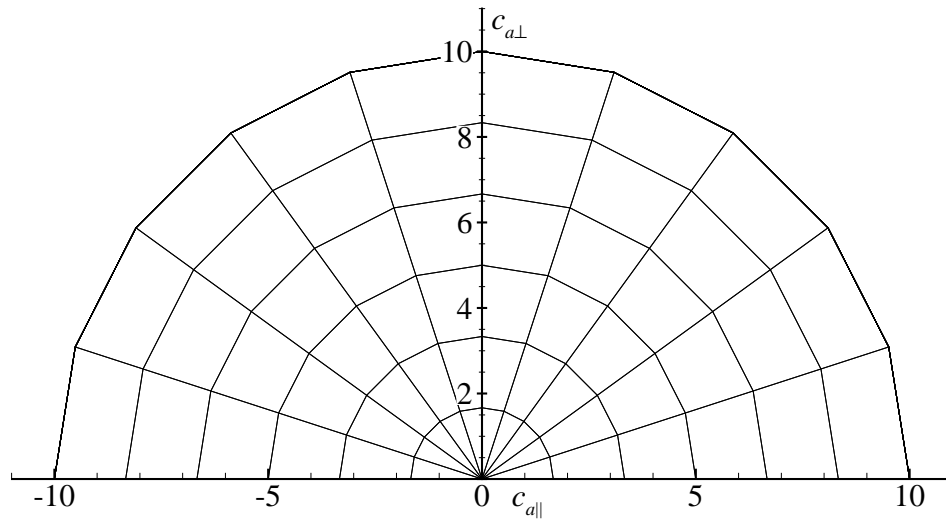


Fig. 3.2: Example semicircular grid. Here $m_x = 6$ and $m_y = 10$. The logical x-direction corresponds to the radial direction in real space, $|\mathbf{c}_a|$, and the logical y-direction corresponds to pitchangle, $\xi = \cos^{-1} \left(\frac{c_{a\parallel}}{|\mathbf{c}_a|} \right)$.

The rectangular grid is useful when a test particle distribution or kinetic distortion has a significant portion lying away from the origin, such as problems involving particle beams. The circular grid is useful when most of the important collisional physics lies within a couple of thermal speeds away from the origin, such as thermalization and conduction problems. Both grids can handle grid packing which means cells can be strategically concentrated near regions of velocity space where higher resolution is critical.

Returning now to the issue of accounting for degrees of freedom, the two different grid styles have slightly different degrees of freedom. In the case of the rectangular grid, the regularity condition demands that the coefficients, $F_{a,n,i}$, that correspond to values on nodes along the $c_{a\parallel}$ axis must vanish for all $n \neq 0$. These nodes lie along the logical y-axis. This yields the following total degrees of freedom:

$$[p \times \text{mx} (2N + 1) + 1] (p \times \text{my} + 1). \quad (3.13)$$

For the circular grid, all $|\mathbf{c}_a| = 0$ nodes along the logical y-axis collapse to a single node. The regularity condition is the same as above, yet the coefficients which must be removed have nodes in the logical x-axis. This yields the following total degrees of freedom:

$$p \times \text{mx} [(2N + 1) (p \times \text{my} - 1) + 2] + 1. \quad (3.14)$$

Solving the Fokker-Planck equation

For demonstrative purposes, we return momentarily to the generic time-discretized equation, Eq. (3.2). The way in which a partial differential equation gets transformed into an algebraic system of equations can be explained in the following way. A finite element solution can be viewed in terms of a variational formulation. Consider the residual of

Eq. (3.2)

$$\mathbb{R}(\Delta f) \equiv \Delta f - \theta \Delta t \mathbb{O}(\Delta f) - \Delta t \mathbb{O}(f^k), \quad (3.15)$$

where Δf is defined over the velocity domain Ω , and subject to appropriate boundary and initial conditions. Solutions to Eq. (3.2) satisfy $\mathbb{R}(\Delta F) = 0$, and the inner product between $\mathbb{R}(\Delta F)$ and any complex test function, $\phi(\mathbf{v})$ (whose conjugate is $\bar{\phi}$), must vanish

$$\langle \phi, \mathbb{R}(\Delta F) \rangle \equiv \frac{1}{2\pi} \int_{\Omega} d\mathbf{c}_a \bar{\phi}(\mathbf{c}_a) \mathbb{R}(\Delta F) = 0. \quad (3.16)$$

Here a factor of $\frac{1}{2\pi}$ is included in this definition to normalize the inner product of Fourier modes. To ensure that ΔF is a solution to Eq. (3.2), it is sufficient to demand that Eq. (3.16) vanish for a complete basis of test functions $\{\phi_i | i = 1, 2, \dots, \infty\}$. An approximation to ΔF is then found by demanding that Eq. (3.16) vanish for a finite subset of test functions, $\{\phi_i | i = 1, 2, \dots, i_{\max}\}$. In other words, the resulting set of i_{\max} equations, $\langle \phi_i, \mathbb{R}(\Delta F) \rangle = 0$, form a system of equations that approximate ΔF . Only an approximation is obtained in this manner since a finite subset of the complete basis of test functions is used.

Many numerical methods can be viewed as this type of variational formulation. For instance, a Fourier series solution is found by expanding ΔF as a truncated Fourier series. The test functions, ϕ_i , are then identified with the conjugate Fourier modes, and the resulting system of equations is used to solve for the Fourier coefficients. This general procedure can also be used to describe the general moment method, Laplace transforms, spectral methods in general, and many many others. Guided by the geometry of particular problems, different test functions and representations are chosen so the sequence of approximations leads to rapid convergence toward the exact solution.

My algorithm uses the Galerkin FEM scheme [19], which identifies the test functions, ϕ_i , with the functions found in the expansion of the approximate solution, Eq. (3.10). Thus the test functions used in Eq. (3.16) will be identified with the trial functions $\alpha_i e^{i\mathbf{v} \cdot \boldsymbol{\gamma}}$. The

solution to $\mathbb{R}(\Delta F) = 0$ is then approximated by enforcing

$$\left\langle \alpha_j e^{in'\gamma}, \Delta F - \theta \Delta t \mathbb{O}(\Delta F) \right\rangle = \left\langle \alpha_j e^{in'\gamma}, \Delta t \mathbb{O}(F^k) \right\rangle, \quad (3.17)$$

for $1 \leq j \leq I$, and $0 \leq n' \leq N$. If the differential operator, \mathbb{O} , is a linear operator (which is the case for the linearized collision operators), then

$$\sum_{n=-N}^N \sum_{i=1}^I \left\langle \alpha_j e^{in'\gamma}, \alpha_i e^{in\gamma} - \theta \Delta t \mathbb{O}(\alpha_i e^{in\gamma}) \right\rangle \Delta F_{n,i} = \left\langle \alpha_j e^{in'\gamma}, \Delta t \mathbb{O}(F^k) \right\rangle. \quad (3.18)$$

In principle this system of equations can be viewed as an inhomogeneous matrix equation,

$$\mathbf{A} \cdot \Delta \mathbf{F} = \mathbf{b}, \quad (3.19)$$

which could be solved using a numerical linear algebra solver. Even for simple simulations, this would require an extraordinary amount of memory to store every matrix element and invert the matrix \mathbf{A} . For example, for the rectangular grid shown in Fig. 3.1, with $p = 3$, and $N = 3$, there are 3937 independent $\Delta F_{n,i}$ for each species (cf. Eq. 3.13). This would require inverting a matrix with $(3937)^2 = 15,499,969$ elements. Note, because of the nature of finite elements, most of the entries in \mathbf{A} are zero. Such matrices are referred to as sparse.

Several simplifications are possible. For instance

$$\left\langle \alpha_j e^{in'\gamma}, \mathbb{O}(\alpha_i e^{in\gamma}) \right\rangle, \quad (3.20)$$

(where \mathbb{O} is the test particle operator), vanishes if α_j and α_i are nonzero in different cells, Ω_l . This causes most of the matrix elements of \mathbf{A} to vanish. Also, when the background flow is parallel to the cylindrical axis, only the $n = n' = 0$ elements of \mathbf{A} survive. One could, in principle, invert a very simple-looking matrix in this special case. However, it does not take much to spoil these conditions. For example, the field operator, collisional friction and

collisional energy exchange involve integrals of F_a and \mathbf{u} over the whole velocity domain. In this case the matrix \mathbf{A} would require elements which couple every single $\Delta F_{n',j}$.

Instead of forming and inverting the full matrix \mathbf{A} , my Fokker-Planck code makes use of the matrix-free, general minimum residual (GMRES) solver [20], which is implemented in NIMROD [10]. The GMRES solver is aided by constructing the $n' = n$ blocks of \mathbf{A} , which are inverted and applied in a preconditioning step. For magnetized plasmas, $n = 0$ dominates and coupling to $n \neq 0$ is relatively weak. This results in the GMRES solver quickly converging upon a solution.

For a differential operator, \mathbb{O} , such as the test particle operator, elements of \mathbf{A} are nonzero only when a test function is paired with an overlapping trial function, such as when the two functions are defined over the same cell or when their cells are contiguous. However, in an integro-differential operator, such as the field operator, every element of \mathbf{A} is nonzero, and the trial functions of every cell couple to one another. To avoid additional couplings that the field operator brings, our algorithm includes only the test particle operator in the preconditioning matrix.

Note about cylindrical coordinates

The coordinates used by my algorithm are normalized by the thermal speeds for the F_a being advanced, rather than being in SI units, or normalized by a common speed. The reason for this is that the thermal speeds set a reasonable scale for the bulk of the particles, and hence the domain where most of the Coulomb interactions take place. For distributions with comparable temperatures but disparate masses (such as protons and electrons) these scales are very different. By scaling \mathbf{v} by v_{Ta} I avoid having to construct multiple coordinates and grids for different species.

Now, the azimuthal angle must be referenced from a vector field well defined in physical space. This point is not terribly important for the current work, but needs to be addressed in

future works that may expand the functionality of this code to include spatial dimensions. Nevertheless, it is necessary to define this vector field when discussing vectors, such as the heat flow, flow velocity and collisional friction.

I define the azimuthal angle, γ , by vector fields $\hat{\mathbf{e}}_2(\mathbf{x})$ and $\hat{\mathbf{e}}_3(\mathbf{x})$, which form an orthonormal basis with $\hat{\mathbf{b}}$:

$$\mathbf{c}_a = c_{a\parallel}\hat{\mathbf{b}} + c_{a\perp}\hat{\mathbf{v}}_{\perp} = c_{a\parallel}\hat{\mathbf{b}} + c_{a\perp}(\hat{\mathbf{e}}_2\cos\gamma + \hat{\mathbf{e}}_3\sin\gamma). \quad (3.21)$$

It is anticipated future works will define the basis vector fields in relation to the magnetic geometry of a particular application. Regardless of how these vector field are defined, the basis vectors $\hat{\mathbf{v}}_{\perp}$ and $\hat{\boldsymbol{\gamma}}$ are simply $\hat{\mathbf{e}}_2$ and $\hat{\mathbf{e}}_3$ rotated by γ :

$$\begin{pmatrix} \hat{\mathbf{v}}_{\perp} \\ \hat{\boldsymbol{\gamma}} \end{pmatrix} = \begin{pmatrix} \cos\gamma & \sin\gamma \\ -\sin\gamma & \cos\gamma \end{pmatrix} \begin{pmatrix} \hat{\mathbf{e}}_2 \\ \hat{\mathbf{e}}_3 \end{pmatrix}. \quad (3.22)$$

Then a spatial vector, such as the flow velocity, with components $\mathbf{V} = V_{\parallel}\hat{\mathbf{b}} + V_x\hat{\mathbf{e}}_2 + V_y\hat{\mathbf{e}}_3$ can be written as

$$\mathbf{V} = V_{\parallel}\hat{\mathbf{b}} + (V_x\cos\gamma + V_y\sin\gamma)\hat{\mathbf{v}}_{\perp} + (-V_x\sin\gamma + V_y\cos\gamma)\hat{\boldsymbol{\gamma}}. \quad (3.23)$$

It is also important to define this relationship because frequently, it is necessary to compute differences of velocities, such as when computing \mathbf{z}_a , or \mathbf{u} , with two velocities given in different bases. A useful identity in this context is the velocity gradient

$$\nabla_{\mathbf{c}_a} = \hat{\mathbf{b}}\frac{\partial}{\partial c_{a\parallel}} + \hat{\mathbf{v}}_{\perp}\frac{\partial}{\partial c_{a\perp}} + \hat{\boldsymbol{\gamma}}\frac{1}{c_{a\perp}}\frac{\partial}{\partial \gamma} \quad (3.24)$$

$$= \hat{\mathbf{b}}\frac{\partial}{\partial c_{a\parallel}} + \hat{\mathbf{e}}_1\left(\cos\gamma\frac{\partial}{\partial c_{a\perp}} - \frac{\sin\gamma}{c_{a\perp}}\frac{\partial}{\partial \gamma}\right) + \hat{\mathbf{e}}_2\left(\sin\gamma\frac{\partial}{\partial c_{a\perp}} + \frac{\cos\gamma}{c_{a\perp}}\frac{\partial}{\partial \gamma}\right). \quad (3.25)$$

Weak form

As previously mentioned, only C^0 continuity is enforced, and second order derivatives of F_a must be avoided. This is done by partial integration of the system of equations in Eq. (3.17). The resulting equation after integration by parts, is called the weak form. This section gives detailed explanations of how this is done for the right side of Eq. (3.17) where \mathbb{O} includes the test particle and field operators. The other terms in Eq. (3.5) are then easily explained within this context. The method in which the terms on the left side of Eq. (3.17) are incorporated into the proposed Fokker-Planck code are also briefly explained.

Test particle operator

The conversion of the test particle operator to weak form is done by simply integrating by parts the outermost divergence. Defining

$$I_{ab,j}^{\text{T},n'} \equiv \frac{1}{2\pi} \int_{\Omega} d\mathbf{c}_a \alpha_j e^{-in'\gamma} \Delta t C_{ab}^{\text{T}}, \quad (3.26)$$

and partially integrating yields

$$I_{ab,j}^{\text{T},n'} = -\frac{\Delta t}{2\pi v_{Ta}} \sum_b \frac{\Gamma_{ab}}{2} \int_{\Omega} d\mathbf{c}_a \nabla_{\mathbf{c}_a} \left(\alpha_j e^{-in'\gamma} \right) \cdot \left[\left(\frac{2}{v_{Tb}} \frac{m_a}{m_b} \mathbf{z}_b F_a^k + \frac{1}{v_{Ta}} \nabla_{\mathbf{c}_a} F_a^k \right) \cdot \mathbf{D}_b^{\text{M}} \right], \quad (3.27)$$

where $\nabla_{\mathbf{c}_a} \left(\alpha_j e^{-in'\gamma} \right) = \left(\frac{\partial \alpha_j}{\partial c_{a\parallel}} \hat{\mathbf{b}} + \frac{\partial \alpha_j}{\partial c_{a\perp}} \hat{\mathbf{v}}_{\perp} - \frac{in'}{c_{a\perp}} \alpha_j \hat{\gamma} \right) e^{-in'\gamma}$. The two vector dot products in the integrand of this equation can then be evaluated explicitly and the integral computed.

Field operator

When working with the field operator, we choose to use the TR potential formalism in Eqs. (2.28 & 2.29). Using this formalism, the Fokker-Planck form of the collision operator

is written as

$$C(f_a, f_b) = -\frac{\Gamma_{ab}}{2} \nabla_{\mathbf{v}} \cdot \left(2 \frac{m_a}{m_b} f_a \nabla_{\mathbf{v}} h_b - \nabla_{\mathbf{v}} \nabla_{\mathbf{v}} g_b \cdot \nabla_{\mathbf{v}} f_a \right). \quad (3.28)$$

As with the test particle operator, the field operator on the right side of Eq. (3.5) is multiplied by $\frac{1}{2\pi} \alpha_j e^{-in'\gamma}$, and then integrated over velocity space,

$$I_{ab,j}^{\text{F},n'} \equiv \frac{1}{2\pi} \int_{\Omega} d\mathbf{c}_a \alpha_j e^{-in'\gamma} \Delta t C_{ab}^{\text{F}}. \quad (3.29)$$

The problem of producing a weak form of this expression (through partial integration) is different from many other finite element problems because the field operator is given in terms of the TR potentials rather than the kinetic distortion directly. There exist several partial integrations that can be performed with this integro-differential operator. For instance, it is possible, as with the case of the test particle operator, to remove the outer divergence in the collision operator by partial integration. Alternatively, the outer divergence could be distributed to each term with no partial integration being performed. In both cases, $\nabla_{\mathbf{v}} \nabla_{\mathbf{v}} g_b$ would need to be computed, which would be equivalent to computing the diffusion tensor, D_b . Rather than compute the components of this tensor, partial integration yields a weak form involving only the TR potentials and their gradients. One caveat to keep in mind is that partial integration can potentially introduce domain truncation errors from surface terms, which do not exactly vanish, but nonetheless are ignored in my algorithm.

The weak form used in this work was carefully selected to give the best results within the context of the conduction problem presented in Chapter 5. The sequence of partial integrations used to get to this form is outlined here, but the reason for selecting this particular selection of partial integrations will not be fully justified until Chapter 5. With this in mind,

Eq. (3.29) is expanded as

$$I_{ab,j}^{F,n'} = -\frac{\Delta t}{2\pi} \frac{\Gamma_{ab}}{2} \int_{\Omega} d\mathbf{c}_a \alpha_j e^{-in'\gamma} \times \left[2\frac{m_a}{m_b} \nabla_{\mathbf{v}} \cdot (f_a^M \nabla_{\mathbf{v}} h_b) - 2\nabla_{\mathbf{v}} f_a^M \cdot \nabla_{\mathbf{v}} h_b - \nabla_{\mathbf{v}} \nabla_{\mathbf{v}} f_a^M : \nabla_{\mathbf{v}} \nabla_{\mathbf{v}} g_b \right]. \quad (3.30)$$

The term, which involves $\nabla_{\mathbf{v}} \cdot (f_a^M \nabla_{\mathbf{v}} h_b)$, could be further expanded into two terms, one of which would involve the product $f_a^M F_b$. This is undesirable because $F_b(\mathbf{c}_b, t)$ is defined over \mathbf{c}_b , whereas the integration is over \mathbf{c}_a with $\alpha_j = \alpha_j(c_{a\parallel}, c_{a\perp})$, hence F_b would require interpolation on a velocity domain that is normalized by what can be a very different thermal speed. To avoid this complication, $\nabla_{\mathbf{v}} h_b$ is computed and the term in question is partially integrated. Furthermore, by using $\nabla_{\mathbf{v}} f_a^M = -\frac{2}{v_{Ta}} f_a^M \mathbf{z}_a$, $\nabla_{\mathbf{v}} \nabla_{\mathbf{v}} f_a^M = -\frac{2}{v_{Ta}^2} f_a^M (1 - 2\mathbf{z}_a \mathbf{z}_a)$, and $1 : \nabla_{\mathbf{v}} \nabla_{\mathbf{v}} g_b = \Delta_{\mathbf{v}} g_b = 2h_b$, $I_{ab,j}^{F,n'}$ can be written as

$$I_{ab,j}^{F,n'} = -\frac{\Delta t}{2\pi} \frac{\Gamma_{ab}}{2} \int_{\Omega} d\mathbf{c}_a \alpha_j e^{-in'\gamma} \left[2\frac{m_a}{m_b} \nabla_{\mathbf{v}} \cdot (f_a^M \nabla_{\mathbf{v}} h_b) + \frac{4}{v_{Ta}} f_a^M \mathbf{z}_a \cdot \nabla_{\mathbf{v}} h_b + \frac{4}{v_{Ta}^2} f_a^M h_b - \frac{4}{v_{Ta}^2} f_a^M \mathbf{z}_a \mathbf{z}_a : \nabla_{\mathbf{v}} \nabla_{\mathbf{v}} g_b \right]. \quad (3.31)$$

In order to integrate the last term by parts, the following identity is used

$$\begin{aligned} \alpha_j e^{-in'\gamma} f_a^M \mathbf{z}_a \mathbf{z}_a : \nabla_{\mathbf{v}} \nabla_{\mathbf{v}} g_b &= \nabla_{\mathbf{v}} \cdot \left[\alpha_j e^{-in'\gamma} f_a^M \mathbf{z}_a (\mathbf{z}_a \cdot \nabla_{\mathbf{v}} g_b) \right] \\ &\quad - \frac{f_a^M}{v_{Ta}} e^{-in'\gamma} \left[\overrightarrow{\alpha_j^{n'}} \cdot \mathbf{z}_a + 2\alpha_j (2 - z_a^2) \right] (\mathbf{z}_a \cdot \nabla_{\mathbf{v}} g_b) \end{aligned} \quad (3.32)$$

where $\overrightarrow{\alpha_j^{n'}} \equiv e^{in'\gamma} \nabla_{\mathbf{c}_a} (\alpha_j e^{-in'\gamma})$. Then, partially integrating the first, second and last terms

of Eq. (3.31) yields

$$\begin{aligned}
I_{ab,j}^{F,n'} = & -\frac{\Delta t}{2\pi} \frac{\Gamma_{ab}}{2} \int_{\Omega} d\mathbf{c}_a e^{-in'\gamma} f_a^M \left\{ -2 \frac{m_a}{m_b} \frac{v_{Tb}}{v_{Ta}} \vec{\alpha}_j^{n'} \cdot \nabla_{\mathbf{c}_b} \bar{h}_b \right. \\
& -4 \left(\frac{v_{Tb}}{v_{Ta}} \right)^2 \left[\vec{\alpha}_j^{n'} \cdot \mathbf{z}_a + 2\alpha_j (1 - z_a^2) \right] \bar{h}_b \\
& \left. +4 \left(\frac{v_{Tb}}{v_{Ta}} \right)^3 \left[\vec{\alpha}_j^{n'} \cdot \mathbf{z}_a + 2\alpha_j (2 - z_a^2) \right] \mathbf{z}_a \cdot \nabla_{\mathbf{c}_b} \bar{g}_b \right\}. \quad (3.33)
\end{aligned}$$

Here we have used

$$\bar{h}_b \equiv \frac{1}{v_{Tb}^2} h_b = \int d\mathbf{c}'_b F'_b \bar{u}_b^{-1} \quad (3.34)$$

$$\nabla_{\mathbf{c}_b} \bar{h}_b \equiv \frac{1}{v_{Tb}} \nabla_{\mathbf{v}} h_b = - \int d\mathbf{c}'_b F'_b \frac{1}{\bar{u}_b^3} \bar{\mathbf{u}}_b \quad (3.35)$$

$$\nabla_{\mathbf{c}_b} \bar{g}_b \equiv \frac{1}{v_{Tb}^3} \nabla_{\mathbf{v}} g_b = \int d\mathbf{c}'_b F'_b \frac{1}{\bar{u}_b} \bar{\mathbf{u}}_b, \quad (3.36)$$

where

$$\bar{\mathbf{u}}_b \equiv \frac{v_{Ta}}{v_{Tb}} \mathbf{c}_a - \mathbf{c}'_b. \quad (3.37)$$

This form is indicative of how these potentials are actually calculated. The integrals over γ in the TR potentials are convolutions of F_b with some form of $\bar{\mathbf{u}}_b$. NIMROD permits the use of dealiased Fast Fourier Transforms, by which γ is discretized into N_γ equispaced gyroangles and only $N = \frac{N_\gamma}{3} + 1$ independent complex Fourier modes are used in the expansion of F_a . Therefore, it is faster to compute the γ integrals within the TR potentials using the convolution theorem,

$$\frac{1}{2\pi} \int_0^{2\pi} d\gamma' f(\gamma') g(\gamma - \gamma') \approx \sum_{n=-N}^N f_n g_n e^{in\gamma}, \quad (3.38)$$

which requires the Fourier coefficients of various forms of $\bar{\mathbf{u}}_b$ to be precomputed. The fact these coefficients can be precomputed also greatly speeds up the calculation, with the caveat

that if thermal speeds change during the evolution, the potentials must be recomputed. This recomputation is done when any temperature changes by more than a specified tolerance.

Collisional friction, heating and implicit terms

In this subsection, the treatment of the other terms in Eq. (3.5) is summarized. Note the collisional friction, \mathbf{R}_{ab} , is related to the integrals, $I_{ab,j}^{T,n'}$ and $I_{ab,j}^{F,n'}$. The difference is that rather than multiplying the right side of Eq. (3.5) by $\frac{\Delta t}{2\pi}\alpha_j e^{-in'\gamma}$ and integrating, we multiply by $m_a v_{Ta}^4 \mathbf{c}_a$ and integrate. Thus

$$\mathbf{R}_{ab}^T = -m_a v_{Ta}^3 \frac{\Gamma_{ab}}{2} \int_{\Omega} d\mathbf{c}_a \left(\frac{2}{v_{Tb}} \frac{m_a}{m_b} \mathbf{z}_b F_a + \frac{1}{v_{Ta}} \nabla_{\mathbf{c}_a} F_a \right) \cdot \mathbf{D}_b^M, \quad (3.39)$$

$$\begin{aligned} \mathbf{R}_{ab}^F &= -2m_a v_{Ta}^4 \Gamma_{ab} \int_{\Omega} d\mathbf{c}_a f_a^M \\ &\times \left\{ -\frac{1}{2} \frac{m_a}{m_b} \frac{v_{Tb}}{v_{Ta}} \nabla_{\mathbf{c}_b} \bar{h}_b + \left(\frac{v_{Tb}}{v_{Ta}} \right)^3 \mathbf{z}_a \mathbf{z}_a \cdot \nabla_{\mathbf{c}_b} \bar{g}_b - \left(\frac{v_{Tb}}{v_{Ta}} \right)^2 \mathbf{z}_a \bar{h}_b \right. \\ &\quad \left. + 2\mathbf{c}_a \left[(z_a^2 - 1) \left(\frac{v_{Tb}}{v_{Ta}} \right)^2 \bar{h}_b + (2 - z_a^2) \left(\frac{v_{Tb}}{v_{Ta}} \right)^3 \mathbf{z}_a \cdot \nabla_{\mathbf{c}_b} \bar{g}_b \right] \right\}. \quad (3.40) \end{aligned}$$

It is also worth noting that since the velocity dependence is integrated away, the components of the collisional friction are calculated in a spatial coordinate system, $(\hat{\mathbf{b}}, \hat{\mathbf{e}}_2, \hat{\mathbf{e}}_3)$ (Eq. 3.22). Q_{ab} is calculated similarly with $\frac{\Delta t}{2\pi}\alpha_j e^{-in'\gamma}$ replaced by $\frac{m_a v_{Ta}^5}{2} z_a^2$:

$$Q_{ab}^T = -m_a v_{Ta}^4 \frac{\Gamma_{ab}}{2} \int_{\Omega} d\mathbf{c}_a \mathbf{z}_a \cdot \left[\left(\frac{2}{v_{Tb}} \frac{m_a}{m_b} \mathbf{z}_b F_a + \frac{1}{v_{Ta}} \nabla_{\mathbf{c}_a} F_a \right) \cdot \mathbf{D}_b^M \right], \quad (3.41)$$

$$\begin{aligned} Q_{ab}^F &= -2m_a v_{Ta}^5 \Gamma_{ab} \int_{\Omega} d\mathbf{c}_a f_a^M \left\{ -\frac{1}{2} \frac{m_a}{m_b} \frac{v_{Tb}}{v_{Ta}} \mathbf{z}_a \cdot \nabla_{\mathbf{c}_b} \bar{h}_b \right. \\ &\quad \left. + z_a^2 (z_a^2 - 2) \left(\frac{v_{Tb}}{v_{Ta}} \right)^2 \bar{h}_b + z_a^2 (3 - z_a^2) \left(\frac{v_{Tb}}{v_{Ta}} \right)^3 \mathbf{z}_a \cdot \nabla_{\mathbf{c}_b} \bar{g}_b \right\}. \quad (3.42) \end{aligned}$$

The quantities in Eq. (3.5) with the superscript M are calculated with the test particle operator by adding f_a^M to the kinetic distortion. The quantities with the Δ prefix are calculated in a subroutine that looks almost identical to the one that computes the right side of

Eq. (3.5), with the minor change that instead of using the kinetic distortion at the previous time step, quantities are calculated using the current iterate of the GMRES algorithm.

Numerical quadrature

Anywhere an integral is performed in velocity space, such as in the weak formulation of the Fokker-Planck equation, three independent integrals are performed using numerical quadrature. The γ integral is quickly computed using a Fast Fourier Transform algorithm. The remaining integrals over $c_{a\parallel}$ and $c_{a\perp}$ are performed using Gaussian quadrature [21]. This means that integrals in velocity space are first transformed to integrals in logical space,

$$\iint_{\Omega_i} dc_{a\parallel} dc_{a\perp} \rightarrow \int_0^1 \int_0^1 \mathcal{J} dx dy, \quad (3.43)$$

where x and y are the logical coordinates and \mathcal{J} is the Jacobian. Then integrals in logical space are approximated as sums,

$$\int_0^1 \int_0^1 dx dy f(x, y) = \sum_{i=1}^m w_i f(x_i, y_i), \quad (3.44)$$

where (x_i, y_i) is the i^{th} root of the m^{th} Legendre bi-polynomial, and the weights, w_i , are defined to give exact results when $f(x, y)$ is any polynomial of order $2m - 1$ or less in x and y . Given the test and trial functions are all possible two dimensional products of p -degree Lagrange polynomials, my algorithm uses $(p + 1)^2$ point Gaussian quadrature in each cell, giving exact results for integrands, which are the product of any test function with any trial function.

Since many of the integrals, such as $I_{ab,j}^{T,n'}$, $I_{ab,j}^{F,n'}$ and \bar{h}_b have integrands, which are not polynomials, this quadrature scheme is often not exact. Nevertheless, highly accurate results are obtained given sufficient grid resolution and polynomial degree. In the calculation of the TR potentials, the Fourier coefficients of \mathbf{u} are coupled, and several coefficients, \mathbf{u}_n ,

must be computed in order to use the first few in the convolution theorem with $F_{b,n}$. If $N + 1$ is the number of independent coefficients in the Fourier expansion of $F_{b,n}$, and $N_{\mathbf{u}} + 1$ is the number of independent coefficients in the Fourier expansion of \mathbf{u} , then my algorithm uses $N_{\mathbf{u}} = \max \{12, N\}$ to ensure an accurate calculation involving the necessary \mathbf{u}_n .

CHAPTER 4

THE TEST PARTICLE OPERATOR

Chang and Cooper [22] described solving the FP equation best when they wrote, “The underlying objectives of any practical numerical scheme are the following: (1) large time and velocity steps, (2) accuracy and stability, and (3) preservation of any intrinsic properties implied by the Fokker-Planck equation.” One may enlarge this list to include general applicability, which is the objective of a code that can be reliably used in multiple applications. It is by these standards the methods of this work are judged.

This chapter will discuss several problems, which were solved using the algorithm implementing the δf linearized collision operator, i.e., the test particle operator. Some of the problems were chosen to show this algorithm reproduces previously accepted results. These benchmark calculations are used to illustrate the superior convergence properties of the finite element method, a primary reason for considering its use. These calculations are also used to examine how well this algorithm preserves the intrinsic conservation laws implied by the collision operator. Additional problems demonstrate the algorithm’s capacity for going beyond gyro-averaged kinetics. The chapter summary returns to the three objectives stated by Chang and Cooper, and summarizes how well the algorithm is able to fulfill these objectives.

Resistivity of an unmagnetized Lorentz plasma

This section discusses a comparison of the analytic form of the resistivity of an unmagnetized plasma using the Lorentz gas approximation [23] with results obtained by using my algorithm. For test particle electrons scattering off a background of immobile ions, $f_i(\mathbf{v}) = n_i \delta(\mathbf{v})$, the Coulomb collision operator reduces to the Lorentz pitch angle scattering operator,

$$C(F_e, f_i^M) = \frac{n_e \Gamma_{ei}}{2} \frac{\partial}{\partial \mathbf{v}} \cdot \left(\frac{v^2 \mathbf{I} - \mathbf{v} \mathbf{v}}{v^3} \cdot \frac{\partial F_e}{\partial \mathbf{v}} \right). \quad (4.1)$$

Although the Lorentz operator does not correctly take into account the collisional effects on the ion distribution function nor the slowing down of the electrons, this operator conserves energy as well as density.

If a weak electric field, $\mathbf{E} \equiv E\hat{\mathbf{b}}$, is present, and the initial electron distribution is Maxwellian, i.e., $F_e(\mathbf{v}, t=0) = 0$, the electrons will accelerate until collisions with ions balance the electric force. The steady state solution is obtained by solving the linearized first order Boltzmann equation

$$\frac{q_e}{m_e} \mathbf{E} \cdot \frac{\partial f_e^M}{\partial \mathbf{v}} = \frac{n_e \Gamma_{ei}}{2} \frac{\partial}{\partial \mathbf{v}} \cdot \left(\frac{v^2 \mathbf{I} - \mathbf{v} \mathbf{v}}{v^3} \cdot \frac{\partial F_e}{\partial \mathbf{v}} \right), \quad (4.2)$$

which has the solution,

$$F_e = \frac{2q_e E}{n_e m_e v_{Te}^2 \Gamma_{ei}} v^3 v_{\parallel} f_e^M. \quad (4.3)$$

Calculating the current density, $\mathbf{J} = q_e \int d\mathbf{v} \mathbf{v} F_e$, and defining electrical resistivity through the relationship $\eta_L \mathbf{J} = \mathbf{E}$, leads to an electrical resistivity

$$\eta_L = \frac{Z q_e^2 \ln \Lambda_{ei}}{32 \sqrt{\pi} \epsilon_0^2 m_e v_{Te}^3}, \quad (4.4)$$

where $Z \equiv q_i / |q_e|$ is the ion charge in units of the electron charge.

As a tools to estimate errors in the finite element/Fourier representation, the mean point-wise error of a test particle distribution function, $F_a(\mathbf{v}, t)$, is defined as

$$\varepsilon(t) \equiv \frac{1}{M} \sum_{i=1}^M |F_a(\mathbf{v}_i, t) - F_a^{\text{exact}}(\mathbf{v}_i, t)|. \quad (4.5)$$

Here \mathbf{v}_i are $M = 100 \times 100$ equally spaced points throughout the domain, and F_a^{exact} is the distribution function found in Eq. (4.3).

Table 4.1 demonstrates the exponential convergence of the steady state solution, F_e , as the polynomial order, p , is increased. We refer to this as p -type refinement. The resistivity

Table 4.1: p -type refinement of the electrical resistivity, η_L , of a Lorentz plasma in response to an electric field, $E = 10^{-5}$ V/m, and the mean pointwise error, ε , cf. Eq. (4.5). In this example, the electron temperature was set to $T_e = 2.25$ keV. The velocity domain is rectangular, with $(v_\perp, v_\parallel) \in [0, 10v_{Te}] \times [-10v_{Te}, 10v_{Te}]$ and a grid resolution of 16×32 . T_e is given in units of K.

p	$\eta_L (\Omega\text{-cm}) \times T_e^{3/2} / (Z \ln \Lambda_{ei})$	$\varepsilon[F_e] (s^3/m^6)$
1	3.697866×10^3	4.83×10^{-12}
2	3.797414×10^3	4.91×10^{-13}
3	3.797144×10^3	2.98×10^{-14}
4	3.797167×10^3	6.13×10^{-15}
Exact	3.797282×10^3	0

is accurate for the lowest few p , since it depends only on the flow moment of F_e . The resistivity, with a more detailed account of the collisional effects on both the ions and the electrons, was computed by Landshoff [24] and Spitzer and Härm [25]. However, to replicate this correct resistivity, the CEL kinetic equation must be used, which includes the field terms to be discussed in the next chapter.

Thermalization of test particles

To further test the convergence properties of the FEM treatment of velocity space, consider a tenuous ion Maxwellian test particle distribution thermalizing due to collisions with a background ion Maxwellian of different temperature. Neither distribution is flowing. The density of the field particles, n_i , and test particles, n_{test} , are 10^{20} m^{-3} and 10^{18} m^{-3} , respectively. The initial temperature of the test particles is $T_{\text{test}} \equiv 1.5$ keV. The background has a temperature of $T_i = 2.25$ keV for heating, or 1.125 keV for cooling.

The calculation of the evolution of the test particle distribution was also performed by Xiong et al. [8]. For consistency with Ref. [8], $\ln \Lambda_{ii} = 16$, $m_i = m_D$ and $q_i = e$, where m_D and e are the mass and charge of the deuteron, respectively. In this case the field particle thermal speed is $v_{Ti} = 4.64 \times 10^5$ m/s, and the time step is normalized by the characteristic collision time, $\tau = \frac{4\pi\varepsilon_0^2 m_D^2 v_{Ti}^3}{n_i e^4 \ln \Lambda_{ii}}$. These parameters are used to normalize velocity space coor-

ordinates, $(v_{\perp}, v_{\parallel})$, and time, t . Finally, as in the previous resistivity calculation, this problem only involves the $n = 0$ Fourier coefficient, hence the preconditioning step of the GMRES algorithm provides the inverse for the full problem.

Temperature evolution

If one assumes the test distribution remains Maxwellian during the thermalization process, the temperature evolves as [14]

$$\frac{dT_{\text{test}}}{dt} = -\frac{8}{3\sqrt{\pi}} \frac{T_{\text{test}} - T_i}{\tau_l^{i/i}}, \quad (4.6)$$

where $\tau_l^{i/i}(\varepsilon) = \frac{\sqrt{m_D}}{\pi\sqrt{2}q_i^4} \frac{\varepsilon^{3/2}}{\ln\Lambda_c n_i}$, and $\varepsilon = T_{\text{test}} + T_i$. The evolution given by Eq. (4.6) is only approximate since a nonmaxwellian part develops in the thermalization process. Nevertheless, it gives a standard by which to compare our results.

The temperature evolution for the heating and cooling problems are shown in Figs. 4.1 and 4.2 as the number of finite element cells is increased. We refer to this as h -type refinement. Note, the nonmaxwellian elements of the solution slow down the evolution in comparison to Eq. (4.6) and for both the heating and cooling problems the 5×5 and 20×20 grid solutions are nearly identical.

Comparison with the finite volume method in Ref. [8] is straightforward. There the coordinates are the normalized particle energy and magnetic moment, the maximum value for each is $E_{\text{max}} = \mu_{\text{max}} = 16$, and an external magnetic field of $B = 1.2\text{ T}$ is present. This corresponds roughly to setting the parameters of our code to have a maximum particle velocity of $(v_{\perp\text{max}}, v_{\parallel\text{max}}) = (5v_{Ti}, 5v_{Ti})$. One grid used in Ref. [8] is 20×20 , with 15 coefficients for the polynomial representation per cell, giving 6000 degrees of freedom, globally.

Alternatively, the finite element representation, using Lagrange polynomials of degree

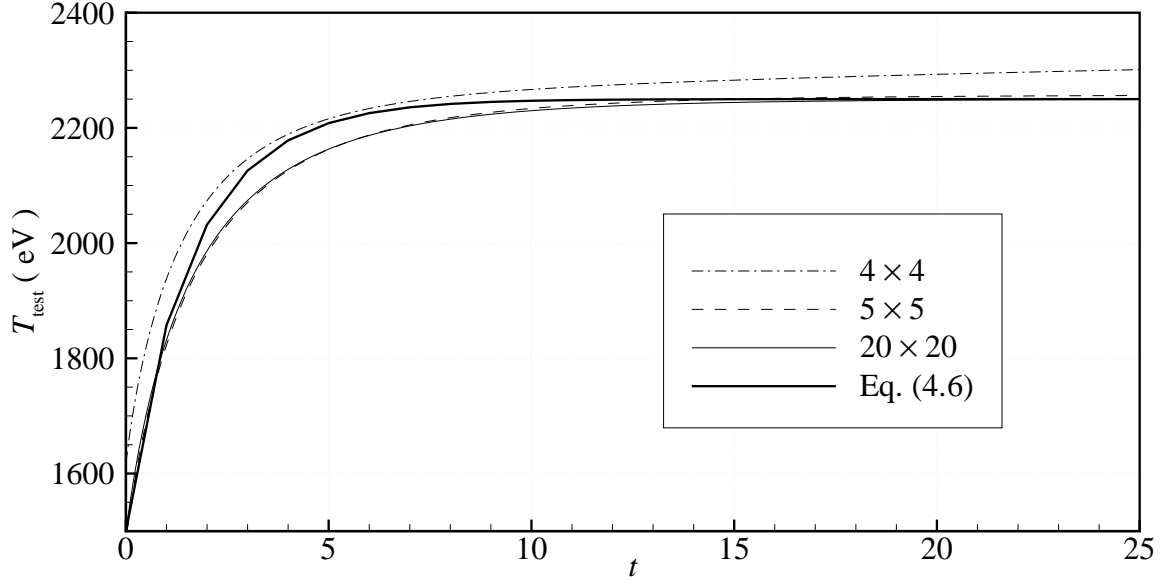


Fig. 4.1: The heating of a tenuous Maxwellian ion distribution scattering off of a higher energy, 2.25 keV, Maxwellian ion distribution with $p = 4$.

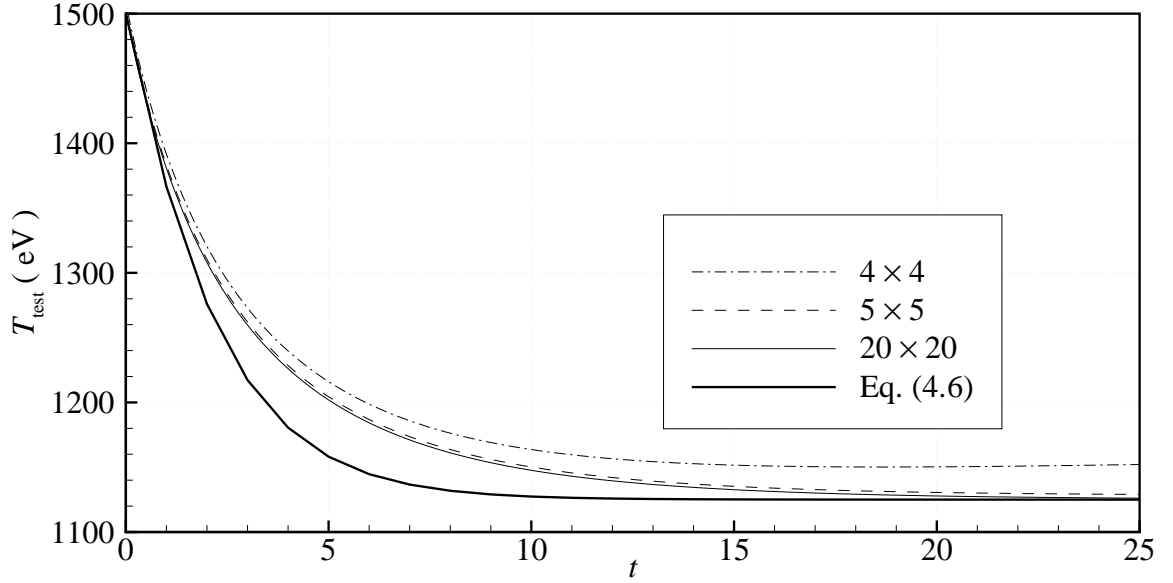


Fig. 4.2: The cooling of a tenuous Maxwellian ion distribution scattering off of a lower energy, 1.125 keV, Maxwellian ion distribution with $p = 4$.

p on a $\xi \times \xi$ grid, gives a total of $(\xi \cdot p + 1)^2$ degrees of freedom, cf. Eq. (3.13). To achieve roughly the same number of degrees of freedom a 20×20 grid, and polynomial

degree $p = 4$ is used. Comparing Figs. 4.1 and 4.2 with Figs. 6 and 7 in [8] shows that convergence occurs much more rapidly under h -type refinement with the proposed algorithm than in the finite volume method. For example, the finite element solution on a 5×5 grid, with 441 degrees of freedom, is comparable to the finite volume solution on a 60×60 grid, with 54,000 degrees of freedom.

Basic convergence properties

This section focuses on the heating problem to demonstrate the basic convergence properties of the FEM. The grid resolution (h -type refinement) and polynomial order (p -type refinement) are increased while computing the mean pointwise error, $\varepsilon(t)$ in Eq. (4.5), at $t = 0$ and 25τ . Here F_i^{exact} is the distribution function found with the greatest polynomial degree and grid resolution. For these cases, the refinement procedure ends with $p_{\max} = h_{\max} = 7$. The velocity space grid has $(v_{\perp}, v_{\parallel}) \in \Omega = [0, 10v_{Ti}] \times [-10v_{Ti}, 10v_{Ti}]$, with $2^h \times 2^{h+1}$ cells.

Typically in a FEM discussion, h would refer to a characteristic length of each cell, and h -type refinement (decreasing the cell size) would lead to algebraic convergence. In this refinement, the cell size decreases by increasing the number of cells in the domain. The convergence with this h -type refinement is seen in Fig. 4.3. The exponential convergence, seen in Fig. 4.4, is commonly observed under p -type refinement. Note the grid resolution and polynomial degree must be large enough to properly resolve the initial condition. For example, in the case where $p = 1$, for small grid resolution (e.g. $h = 1$, and 2) the initial error is quite large, and only increases as the distribution function evolves. The cases of extremely low resolution are considered here simply for demonstrative purposes.

Another important refinement process to consider is the convergence of a solution as the time step Δt is reduced. Figure 4.5 shows the error, after 25 collision times, associated with the heating problem, with a 5×5 grid and $p = 4$, using a fully implicit, $\theta = 1.0$, and a

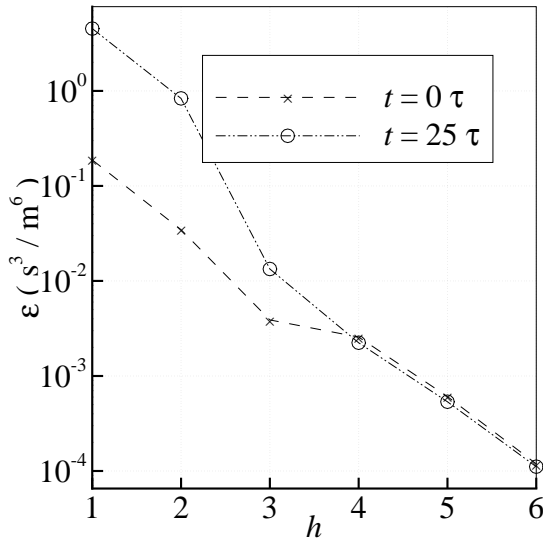


Fig. 4.3: The mean error, $\varepsilon(t)$, associated with using a $2^h \times 2^{h+1}$ grid, and $p = 1$, bilinear trial functions showing h -type refinement, with $h_{\max} = 7$. ε is calculated at $t = 0 \tau$ and $t = 25 \tau$.

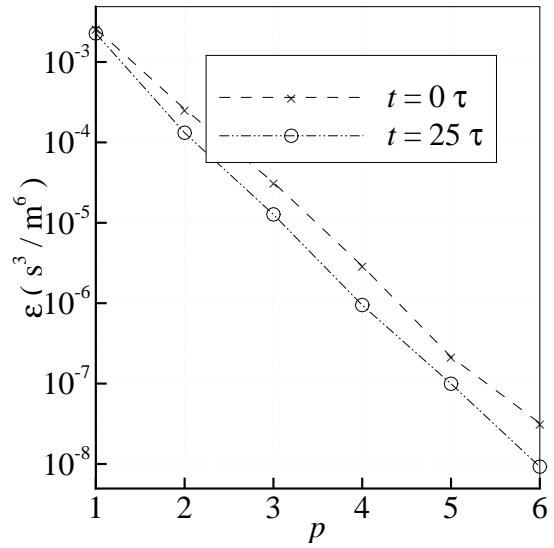


Fig. 4.4: The mean error, $\varepsilon(t)$, associated with using a 16×32 grid and p -order Lagrange polynomial trial functions showing p -type refinement, with $p_{\max} = 7$. ε is calculated at $t = 0 \tau$ and $t = 25 \tau$.

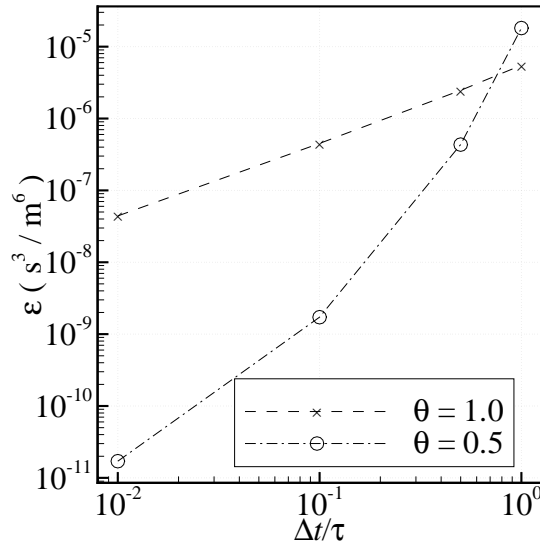


Fig. 4.5: The mean error, $\varepsilon(t = 25 \tau)$, associated with using a 5×5 grid, and $p = 4$, bilinear trial functions showing time step refinement, using fully implicit, $\theta = 1$, and $\theta = 0.5$ implicit time advance [9].

semi-implicit, $\theta = 0.5$, advance. The error of the fully implicit advance is seen to be $\mathcal{O}(\Delta t)$, while the error of the semi-implicit advance is $\mathcal{O}(\Delta t^2)$ for small time steps [9]. The semi-implicit scheme can be used to accurately resolve dynamic processes which occur before equilibrium is reached. However, the fully implicit scheme can take large, stable time steps to quickly advance to time asymptotic solutions.

Density conservation

This section discusses domain truncation error. Because the δf linearization assumes a stationary Maxwellian background, $C(f_a^M, f_b)$ is ignored, and we do not conserve momentum and energy. Nevertheless, the density of the test particle distribution should be conserved.

The velocity space domain must be large enough for the distribution function to evolve in. If the domain is too small, domain truncation leads to source and/or sink errors at the boundary. To illustrate this problem, consider the Spitzer heating problem with $p = 3$, and a 4×8 grid on the domain $(v_\perp, v_\parallel) \in [0, 2.5 v_{Ti}] \times [-2.5 v_{Ti}, 2.5 v_{Ti}]$. Although the residual error from the initial condition is tolerable, as the particles pick up speed by colliding with the hotter background particles some escape the domain, reducing the number density, cf. Figs. (4.6 & 4.7). Table 4.2 shows the relative error in the number density after 50 collision times as the velocity space domain is increased, keeping the grid resolution fixed.

The smallest error, due to the finite element representation, found in Fig. 4.4 can be used to estimate the relative error in test particle density due to the finite element representation,

$$\int d\mathbf{v} \frac{|F_i(\mathbf{v}_i, t) - F_i^{\text{exact}}(\mathbf{v}_i, t)|}{n_{\text{test}}(t = 0 \tau)} \approx \frac{\varepsilon \int_{\Omega} d\mathbf{v}}{n_{\text{test}}(t = 0 \tau)} \approx 6 \times 10^{-6}, \quad (4.7)$$

where Ω is the cylindrical domain used to calculate ε in the section, Basic convergence properties. The last two tests in Table 4.2 have a domain truncation error much smaller than the error due to the FEM representation. This demonstrates the domain truncation

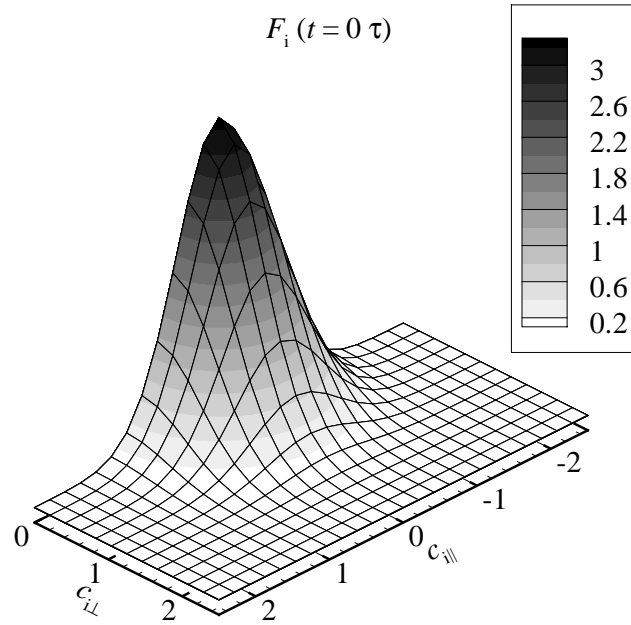


Fig. 4.6: The finite element representation of the initial condition $F_i(t=0 \tau)$ is well resolved with polynomial degree $p=3$, and grid resolution 4×8 . The vertices of the overlaid mesh are the nodes of the Lagrange polynomials.

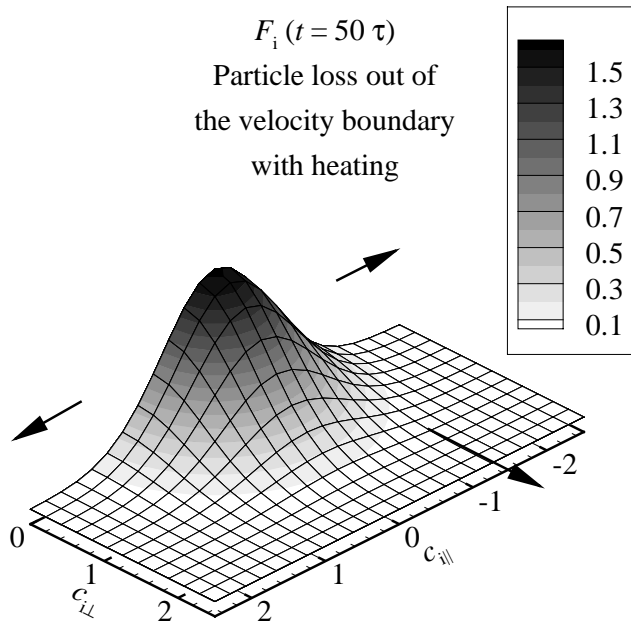


Fig. 4.7: Test distribution, F_i , at $t=50 \tau$. Because the velocity domain is too small, some particles gain energy from collisions with the hotter background and escape causing the density to decrease.

Table 4.2: Maintaining a constant cell size, but increasing the velocity domain shows improved conservation in n_{test} and mitigated domain truncation error. Note the error for the larger domains is much smaller than the error due to the FEM representation itself $\approx 6 \times 10^{-6}$.

p	h	$v_{\perp \text{max}}$	$ v_{\parallel \text{max}} $	$\frac{n_{\text{test}}(t=50\tau) - n_{\text{test}}(t=0\tau)}{n_{\text{test}}(t=0\tau)}$
3	2	$2.5 v_{Ti}$	$2.5 v_{Ti}$	-9.82×10^{-2}
3	3	$5.0 v_{Ti}$	$5.0 v_{Ti}$	-2.11×10^{-9}
3	4	$10.0 v_{Ti}$	$10.0 v_{Ti}$	5.00×10^{-16}

error can be mitigated to the extent that the dominant error comes from the finite element method itself. Also, if the background is flowing, it can drag test particles toward the edge of the velocity domain. This must also be taken into consideration when deciding how large to construct the velocity space domain.

Tenuous beam of test particles

Next consider the evolution of a tenuous beam of electrons given by

$$F_e(v_{\parallel}, v_{\perp}, t=0) = \Phi e^{-[(v_{\parallel} - v_{\parallel 0})^2 + (v_{\perp} - v_{\perp 0})^2] / v_{T\text{test}}^2}, \quad (4.8)$$

scattering off background species of electrons and ions with equal density and temperature. The background ion and electron temperature, $3.30 \times 10^6 \text{ K}$ (284 eV), corresponds to a background electron thermal speed of $v_{Te} = 10^7 \text{ m/s}$. For demonstrative purposes, both Maxwellian background distributions have a finite flow of $\mathbf{V}_e = \mathbf{V}_i = \frac{1}{2} v_{Te} \hat{\mathbf{b}}$. It is also assumed that $v_{\perp 0} = v_{\parallel 0} = 2.5 v_{Te}$, $v_{T\text{test}} = v_{Te}$, and $\Phi = 2.028 \times 10^{-5} \text{ s}^3 \text{ m}^{-6}$. This choice of Φ yields a beam density of $n_{\text{test}} = 10^{18} \text{ m}^{-3}$. The velocity domain has $v_{\perp \text{max}} = |v_{\parallel \text{max}}| = 10 v_{Te}$. The Lagrange polynomials have degree $p = 3$, and the grid resolution is 16×32 . The FP equation is solved using the $\theta = 0.5$ advance with time steps one hundredth of the collision time $\tau_{ee} = \frac{4\pi\epsilon_0^2 m_e^2 v_{Te}^3}{n_e q_e^4 \ln \Lambda_{ee}}$ where $n_e = 10^{20} \text{ m}^{-3}$ and $\ln \Lambda_{ee} = 16$.

Figure 4.8 illustrates the time dependent evolution of this electron beam. As expected,

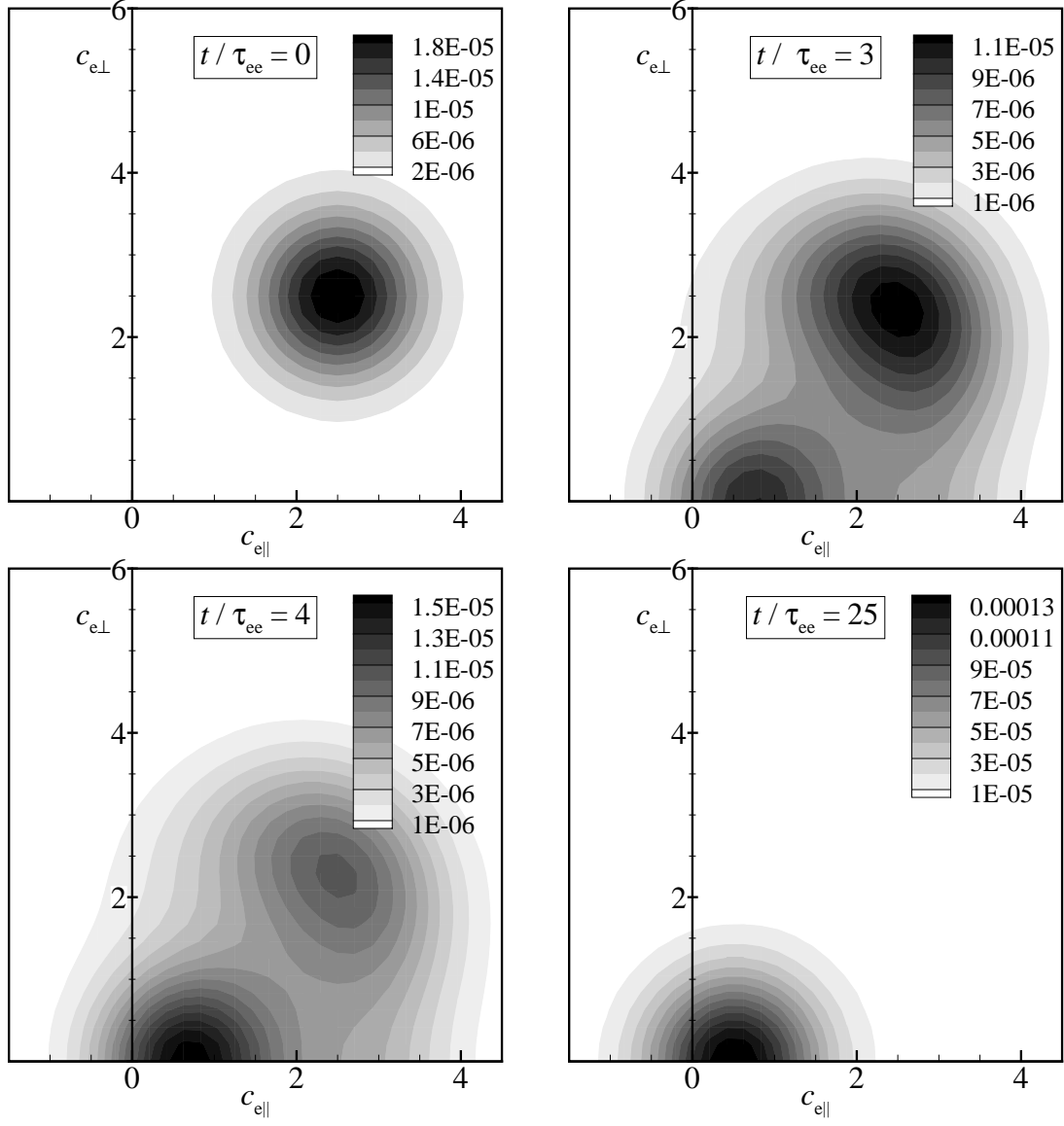


Fig. 4.8: The evolution of a tenuous beam of electrons scattering off flowing electron and ion Maxwellian backgrounds with $V_{\parallel} = \frac{1}{2}v_{Te}$. Here $p = 3$, and a grid resolution of 16×32 is used. Although the calculation uses $v_{\perp \max} = |v_{\parallel \max}| = 10v_{Te}$, these plots are scaled to show detail. The significant changes take place within the first few collision times, after which the beam thermalizes with the background and ultimately acquires the same flow as the background distributions.

the electrons experience diffusion in velocity space, pitch angle scattering, as well as dynamic friction. The beam's flow velocity slows until it matches the background flow, and the beam's temperature eventually assumes the background temperature. Most of the evo-

lution takes place roughly within the first six collision times.

Perpendicular flow

In this section, we explore two examples which require $n > 0$ terms in the Fourier representation of F_e . We consider an ion test particle distribution with no flow scattering off of a flowing ion background. Both test and field distributions are Maxwellian with the same initial temperature, $T_i = 1 \text{ keV}$. The initial test and field particle distributions can be written as

$$F_i = \frac{n_{\text{test}}}{\pi^{3/2} v_{Ti}^3} \exp \left[- \left(\frac{\mathbf{v}}{v_{Ti}} \right)^2 \right], \quad (4.9)$$

$$f_i^M = \frac{n_i}{\pi^{3/2} v_{Ti}^3} \exp \left[- \left(\frac{\mathbf{v} - \mathbf{V}_i}{v_{Ti}} \right)^2 \right], \quad (4.10)$$

where $n_{\text{test}} = 10^{18} \text{ m}^{-3}$, $n_i = 10^{20} \text{ m}^{-3}$, and $v_{Ti} = 3.096 \times 10^5 \text{ m/s}$. As in section, Thermalization of test particles, the Coulomb logarithm is taken to be $\ln \Lambda_{ii} = 16$, the ions are deuterons, and the characteristic collision time is $\tau = \frac{4\pi\epsilon_0^2 m_D^2 v_{Ti}^3}{n_i e^4 \ln \Lambda_{ii}}$. Recall the Cartesian unit vectors, $(\hat{\mathbf{e}}_2, \hat{\mathbf{e}}_3)$, explained in the subsection, Note about cylindrical coordinates, esp. Eq. (3.22). Without loss of generality, we choose coordinates such that $\hat{\mathbf{e}}_2 \parallel \mathbf{V}_i$. In the first case, we set $\mathbf{V}_i = 0.1 v_{Ti} \hat{\mathbf{e}}_2$, and in the second case $\mathbf{V}_i = v_{Ti} \hat{\mathbf{e}}_2$. These examples require a representation of the test particle distribution, Eq. (3.10), with more than one term in the Fourier series because \mathbf{z}_i , in Eq. (3.27), and the diffusion tensor in Eq. (2.49) depend on γ .

Figure 4.9 shows in both cases, the test particles accelerate until the flow matches the background flow. For the slower background, this acceleration occurs more quickly. Additionally, the test particle temperature remains roughly constant when the background flow is small compared to the thermal speed, $\mathbf{V}_i = 0.1 v_{Ti} \hat{\mathbf{e}}_1$. However, the temperature actually

increases as an initial response to collisions with the flowing background, $\mathbf{V}_i = v_{Ti} \hat{\mathbf{e}}_1$. This describes an initial spreading in addition to acceleration of the test particle distribution. After three collision times the acceleration decreases and the spread in the distribution begins to shrink. The test particles cool until equilibrium with the background is achieved. Note the equilibrium temperature and flow are not a weighted average between the field and test particles because the δf approach linearizes about a fixed Maxwellian background. Additionally, if the field terms had been included in the FP equation, then energy and momentum would also be conserved throughout the equilibration process.

As a means of estimating the relative importance of Fourier modes, we sum the absolute values of the complex Fourier coefficients, $F_{i,n,j}^k$, (cf. Eq. (3.10)) defined at the vertex nodes of the FEM representation,

$$\Xi_n(t) \equiv \sum_{j \in \text{vertex nodes}} \left| F_{i,n,j}^k(t) \right|. \quad (4.11)$$

Figure 4.10 shows how the Ξ_n 's evolve during equilibration for the case of small and large background flows. We see the Fourier series converges more quickly for $\frac{V_{i\perp}}{v_{Ti}} \ll 1$. Equation (3.27) indicates the number of Fourier modes needed depends directly on the magnitude of perpendicular background flow.

The mode coupling expressed in Eq. (3.27) was confirmed to be very weak in constructing Fig. 4.10, as the $\Xi_n(t)$ common among the $N = 1, 2$, and 5 representations differ very little. This coupling is even weaker in cases where $V_{i\perp}/v_{Ti}$ is small. As previously discussed, the solution converges with far fewer Fourier coefficients for small $V_{i\perp}/v_{Ti}$. The mode coupling had the most significant effect within the first few time steps, where the GMRES solver took the most iterations. GMRES iterations decreased until the steady state was reached. In the case where $V_{i\perp} = v_{Ti}$ the solver took roughly ten times as many iterations as in the case where $V_{i\perp} = 0.1 v_{Ti}$.

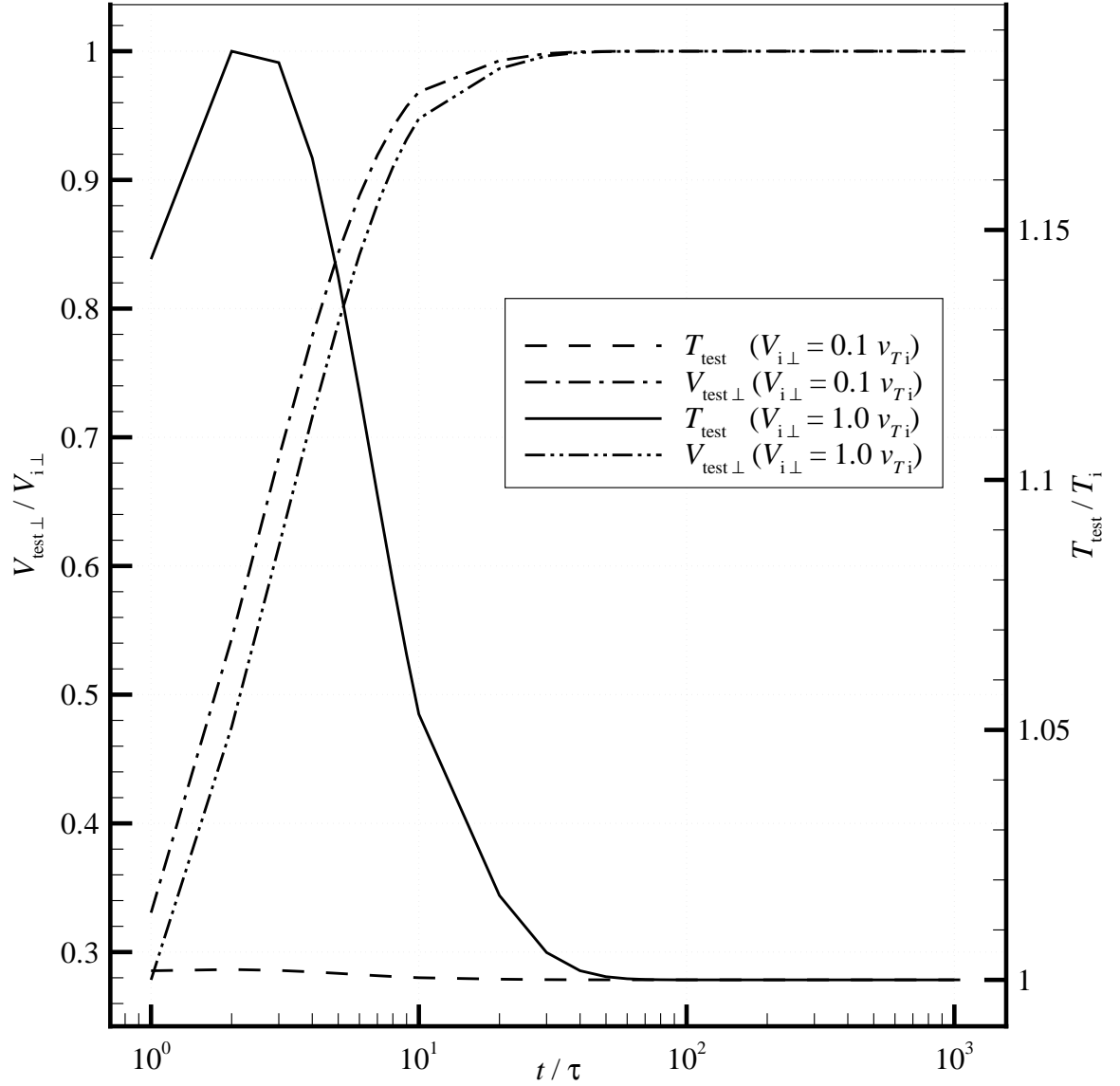


Fig. 4.9: The perpendicular flow, $V_{\text{test}\perp}$, and temperature, T_{test} , of an initially unshifted Maxwellian ion test distribution scattering off a flow-shifted Maxwellian field distribution with a flow of (1) $V_{i\perp} = 0.1 v_{Ti}$, and (2) $V_{i\perp} = v_{Ti}$. In both cases, the velocity domain has a 16×32 mesh with $v_{\perp\text{max}} = v_{\parallel\text{max}} = 10 v_{Ti}$, and $p = 3$.

It is instructive to consider this problem in the frame of the background species, in which case, mode coupling does not exist. In this case the initial condition for our test particles would be represented by a Fourier sum and $n > 0$ coefficients would decay as $t \rightarrow \infty$. Nevertheless, we would be required to take the Fourier transform of a flow-

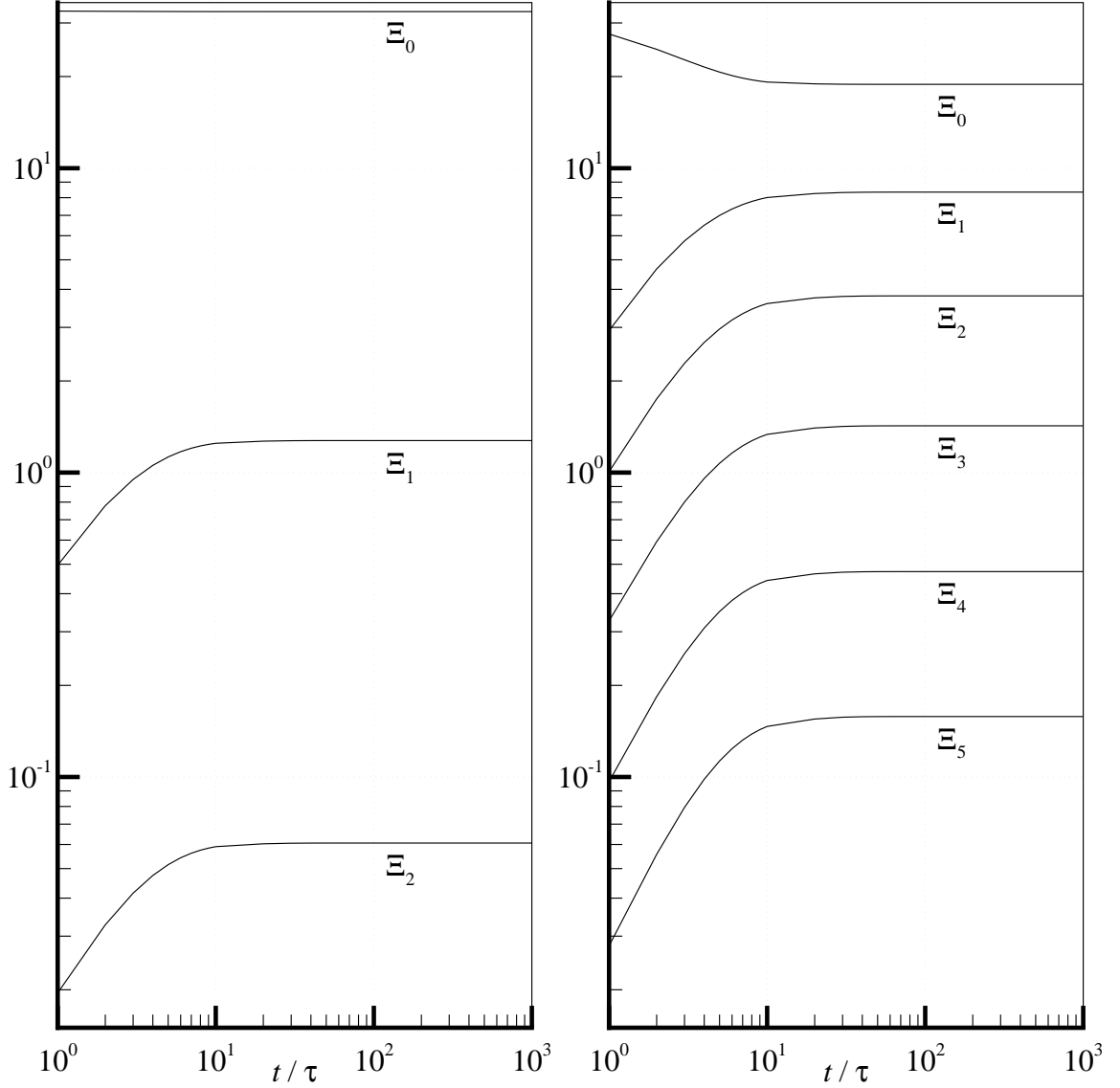


Fig. 4.10: Ξ_n , calculated from Eq. (4.11) for the two examples in Fig. 4.9. Left: $V_{i\perp} = 0.1 v_{Ti}$ and $N = 2$ in the Fourier representation. Right: $V_{i\perp} = v_{Ti}$ and $N = 5$ in the Fourier representation. In the second case more Fourier modes are required to represent the distribution function.

shifted Maxwellian test particle distribution to provide our initial condition. Treating the γ dependent cross term, $v_{i\perp} V_{i\perp} \cos \gamma$, in the exponent of Eq. (2.15) with the identity $\exp(x \cos \gamma) = I_0(x) + 2 \sum_{n=1}^{\infty} I_n(x) \cos(n\gamma)$ [21], where the I_n are modified Bessel functions of the first kind, it can be shown that the n^{th} Fourier coefficient of the flow-shifted

Maxwellian test particle distribution is

$$F_{i,n}(t=0) = \frac{n_{\text{test}}}{\pi^{3/2} v_{Ti}^3} \exp\left(-\frac{v^2 + V_{i\perp}^2}{v_{Ti}^2}\right) (-1)^n I_n\left(2 \frac{v_{\perp} V_{i\perp}}{v_{Ti}^2}\right), \quad (4.12)$$

where $v^2 = v_{\parallel}^2 + v_{\perp}^2$.

The modified Bessel functions of the first kind are shown graphically in Fig. 4.11. I_0 is

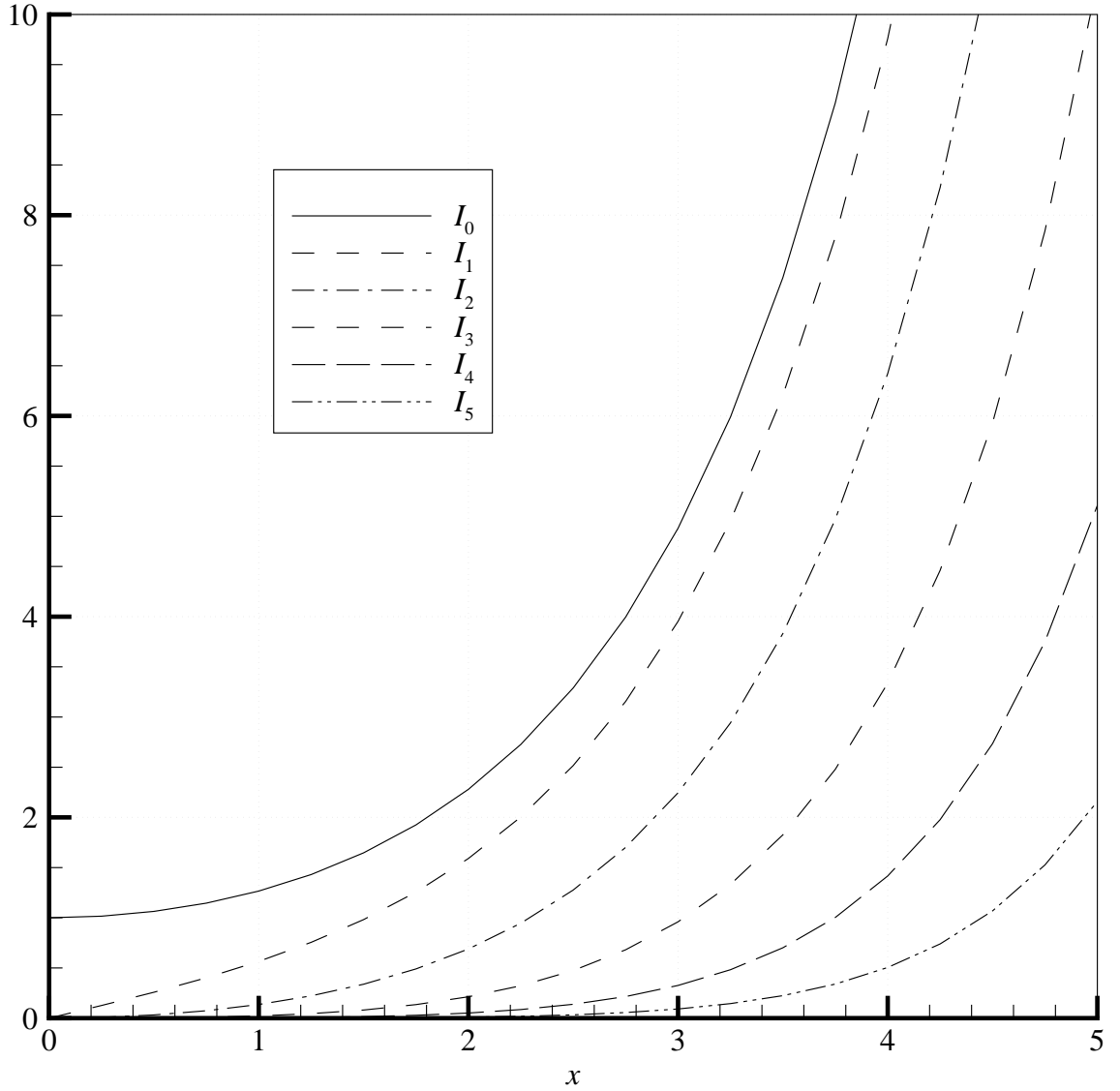


Fig. 4.11: Modified Bessel functions of the first kind, I_n , in Eq. (4.12).

the only function that has a nonzero value when its argument, $\left(x = 2 \frac{v_{\perp} V_{i\perp}}{v_{Ti}^2}\right)$, is zero. Thus, if $V_{i\perp} = 0$, only the $n = 0$ mode is needed, and the form of Eq. (3.27) ensures that no other modes will develop as the test particles evolve in time. If $0 < \frac{V_{i\perp}}{v_{Ti}} \ll 1$, the smallness of the $n > 0$ modes is guaranteed by the smallness of the $I_{n>0}$'s where $v_{\perp}/v_{Ti} \ll 1$, and by the exponential term in Eq. (4.12) where $v_{\perp}/v_{Ti} \gtrsim 1$. If $\frac{V_{i\perp}}{v_{Ti}} > 1$, $I_{n>0}$ enhance the significance of the $n > 0$ Fourier modes. Nevertheless, the convergence of the Fourier representation is still guaranteed by the fact that for a given argument, the I_n 's quickly decay with increasing n . Therefore, the rate at which the Fourier representation of a Maxwellian distribution converges is seen to be directly tied to the ratio $V_{i\perp}/v_{Ti}$.

Chapter summary

As previously stated, the qualities of a successful Fokker-Planck algorithm are general applicability, numerical efficiency, and preservation of the fundamental conservation properties of the FP operator. It is these qualities that have been explored by testing the proposed algorithm using the problems described in this chapter.

The δf approach, described in Chapter 3, can be implemented as a fully implicit scheme, allowing large, stable time steps. Within this chapter, some of the considerations and limitations of this scheme were discussed within the context of simple experiments. We have shown this scheme conserves number density to within the errors inherent in the representation and time advance, so long as the distribution function is well resolved and the velocity space domain is large enough to mitigate particle loss at the boundary.

The results in sections, Resistivity of an unmagnetized Lorentz plasma, and Thermalization of test particles, were compared to the finite volume approach in Ref. [8]. Using 441 degrees of freedom, the proposed algorithm obtained results comparable to those of Ref. [8] using 54,000 degrees of freedom. Convergence under h -type and p -type refinement was also shown, along with second order accuracy in time with $\theta = 0.5$ time discretization.

Ultimately, the parameters of the FEM, h and p , as well as the semi-implicit time stepping yields a robust method for obtaining accurate solutions to the δf equation.

In the section entitled, Tenuous beam of test particles, the dynamic process of a beam scattering off a background plasma until equilibrium is reached was explored. This was shown to occur within only a few collision times. The last section considered a simple problem that requires the use of the Fourier expansion, when the test distribution and field distribution have different perpendicular flows. The number of Fourier harmonics required for a solution, as well as how strongly they couple together, was shown to be related to the strength of the relative flow. However, even with perpendicular flows on the order of the background thermal speed, relatively few Fourier terms are needed in the expansion to obtain converged results.

All of the results reported in this chapter were obtained on a laptop utilizing a 1 GHz processor, and 4 GB of memory. Many of the calculations took less than a minute to compute. This code is distributable to multiple processors, but this feature was not necessary for the applications presented here because of the speed of the algorithm. The necessity of the multiprocessing feature is anticipated when considering adding spatial dimensions, and is demonstrated in the next chapter for computing the field terms.

In summary, my proposed scheme applied to the test particle operator is a powerful tool for efficiently obtaining accurate solutions to a number of relevant test problems and extends the range of problems FP codes are currently equipped to handle by solving for the full 3D velocity dependence.

CHAPTER 5

THE FIELD OPERATOR

The Chapman-Enskog-like (CEL) approach described in Chapter 3 introduces the field operator into the FP equation, and its velocity space moments into the fluid equations. This is challenging to code and difficult to make computationally efficient. The reason for the difficulty lies in the calculation of the TR potentials, which are integrals defined over the entire domain. While the finite element method is parallelizable over many computers by dividing the computational domain into blocks of cells owned by groups of processors, the TR potentials require calculating the relative velocity \mathbf{u} at every point in velocity space and sharing the numerical integration data among all the processors. Additionally, the TR potentials must be updated at every time step. Furthermore, a θ -centered implicit time advance requires the calculation of the TR potentials at every iteration of the GMRES solver. A major accomplishment of my thesis work involved an efficient implicit implementation of the field operator that is capable of using hundreds of processors.

This chapter will demonstrate numerical results, which have been obtained using the field operator through the CEL approach. In the first simulation, we calculate the conductivity of an unmagnetized plasma by applying an electric field, and evolving the electrons and ions until collisional friction balances the electric force. Complications arise, and the present solutions to these complications are discussed in detail. The second section of this chapter examines the thermalization of ion and electron distribution functions with different initial temperatures.

Spitzer conductivity

As a numerical experiment to test the accuracy and efficiency of our Fokker-Planck code including the field operator, we compute the conductivity of an unmagnetized plasma and compare with accepted values. To understand the dynamical features of this problem

consider the following thought experiment. Imagine a spatially homogeneous, fully ionized plasma in thermal equilibrium, i.e., the ion and electron distributions are Maxwellians with equal temperatures and the kinetic distortions are initially zero, $F_a = 0$. If a weak electric field, $\mathbf{E} \equiv E\hat{\mathbf{b}}$, is suddenly turned on, the electrons will accelerate in the $-\hat{\mathbf{b}}$ direction. Unlike the assumptions under the δf approach, which lead to the resistivity of a Lorentz plasma of immobile ions, presented in Chapter 4, here the ions are mobile and begin to accelerate in the direction of the electric field. The inertia of the ions prevent them from accelerating as quickly as the electrons, and the magnitude of the ion flow velocity is much smaller than that of the electron flow.

The current, \mathbf{J} , is primarily due to the flow of electrons. The total momentum is conserved during the acceleration due to \mathbf{E} , and the Coulomb collision operator also conserves total momentum despite collisions the particles experience with each other. Friction between particle species due to collisions slows the increase of current until a steady state is achieved. In addition, collisional heating takes place as the energy particles gain from the electric field is distributed through collisions within and between species. Heating of the plasma continues even after the semi-steady-state current is achieved. This ohmic heating is very important in the heating of fusion plasmas, such as tokamaks, where a toroidal current is induced in the plasma to provide this primary form of heating and the confining poloidal magnetic field. Ohmic heating is capable of increasing the temperature to about $2 \sim 3$ keV at which point the lower resistivity makes this heating process inefficient. However, this happens on a much longer timescale than we are interested in presently. For our test, it is the semi-steady state that we are interested in, and the dynamical evolution leading to it.

Analysis of the test particle operator gives us insight into the timescales of these processes. A reference collision frequency for particles streaming, with a velocity, \mathbf{v} , through

a background of particles is often defined as

$$v_0^{a/b} = \frac{n_b \Gamma_{ab}}{v^3}, \quad (5.1)$$

where Γ_{ab} is the coefficient of the Coulomb collision operator defined in Chapter 2. For this discussion we normalize other timescales by $\tau_{ee} = \left(v_0^{e/e}\right)^{-1}$. The test particle operator reveals the timescale for the ion-electron interaction, which slows the ions down, is on the order, $\mathcal{O}\left(\frac{m_i}{m_e} \tau_{ee}\right) = \mathcal{O}(1836 \times \tau_{ee})$, and the timescale for ion energy loss of ions to electrons is on the order, $\mathcal{O}\left(\left(\frac{m_i}{m_e}\right)^2 \tau_{ee}\right) = \mathcal{O}(3.37 \times 10^6 \times \tau_{ee})$. The ion slowing down time is characteristic of the frictional heating in this conductivity problem, and the energy loss time is characteristic of the ohmic heating, both of which are far longer than the timescales we are interested in when calculating the conductivity.

The conductivity, σ , of the plasma is defined by the relationship

$$\mathbf{J} = \sigma \mathbf{E}, \quad (5.2)$$

and can be calculated from the current and electric field. In an unmagnetized plasma,

$$\sigma = \alpha \frac{3\pi^{3/2} \epsilon_0^2 m_e v_{Te}^3}{q_e^2 \ln \Lambda_{ee}}, \quad (5.3)$$

where commonly accepted estimates of α are between 1.96 and 1.98 [25, 26, 27]. This experiment provides a good test to verify the field operator is implemented correctly and the CEL approach can preserve the conservation of momentum inherent in the collision operator, which was violated when the δf approach was used.

In the first attempts to calculate the dynamic evolution of σ , the code implemented a θ -centered implicit form of the test particle operator and an explicit form of the field operator

and CEL terms in the time advance:

$$\begin{aligned} \Delta F_a - \theta \Delta t \sum_b \left\{ \Delta C_{ab}^T - \frac{2f_a^M}{m_a n_a v_{Ta}} \left[\mathbf{z}_a \cdot \Delta \mathbf{R}_{ab}^T + v_{Ta}^{-1} \left(\frac{2}{3} z_a^2 - 1 \right) \Delta Q_{ab}^T \right] \right\} \\ = \Delta t \sum_b \left\{ C_{ab} - \frac{2f_a^M}{m_a n_a v_{Ta}} \left[\mathbf{z}_a \cdot \mathbf{R}_{ab} + v_{Ta}^{-1} \left(\frac{2}{3} z_a^2 - 1 \right) Q_{ab} \right] \right\}. \end{aligned} \quad (5.4)$$

This is different from the formulation in Eq. (3.5), which has field operator terms on the left side. Explicit terms are generally easier to implement, and are usually coded first. Initially, a uniform rectangular grid was used (see Fig. 5.2), giving the results shown in Fig. 5.1. The exact result, showing an increase in conductivity until the steady-state value of 1.97 is reached, is compared with our results for $p = 2, 3 \& 4$. Clearly the steady-state conductivity is not obtained and convergence with increasing p is quite slow. The results in Fig. 5.1 are well resolved in time. This was verified by repeating the simulation with smaller time steps and finding essentially the same result. After a lot of debugging and experimenting with different input parameters, it was apparent the code was performing as it should, and there must be a reasonable explanation for the decrease in the conductivity over time.

An important part of this problem is accurately computing the collisional friction, which controls the evolution of the flows, and hence the conductivity. For a physical interpretation, consider the following. When ions collide with electrons, it is like a collision between a car and a fly. The fly's momentum changes significantly but the car's momentum changes very little. The collisions that make the most significant changes to an ion's momentum are with electrons traveling close to the same velocity. This lengthens the interaction time of the collision, allowing the electron to have more of an influence on the ion. In terms of grid resolution, this demands resolving the electron distribution at lower energies where significant interaction with the ion distribution occurs. If this interaction is not accurately computed, the system will evolve as expected at first before the small inaccuracies in these long timescale interactions build up and spoil the long-term evolution (see Fig. 5.1).

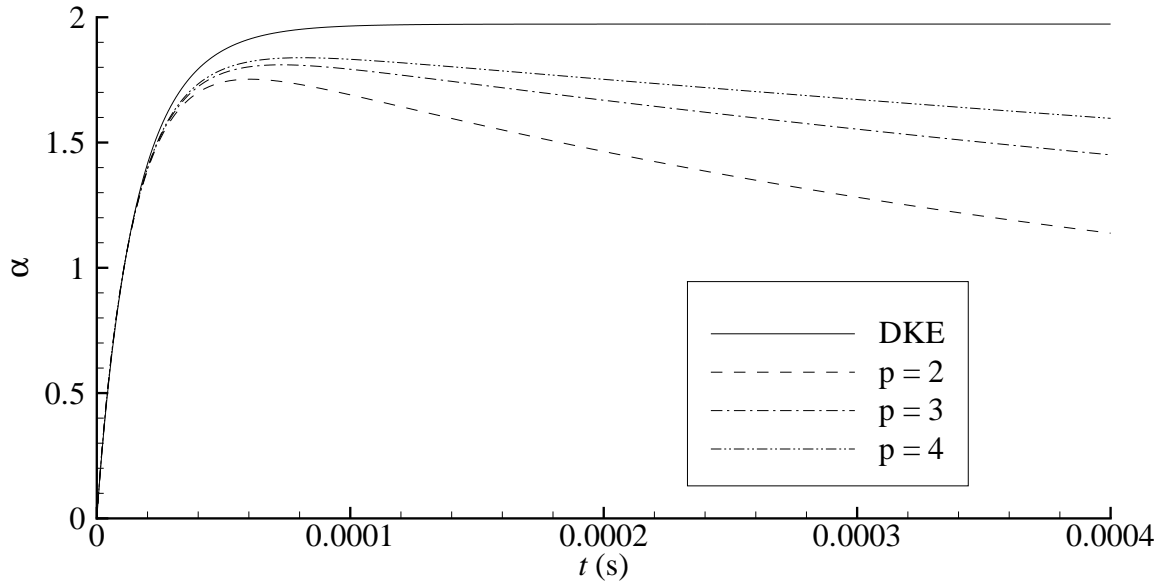


Fig. 5.1: Conductivity coefficient, α , of an unmagnetized plasma, using a 4×12 rectangular grid, and a few different polynomial degrees, over the domain $\Omega = [0, 4] \times [-6, 6]$. The curve labeled DKE was calculated using a different code, which solves the drift-kinetic equation (a gyro-averaged form of the kinetic equation).

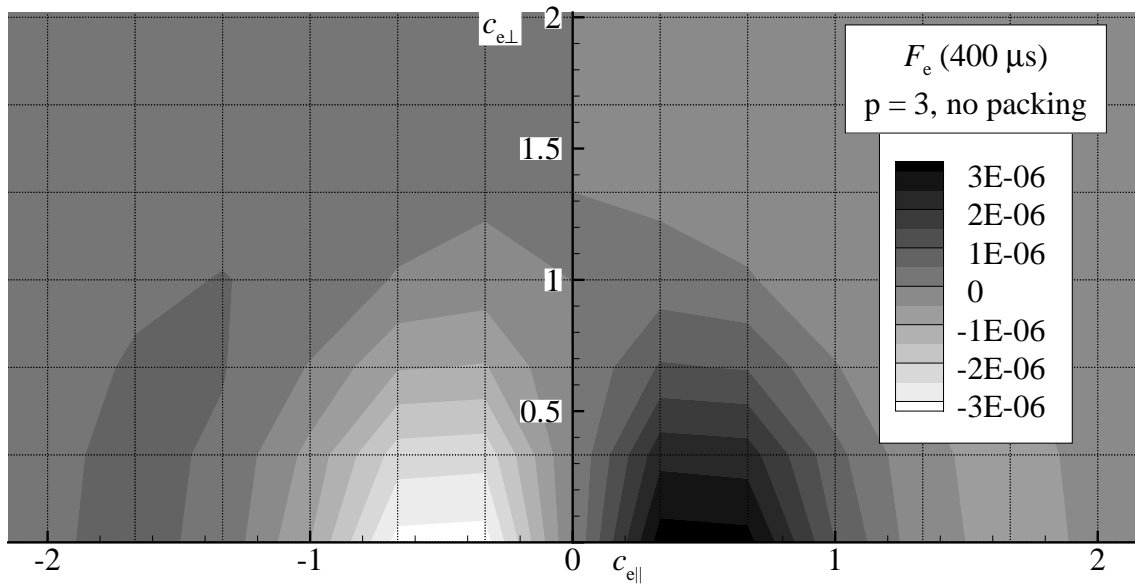


Fig. 5.2: Contour plot of the electron kinetic distortion in the conductivity problem, after $400 \mu s$, with no grid packing. $p = 3$, on a 4×12 grid. Note the lack of resolution near the origin where $|F_e|$ is large. Vertices of the grid are nodal points.

Thinking that the approximation of the kinetic distortion was poorly resolved, the polynomial degree of the underlying finite element representation was increased. However, under p -type refinement, convergence toward a well-behaved solution with a nearly constant conductivity was very slow. Examination of the kinetic distortion at the end of the simulations presented in Fig. 5.1 revealed they were not very well resolved in the region where the kinetic distortion had the greatest magnitude. Unfortunately, decreasing the uniform grid size and increasing the polynomial degree was computationally prohibitive due to the TR potential calculations, hence grid packing became a feature of the code worth exploring. Since the kinetic distortion is largest within a region of a couple thermal speeds of the origin, grid packing near the axes of this rectangular grid was turned on (see Fig. 5.4). Although this improved the results, (see Fig. 5.3), p -type refinement was still not converging quickly.

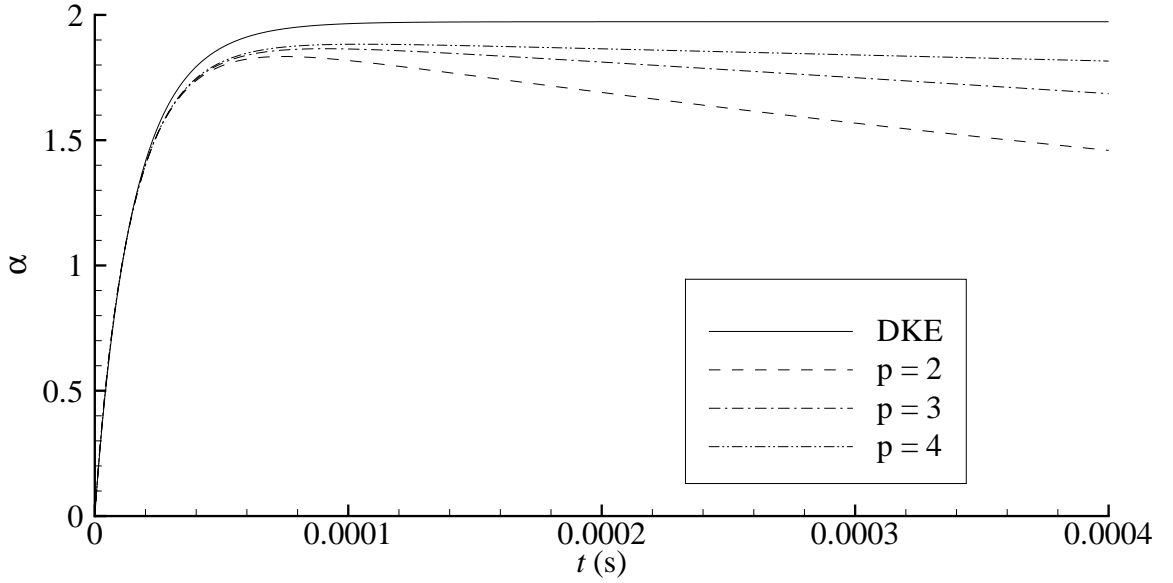


Fig. 5.3: Conductivity coefficient, α , of an unmagnetized plasma, using a 4×12 rectangular grid with packing near the $c_{a\perp} = 0$ and $c_{a\parallel} = 0$ axes, and a few different polynomial degrees, over the domain $\Omega = [0, 4] \times [-6, 6]$. The curve labeled DKE was calculated using a different code, which solves the drift-kinetic equation (a gyro-averaged form of the kinetic equation).

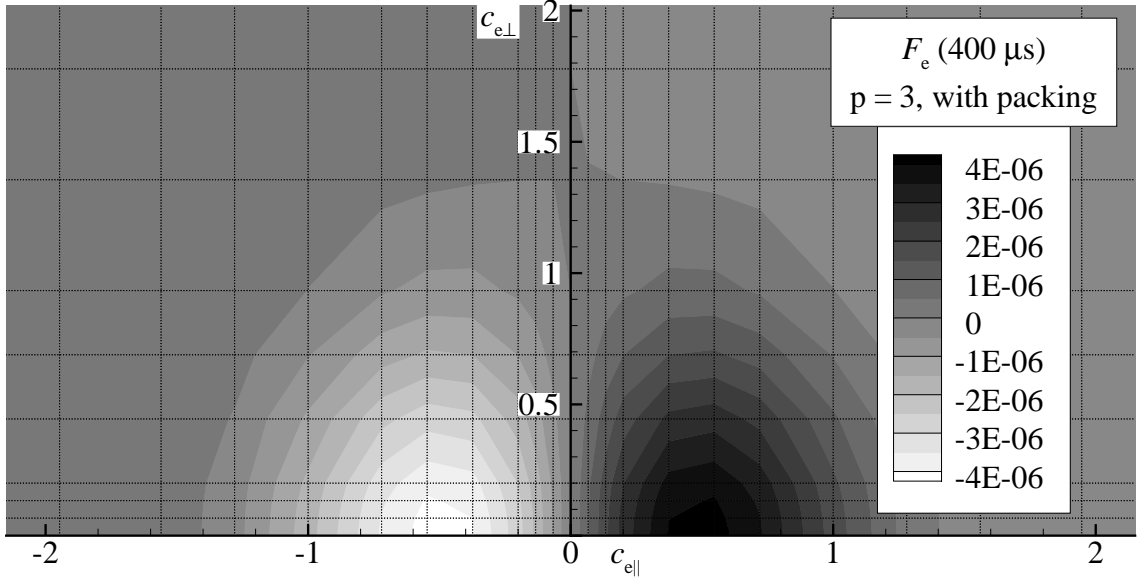


Fig. 5.4: Contour plot of the electron kinetic distortion in the conductivity problem, after $400 \mu s$, with grid packing near the axes. Here $p = 3$, on a 4×12 grid. Vertices of the grid are nodal points. Resolution near the origin was enhanced compared to that of Fig. 5.2.

As mentioned previously, momentum conservation in the conductivity problem heavily relies upon the accurate resolution of the ion-electron interaction in the field term, $C(f_i^M, F_e)$. The reason this field term is difficult to resolve is because the ion domain is roughly $\sqrt{\frac{m_e}{m_i}} \approx \frac{1}{43}$ times smaller than the electron domain. Fortunately, τ_{ee} is roughly $\frac{m_e}{m_i} \approx \frac{1}{1836}$ times the timescale of ion-electron collisions, thus packing within $\sqrt{\frac{m_e}{m_i}} v_{Te}$ of the origin of the electron velocity domain resolves the ion-electron interaction but does not compromise taking large stable time steps.

Grid packing near the axes of a rectangular grid is problematic for a couple of reasons. First, it wastefully packs cells in regions far from the origin where the kinetic distortion is extremely tenuous. Second, with an explicit advance of the field operator, the small cell size away from the origin limits the time step due to numerical stability considerations. For these reasons a semicircular grid with grid packing near the origin of velocity space is desirable.

Additionally, the θ -centered implicit advance, with $\theta > 0$ is desirable for taking large

time steps while maintaining numerical stability. The simultaneous advancement of the ions with the electrons meant an absolute timescale needed to be used rather than scaling time steps by the species collision time, which was done in the δf approach. The field operator inherently takes much longer to compute than the test particle operator, because calculating the TR potentials requires integrating over the whole domain. However, changing the centering of the time advance of the field operator was a nontrivial task. Doing so involves programming the Fokker-Planck code to recompute the TR potentials, collisional friction and collisional energy exchange using the current iterate at each iteration of the GMRES solver. It also meant changing the algorithm to solve for the ion and electron kinetic distortions simultaneously. Finally, in order to perform the simulation in a practical amount of time, the code needed to be run in parallel.

After several months of making the necessary changes, debugging the code, and writing several diagnostic routines to ensure everything was being calculated correctly, it was possible to compute the steady-state plasma conductivity and show convergence under p -type refinement (see Fig. 5.5) to the accepted steady-state result of $\alpha = 1.96$ in the $p = 4$ case. Figures 5.6 & 5.7 show contours of the electron kinetic distortion for the bulk of the electron velocity domain and in the packed region with $|\mathbf{c}_e| \leq 0.1$, respectively. Finally, Fig. 5.8 shows satisfactory momentum conservation using the semicircular grid with grid packing near the origin.

Trubnikov-Rosenbluth potentials

Figures 5.5 - 5.8 show when grid packing is used in a very small region about the origin, e.g., a radius of 0.1 or smaller, the correct steady-state condition is obtained. While this is strictly needed for the electron domain, the implementation applies this grid packing to the ions as well. Tracking down errors in the field terms that capture the ion-electron interaction is a very complicated venture since there are so many pieces used to do the

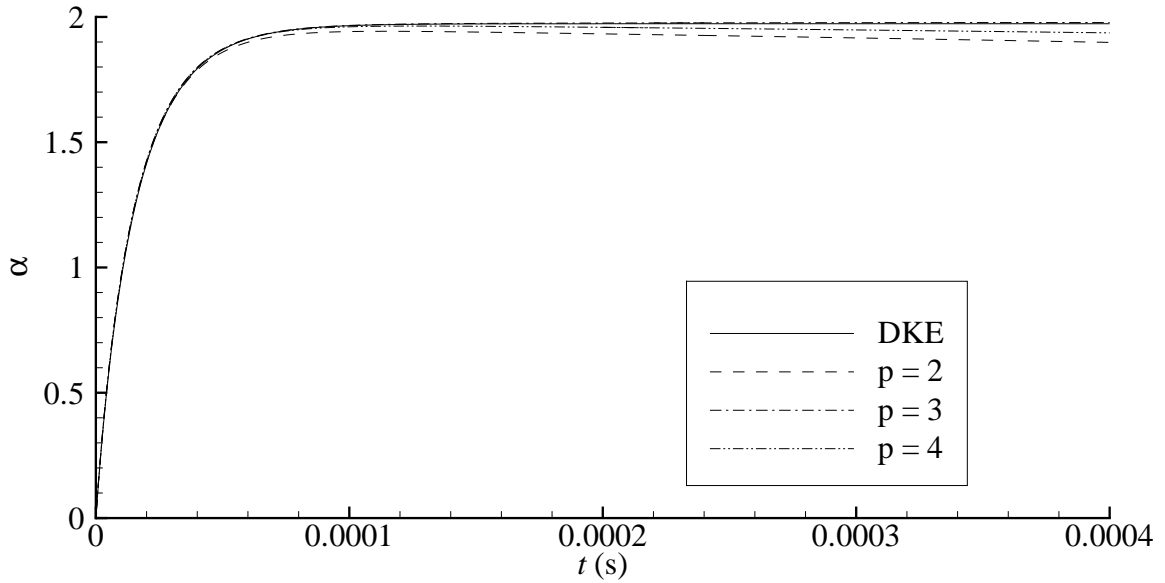


Fig. 5.5: Conductivity coefficient, α , of an unmagnetized plasma, using a 6×12 semicircular grid (using packing within 0.1 radius of origin $(c_{a\perp}, c_{a\parallel}) = (0,0)$), and a few different polynomial degrees, over a semicircular domain Ω with maximum speed of 6 thermal speeds. The curve labeled DKE was calculated using a different code, which solves the drift-kinetic equation.

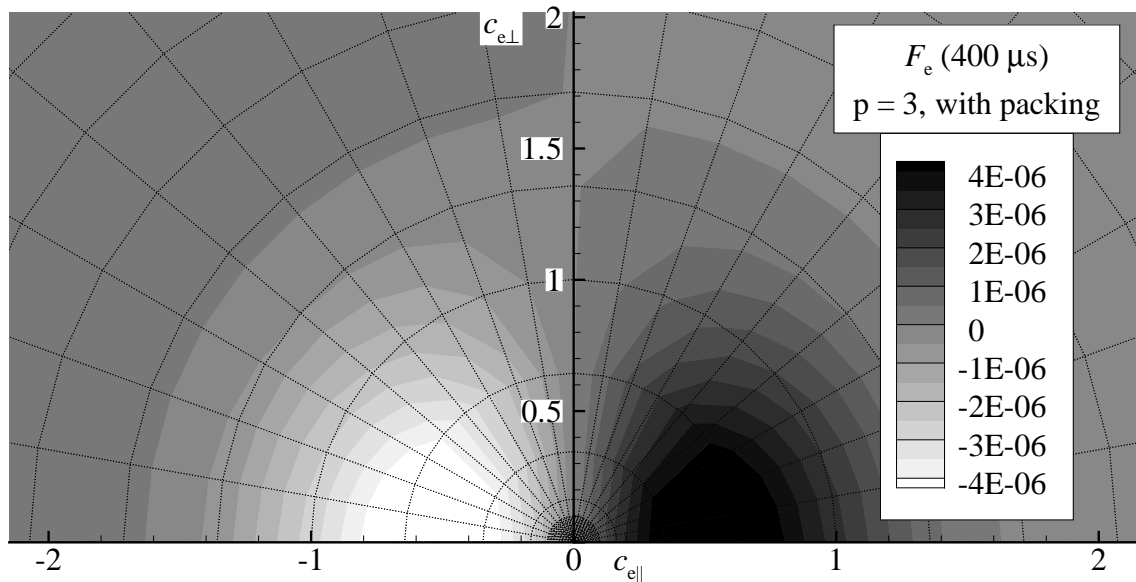


Fig. 5.6: Contour plot of the electron kinetic distortion in the conductivity problem, after $400 \mu s$. $p = 3$, on a 12×6 semicircular grid with 6×6 cells packed into 0.1 radius of the origin. The radius of the domain, Ω , is 6.

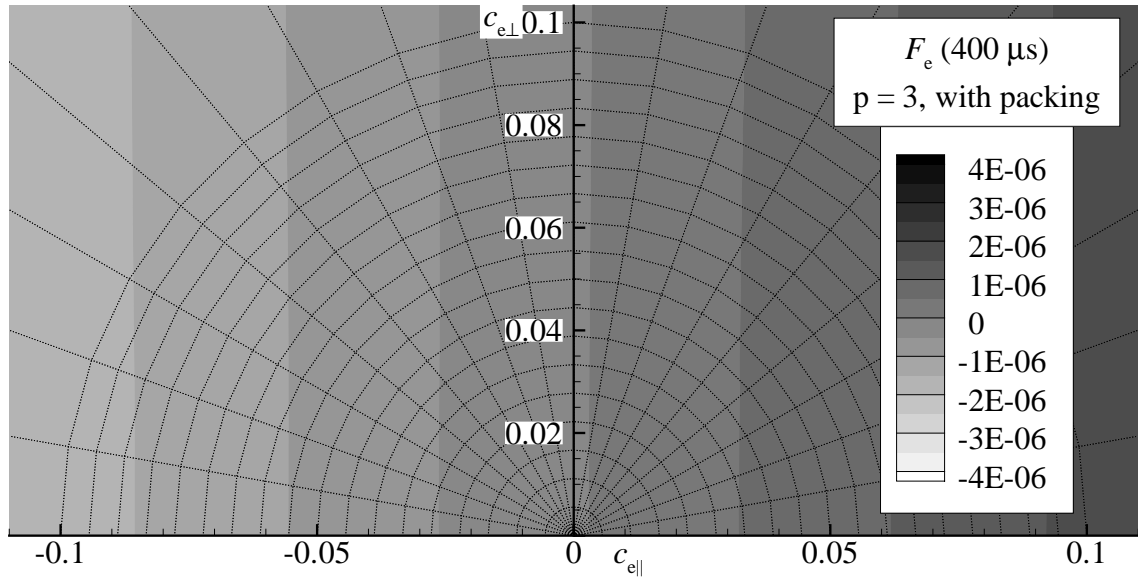


Fig. 5.7: Contour plot of the electron kinetic distortion in the conductivity problem, after $400\mu s$, showing grid packing near the origin. $p = 3$, on a 12×6 semicircular grid showing 6×6 cells packed into 0.1 radius of the origin. The radius of the domain, Ω , is 6.

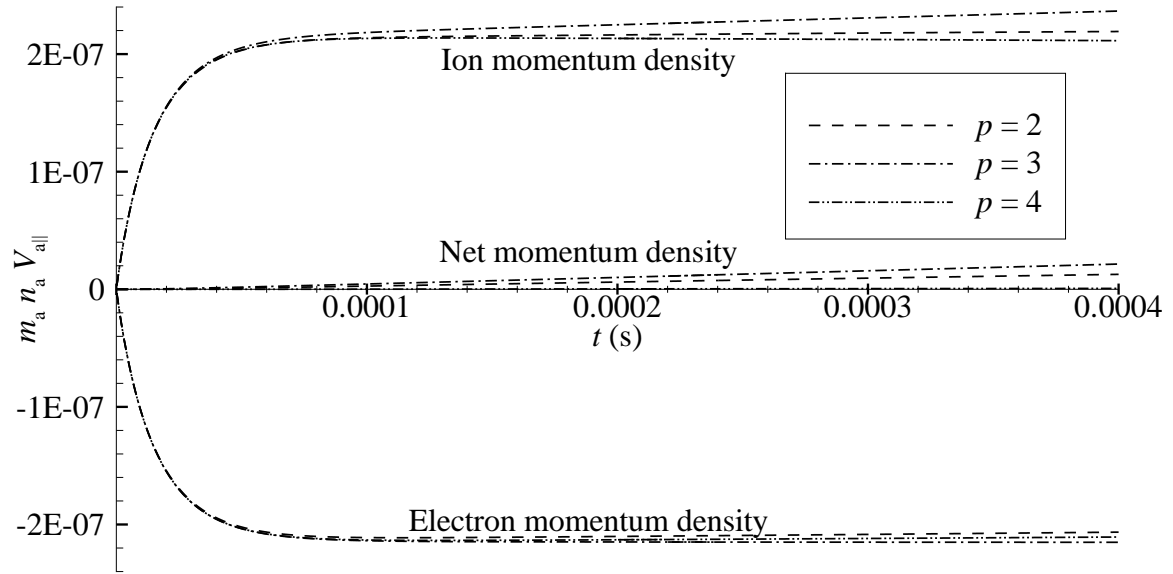


Fig. 5.8: Momentum conservation for the conduction problem.

calculation. Due to the importance of these issues, we now take up a careful discussion of calculating the TR potentials. There are several components, which make up the calculation

and several tests were done to verify the hypothesis that the unexpected evolution of the conductivity lies in the numerical errors of these potentials.

The algorithm is tested by calculating the TR potentials of Maxwellians, which have analytic forms for comparison. We use the following normalized potentials:

$$\bar{h}_b = \frac{1}{v_{Tb}^2} h_b = \int d\mathbf{c}'_b F_b(\mathbf{c}'_b) \bar{u}_b^{-1} \quad (5.5)$$

$$\nabla_{\mathbf{c}_b} \bar{h}_b = \frac{1}{v_{Tb}} \nabla_{\mathbf{v}} h_b = - \int d\mathbf{c}'_b F_b(\mathbf{c}'_b) \frac{1}{\bar{u}_b^3} \bar{\mathbf{u}}_b \quad (5.6)$$

$$\nabla_{\mathbf{c}_b} \bar{g}_b = \frac{1}{v_{Tb}^3} \nabla_{\mathbf{v}} g_b = \int d\mathbf{c}'_b F_b(\mathbf{c}'_b) \frac{1}{\bar{u}_b} \bar{\mathbf{u}}_b, \quad (5.7)$$

where

$$\bar{\mathbf{u}}_b = \frac{v_{Ta}}{v_{Tb}} \mathbf{c}_a - \mathbf{c}'_b. \quad (5.8)$$

Recall the γ integral is calculated using a fast Fourier transform and the convolution theorem:

$$\frac{1}{2\pi} \int_0^{2\pi} d\gamma' f(\gamma') g(\gamma - \gamma') \approx \sum_{n=-N}^N f_n g_n e^{in\gamma}. \quad (5.9)$$

For example, the TR potential, \bar{h}_b , is the convolution of F_b and

$$\bar{u}_b^{-1}(\gamma) = \left[\left(\frac{v_{Ta}}{v_{Tb}} c_{a\parallel} - c'_{b\parallel} \right)^2 + \left(\frac{v_{Ta}}{v_{Tb}} \right)^2 c_{a\perp}^2 + c_{b\perp}^2 - \frac{v_{Ta}}{v_{Tb}} c_{a\perp} c'_{b\perp} \cos(\gamma) \right]^{-1/2}. \quad (5.10)$$

\bar{h}_b can then be calculated by taking the inverse fast Fourier transform (FFT) of the product of $F_{a,n}$ with the Fourier coefficients of $\bar{u}_b^{-1}(\gamma)$. In principle these coefficients could be computed analytically resulting in a linear combination of complete elliptic integrals of the first and second kind. However, a general formulation in terms of the elliptic integrals has not yet been obtained for this purpose. Additionally, it is not clear that such a formulation would provide a faster or more accurate method for calculating these coefficients.

A singularity in the integrands of Eqs. (5.5 - 5.7), occurs where $\mathbf{v} = \mathbf{v}'$. This is avoided

by simply ignoring this term in the Gaussian quadrature sum over the 2D finite element domain. Recall that Gaussian quadrature is formulated to exactly integrate integrands, which are well-approximated by polynomials. Having a singular point in a cell spoils this assumption. Nevertheless this crude scheme is remarkably successful, as will now be shown.

In Chapter 2 the diffusion tensor, cf. Eq. (2.49), was calculated using a Maxwellian distribution in the test particle operator. By defining $\bar{h}_b^M = \int d\mathbf{c}'_b f_b^{M'} \bar{u}_b^{-1}$ and $\bar{g}_b^M = \int d\mathbf{c}'_b f_b^{M'} \bar{u}_b$, one can employ similar integration techniques to get the following results:

$$\bar{h}_b^M = \frac{n_b}{v_{Tb}^3} \frac{E(z_b)}{z_b}, \quad (5.11)$$

$$\nabla_{\mathbf{c}_b} \bar{h}_b^M = -2 \frac{n_b}{v_{Tb}^3} G(z_b) \frac{\mathbf{z}_b}{z_b}, \quad (5.12)$$

$$\bar{g}_b^M = -\frac{n_b}{v_{Tb}^3} \left\{ \frac{E(z_b)}{z_b} + z_b [E(z_b) - G(z_b)] \right\}, \quad (5.13)$$

$$\nabla_{\mathbf{c}_b} \bar{g}_b^M = -\frac{n_b}{v_{Tb}^3} [E(z_b) - G(z_b)] \frac{\mathbf{z}_b}{z_b}, \quad (5.14)$$

where $E(z_b)$ and $G(z_b)$ are the error function and Chandrasekhar function, respectively.

For reference, a contour plot of a nonshifted, electron Maxwellian distribution, for constant γ , is given in Fig. 5.9, and several of the TR potentials listed in Eqs. (5.11 - 5.14), are given in the Appendix.

Using the exact Maxwellian TR potentials, relative errors that arise from using the convolution theorem and numerical quadrature may be defined as

$$\eta(\mathbf{v}) \equiv \frac{|h(\mathbf{v}) - h_{\text{exact}}(\mathbf{v})|}{|h_{\text{exact}}(\mathbf{v})|}. \quad (5.15)$$

The absolute error is given by

$$\varepsilon(\mathbf{v}) \equiv |h(\mathbf{v}) - h_{\text{exact}}(\mathbf{v})|. \quad (5.16)$$

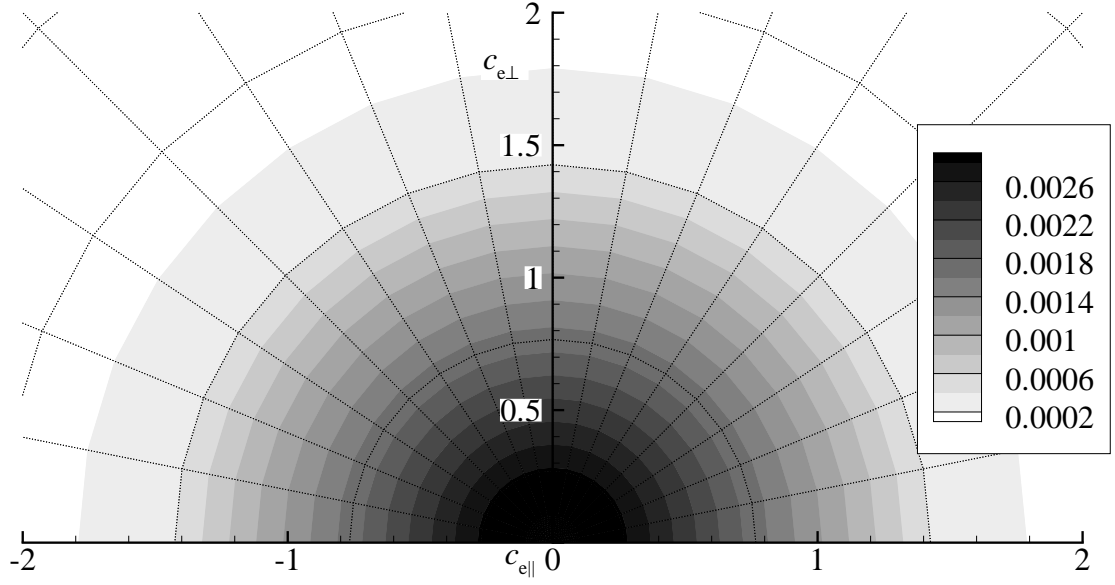


Fig. 5.9: Contour plot, for the $\gamma = 0$ plane, of the nonshifted Maxwellian used to compute the TR potentials in Figs. A.1 - A.11. Grid vertices are nodal points. The figures remaining in this section use $p = 2$ on a 15×8 grid with 7×8 cells packed in a 0.1 radius about the origin.

The reason for defining two errors is that while a relative error is more informative as to how large the error is, the absolute error is needed to quantify the error when the exact solution vanishes, as it does for the gradients in Eqs. (5.12 & 5.14). The relative errors of \bar{h}_e^M and \bar{g}_e^M are depicted as contour plots in Figs. 5.10 and 5.12. The absolute errors of the perpendicular components of $\nabla_{\mathbf{c}_e} \bar{h}_e^M$ and $\nabla_{\mathbf{c}_e} \bar{g}_e^M$ are depicted as contour plots in Figs. 5.11 and 5.13.

Figures 5.10 - 5.13 reveal the least amount of error occurs in the calculation of \bar{h}_e^M , in spite of the crude treatment of the singularity of the integrand where $\mathbf{v} = \mathbf{v}'$. Though difficult to make an exact comparison, $\nabla_{\mathbf{c}_e} \bar{g}_e^M$ has an error very close to that of \bar{h}_e^M . The relative error in \bar{g}_e^M is worse. $\nabla_{\mathbf{c}_e} \bar{h}_e^M$ seems to have the greatest error, which occurs near the origin, where important interactions between electrons and ions take place. This error is likely due to the fact that integrand's singularity is ignored, hence a more sophisticated numerical scheme may be necessary. This is a topic of future research. This error may

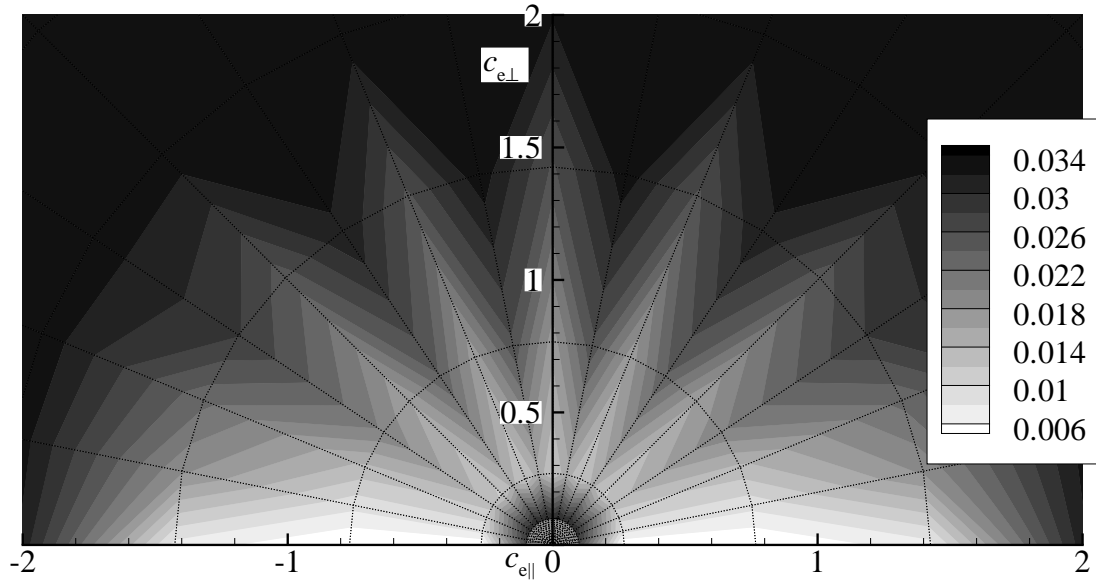


Fig. 5.10: Contour plot of relative error, η , of \bar{h}_e^M , defined in Eq. (5.15). This view shows detail near the origin.

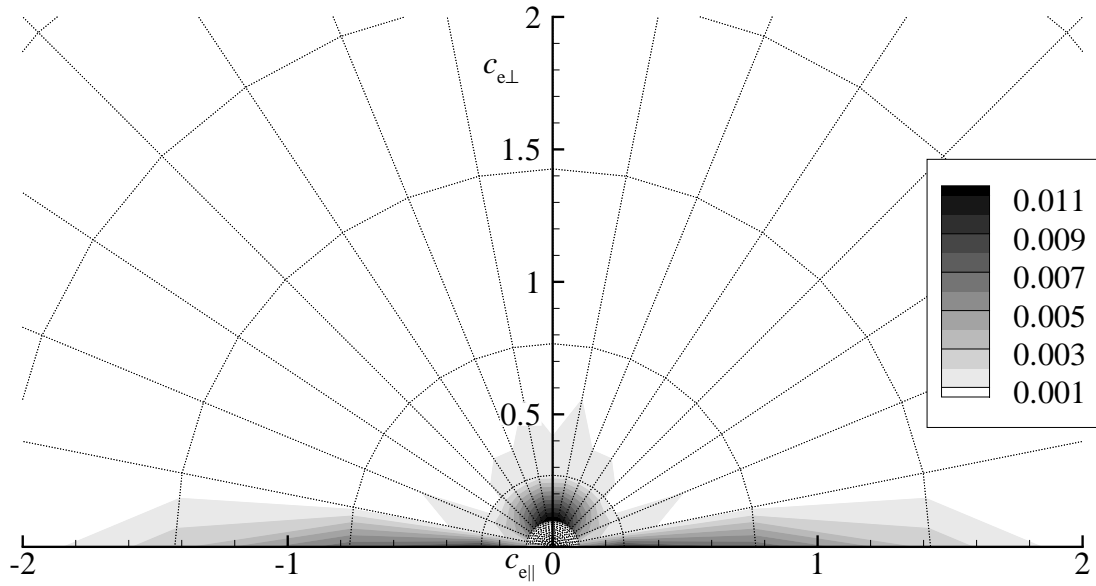


Fig. 5.11: Contour plot of absolute error, ϵ , of perpendicular component of $\nabla_{c_e} \bar{h}_e^M$, defined in Eq. (5.16). This view shows detail near the origin.

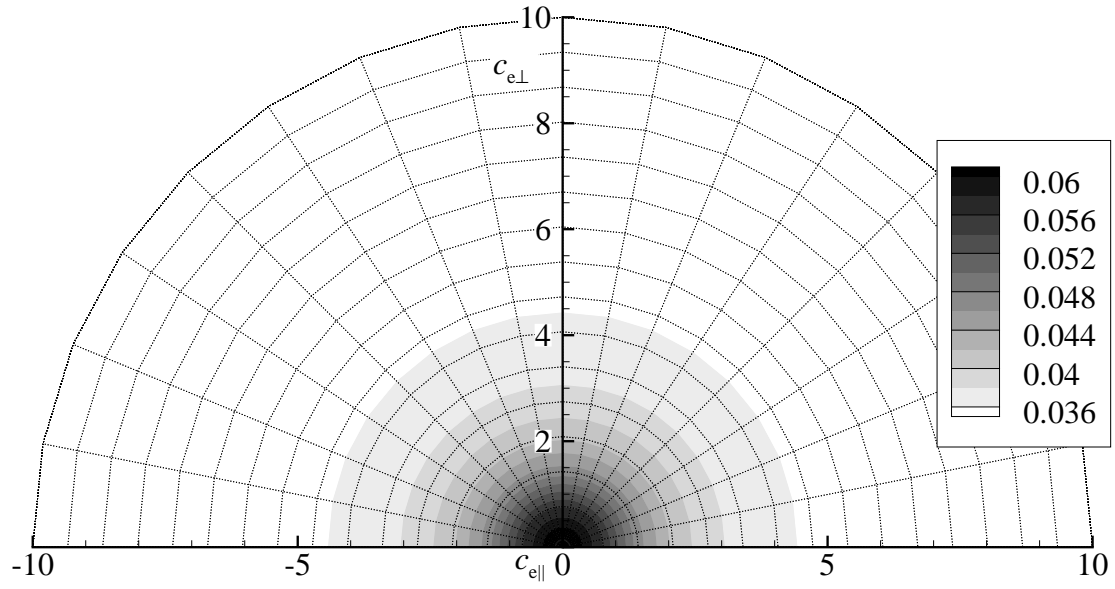


Fig. 5.12: Contour plot of relative error, η , of \bar{g}_e^M , defined in Eq. (5.15).

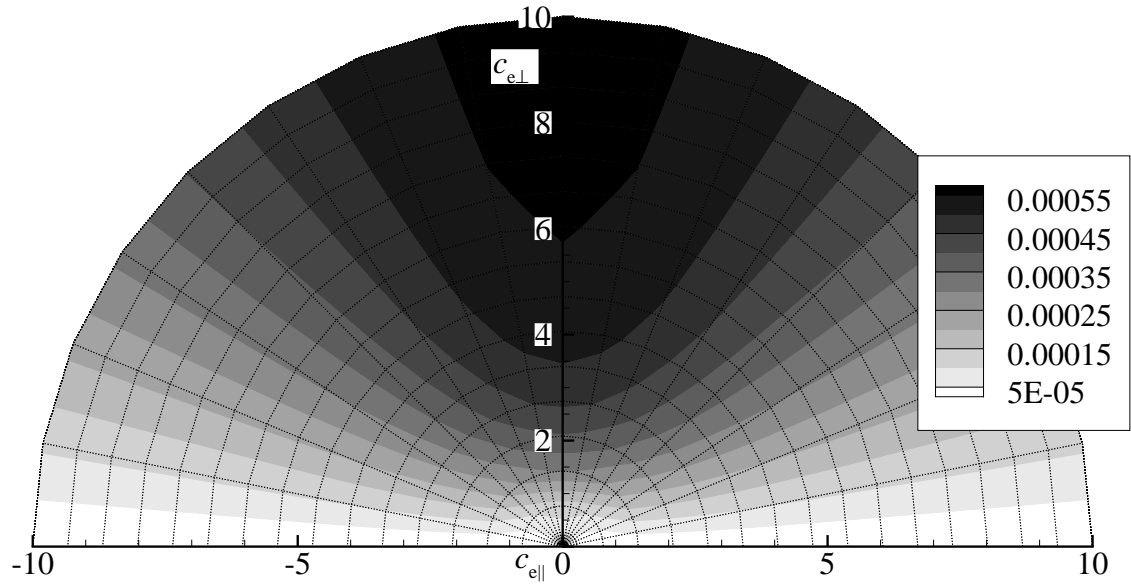


Fig. 5.13: Contour plot of absolute error, ε , of perpendicular component of $\nabla_{c_e} \bar{g}_e^M$, defined in Eq. (5.16).

be tied to errors observed in calculations of the plasma conductivity and thermalization, discussed in the next section.

While a possible contributor, it seems as though the singularity in the integrand is not entirely to blame for the errors seen in Figs. 5.10 - 5.13. If this were the case, then the least conspicuous integrand is in \bar{g}_e^M with no singularity. Yet it has an error, which is second only to $\nabla_{\mathbf{c}_e} \bar{h}_e^M$, with the highest order singularity. Another very important feature of these figures is the regions of high and low errors. These regions do not look entirely like random noise accumulated through numerical errors, such as the snowflake-like features in Fig. 5.10. Instead, the errors are concentrated in regions near the origin, far away from the origin, or in geometric patterns around the origin. This feature may be as important, or more important than the overall accuracy throughout the domain.

In the conductivity calculation, the large timescale behavior is dominated by the interaction between very slow electrons and ions. In order for momentum to be conserved, the test particle collisional friction, \mathbf{R}_{ei}^T , which is calculated using an exact form of the diffusion tensor, must be balanced by field collisional friction, \mathbf{R}_{ie}^F , using the numerically integrated TR potentials. By examining Figs. 5.10 - 5.13, we see that \bar{h}_e^M and $\nabla_{\mathbf{c}_e} \bar{g}_e^M$ not only have the best overall accuracy, but they are also more accurate in the important region of ion-electron interaction near the origin. The opposite is true of \bar{g}_e^M and $\nabla_{\mathbf{c}_e} \bar{h}_e^M$ where the regions of least accuracy lies near the origin. The consequences of this observation will be discussed in the next section where the weak form of the field operator is revisited in greater detail.

Weak form of the field operator

The sequence of partial integration, which leads to Eq. (3.33), namely,

$$\begin{aligned}
 I_{ab,j}^{F,n'} = & -2\Gamma_{ab}\frac{\Delta t}{2\pi}\int_{\Omega}d\mathbf{c}_a e^{-in'\gamma}f_a^M \times \\
 & \left\{ \frac{v_{Tb}}{v_{Ta}}\left(-\frac{1}{2}\frac{m_a}{m_b}\right)\overrightarrow{\alpha_j^{n'}}\cdot\nabla_{\mathbf{c}_b}\bar{h}_b \right. \\
 & - \left(\frac{v_{Tb}}{v_{Ta}}\right)^2\left[\overrightarrow{\alpha_j^{n'}}\cdot\mathbf{z}_a + 2\alpha_j(1-z_a^2)\right]\bar{h}_b \\
 & \left. + \left(\frac{v_{Tb}}{v_{Ta}}\right)^3\left[\overrightarrow{\alpha_j^{n'}}\cdot\mathbf{z}_a + 2\alpha_j(2-z_a^2)\right]\mathbf{z}_a\cdot\nabla_{\mathbf{c}_b}\bar{g}_b \right\}, \quad (5.17)
 \end{aligned}$$

where

$$\overrightarrow{\alpha_j^{n'}} \equiv e^{in'\gamma}\nabla_{\mathbf{c}_a}\left(\alpha_j e^{-in'\gamma}\right), \quad (5.18)$$

is not unique, and several other possible partial integrations were tested in the calculation of the plasma conductivity. The derivation presented in Chapter 3 was the one that gave the closest conductivity evolution when compared to accepted results. This subsection will discuss several approaches that seem like benign alternatives to the one presently used. These alternatives are shown to produce small errors, which accumulate over time. These are possibly due to domain truncation errors and/or errors in the calculation of the TR potentials (see the previous subsection). An approach that completely eliminates these errors is presently unknown, and will be the target of future research.

To begin, recall the result of multiplying the field operator by test functions and integrating over the velocity domain, cf. Eq. 3.31:

$$\begin{aligned}
 I_{ab,j}^{F,n'} = & -2\Gamma_{ab}\frac{\Delta t}{2\pi}\int_{\Omega}d\mathbf{c}_a\alpha_j e^{-in'\gamma}\left[\frac{1}{2}\frac{m_a}{m_b}\nabla_{\mathbf{v}}\cdot(f_a^M\nabla_{\mathbf{v}}h_b) + \frac{1}{v_{Ta}}f_a^M\mathbf{z}_a\cdot\nabla_{\mathbf{v}}h_b \right. \\
 & \left. + \frac{1}{v_{Ta}^2}f_a^Mh_b - \frac{1}{v_{Ta}^2}f_a^M\mathbf{z}_a\mathbf{z}_a:\nabla_{\mathbf{v}}\nabla_{\mathbf{v}}g_b\right]. \quad (5.19)
 \end{aligned}$$

In order to partially integrate the last term, the following is used

$$\begin{aligned}
& \alpha_j e^{-in'\gamma} f_a^M \mathbf{z}_a \mathbf{z}_a : \nabla_{\mathbf{v}} \nabla_{\mathbf{v}} g_b \\
&= \nabla_{\mathbf{v}} \cdot \left[\alpha_j e^{-in'\gamma} f_a^M \mathbf{z}_a (\mathbf{z}_a \cdot \nabla_{\mathbf{v}} g_b) \right] \\
& \quad - \frac{f_a^M}{v_{Ta}} e^{-in'\gamma} \left[\vec{\alpha}_j^{n'} \cdot \mathbf{z}_a + 2\alpha_j (2 - z_a^2) \right] (\mathbf{z}_a \cdot \nabla_{\mathbf{v}} g_b). \tag{5.20}
\end{aligned}$$

Note, any perfect divergence in $I_{ab,j}^{F,n'}$ may be converted to a surface integral at infinity. Distribution functions vanish at infinity by definition and hence, these surface integrals vanish. In Eq. (5.19), the first and last terms must be partially integrated, given reasons previously stated in Chapter 3. The second term, however, may be left alone, and doing so leads to

$$\begin{aligned}
I_{ab,j}^{F,n'} &= -2\Gamma_{ab} \frac{\Delta t}{2\pi} \int_{\Omega} d\mathbf{c}_a e^{-in'\gamma} f_a^M \times \\
& \quad \left\{ \frac{v_{Tb}}{v_{Ta}} \left(-\frac{1}{2} \frac{m_a}{m_b} \right) \vec{\alpha}_j^{n'} \cdot \nabla_{\mathbf{c}_b} \bar{h}_b \right. \\
& \quad + \frac{v_{Tb}}{v_{Ta}} \alpha_j \mathbf{z}_a \cdot \nabla_{\mathbf{c}_b} \bar{h}_b + \left(\frac{v_{Tb}}{v_{Ta}} \right)^2 \alpha_j \bar{h}_b \\
& \quad \left. + \left(\frac{v_{Tb}}{v_{Ta}} \right)^3 \left[\vec{\alpha}_j^{n'} \cdot \mathbf{z}_a + 2\alpha_j (2 - z_a^2) \right] \mathbf{z}_a \cdot \nabla_{\mathbf{c}_b} \bar{g}_b \right\}. \tag{5.21}
\end{aligned}$$

Alternatively, the diffusion tensor, in Eq. (5.20), can be written as

$$\begin{aligned}
& \alpha_j e^{-in'\gamma} f_a^M \mathbf{z}_a \mathbf{z}_a : \nabla_{\mathbf{c}_a} \nabla_{\mathbf{c}_b} \bar{g}_b \\
&= \alpha_j e^{-in'\gamma} f_a^M \mathbf{z}_a \cdot \nabla_{\mathbf{c}_a} \left(\mathbf{z}_a \cdot \nabla_{\mathbf{c}_b} \bar{g}_b - \frac{v_{Tb}}{v_{Ta}} \bar{g}_b \right) \\
&= \nabla_{\mathbf{c}_a} \cdot \left[\alpha_j e^{-in'\gamma} f_a^M \mathbf{z}_a \left(\mathbf{z}_a \cdot \nabla_{\mathbf{c}_b} \bar{g}_b - \frac{v_{Tb}}{v_{Ta}} \bar{g}_b \right) \right] \\
& \quad - e^{-in'\gamma} f_a^M \left[\vec{\alpha}_j^{n'} \cdot \mathbf{z}_a + \alpha_j (3 - 2z_a^2) \right] \left(\mathbf{z}_a \cdot \nabla_{\mathbf{c}_b} \bar{g}_b - \frac{v_{Tb}}{v_{Ta}} \bar{g}_b \right). \tag{5.22}
\end{aligned}$$

This approach yields the following weak form of the integral $I_{ab,j}^{F,n'}$:

$$\begin{aligned}
I_{ab,j}^{F,n'} = & -2\Gamma_{ab} \frac{\Delta t}{2\pi} \int d\mathbf{c}_a e^{-in'\gamma} f_a^M \times \\
& \left\{ \vec{\alpha}_j^{n'} \cdot \left[\frac{v_{Tb}}{v_{Ta}} \left(-\frac{1}{2} \frac{m_a}{m_b} \right) \nabla_{\mathbf{c}_b} \bar{h}_b \right] \right. \\
& + \alpha_j \frac{v_{Tb}}{v_{Ta}} \mathbf{z}_a \cdot \nabla_{\mathbf{c}_b} \bar{h}_b + \alpha_j \left(\frac{v_{Tb}}{v_{Ta}} \right)^2 \bar{h}_b \\
& \left. + \left[\vec{\alpha}_j^{n'} \cdot \mathbf{z}_a + \alpha_j (3 - 2z_a^2) \right] \left[\left(\frac{v_{Tb}}{v_{Ta}} \right)^3 \mathbf{z}_a \cdot \nabla_{\mathbf{c}_b} \bar{g}_b - \left(\frac{v_{Tb}}{v_{Ta}} \right)^4 \bar{g}_b \right] \right\}. \quad (5.23)
\end{aligned}$$

Partially integrating the second term, proportional to $\mathbf{z}_a \cdot \nabla_{\mathbf{c}_b} \bar{h}_b$, yields

$$\begin{aligned}
I_{ab,j}^{F,n'} = & -2\Gamma_{ab} \frac{\Delta t}{2\pi} \int d\mathbf{c}_a e^{-in'\gamma} f_a^M \times \\
& \left\{ \vec{\alpha}_j^{n'} \cdot \left[\frac{v_{Tb}}{v_{Ta}} \left(-\frac{1}{2} \frac{m_a}{m_b} \right) \nabla_{\mathbf{c}_b} \bar{h}_b \right] + \alpha_j \left(\frac{v_{Tb}}{v_{Ta}} \right)^2 \bar{h}_b \right. \\
& + \left[\vec{\alpha}_j^{n'} \cdot \mathbf{z}_a + \alpha_j (3 - 2z_a^2) \right] \left[\left(\frac{v_{Tb}}{v_{Ta}} \right)^3 \mathbf{z}_a \cdot \nabla_{\mathbf{c}_b} \bar{g}_b \right. \\
& \quad \left. \left. - \left(\frac{v_{Tb}}{v_{Ta}} \right)^4 \bar{g}_b - \left(\frac{v_{Tb}}{v_{Ta}} \right)^2 \bar{h}_b \right] \right\}. \quad (5.24)
\end{aligned}$$

Finally, all terms having products of α_j with gradients can be partially integrated, yielding a weak form with the maximum number of partial integrations:

$$\begin{aligned}
I_{ab,j}^{F,n'} = & -2\Gamma_{ab} \frac{\Delta t}{2\pi} \int d\mathbf{c}_a e^{-in'\gamma} f_a^M \times \\
& \left\{ \vec{\alpha}_j^{n'} \cdot \left[\frac{v_{Tb}}{v_{Ta}} \left(-\frac{1}{2} \frac{m_a}{m_b} \right) \nabla_{\mathbf{c}_b} \bar{h}_b \right] \right. \\
& - \left[\vec{\alpha}_j^{n'} \cdot \mathbf{z}_a + 2\alpha_j (1 - z_a^2) \right] \left(\frac{v_{Tb}}{v_{Ta}} \right)^2 \bar{h}_b + \vec{\alpha}_j^{n'} \cdot \mathbf{z}_a \left(\frac{v_{Tb}}{v_{Ta}} \right)^3 \mathbf{z}_a \cdot \nabla_{\mathbf{c}_b} \bar{g}_b \\
& \left. - 2 \left[\vec{\alpha}_j^{n'} \cdot \mathbf{z}_a (2 - z_a^2) + \alpha_j (2z_a^4 - 9z_a^2 + 6) \right] \left(\frac{v_{Tb}}{v_{Ta}} \right)^4 \bar{g}_b \right\}. \quad (5.25)
\end{aligned}$$

Gradients dotted into $\overrightarrow{\alpha_j^{n'}}$ are not further partially integrated because the C^0 continuity constraint on the representation limits the number of derivatives that can be taken.

In the limit that surface terms vanish, Eqs. (5.17, 5.21, 5.23, 5.24 & 5.25) represent equivalent analytic forms. However, the numerical errors that arise from evaluating each of them are considerably different. The reason for this may be that the TR potentials are computed using numerical quadrature and have different orders of singularities in the integrands. Domain truncation errors can also affect the weak form of an operator, when the surface term does not identically vanish. The conductivity problem, has been recalculated using these five different weak forms and the results are shown in Fig. 5.14. The simulations were also run with a reduced domain, with very similar results, suggesting that domain truncation errors are not responsible for the disparate results. This also suggests that ignoring surface terms is not problematic.

Figure 5.14 clearly demonstrates that, for the conduction problem, the most accurate weak form of the field operator is given in Eq. (5.17). When the different forms are compared, it can be seen the distinguishing feature of this weak form is that it maximizes the appearance of terms involving \bar{h}_b and $\nabla_{c_b}\bar{g}_b$, and minimizes the appearance of terms involving \bar{g}_b and $\nabla_{c_b}\bar{h}_b$. This is consistent with the contour plots of errors in the TR potentials found in the previous subsection, see Figs. A.1 - 5.13, which suggest \bar{h}_b and $\nabla_{c_b}\bar{g}_b$ have the least overall error, with regions of accuracy that are critical for capturing the correct long timescale ion-electron interactions. Since these TR potentials are computed using numerical quadrature, while the test particle operator is computed using an analytic form of the diffusion tensor, the collisional frictions, \mathbf{R}_{ei}^T and \mathbf{R}_{ie}^F do not exactly conserve momentum, cf. Eq. (2.38), contributing error, which simply accumulates over time resulting in the evolution seen in Fig. 5.14.

If momentum is not being conserved because of errors in calculating the TR potentials, then momentum conservation should get better by increasing the grid resolution and in-

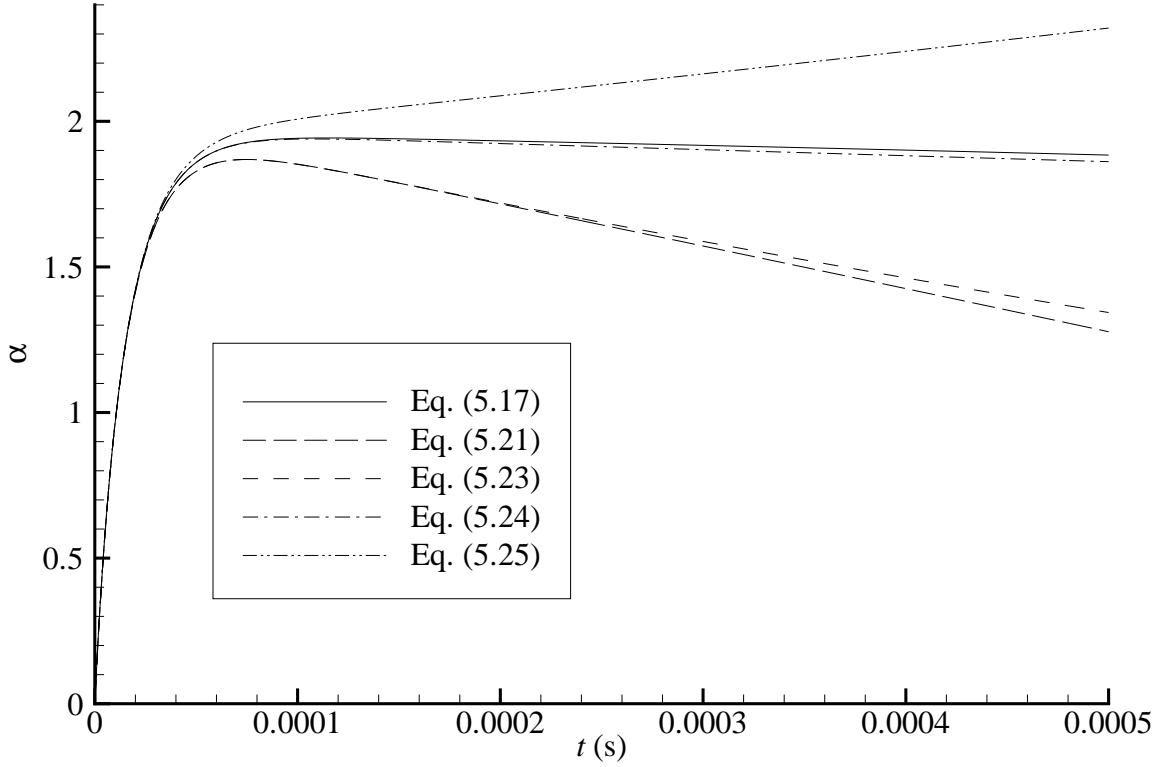


Fig. 5.14: Conductivity factor, α , defined in Eq. (5.3), calculated with different weak forms of the field operator, Eqs. (5.17, 5.21 - 5.25). Eq. 5.17 is closest to the correct evolution and approaches an equilibrium value close to 1.96.

creasing the polynomial degree, p , of the trial functions. Reaching a steady state in the conduction problem requires fidelity to the conservation laws. This is confirmed in the simulations, which undergo such refinement procedures (see Figs. 5.5 and 5.8).

Thermalization problem

In this section, we consider a problem where the ion and electron Maxwellian distributions start with different initial temperatures and come into thermal equilibrium. The initial kinetic distortions for both species are set to zero. Physically, the expected result is that the two species heat/cool until they reach thermal equilibrium at an average temperature. During the evolution, collision effects, which arise from the difference in temperatures, generate kinetic distortions during the process of equilibration. In this problem no colli-

sional friction exists because the distributions are not flowing relative to one another. The kinetic distortions play a minor role in mediating the collisional energy exchange, and after equilibrium is reached the kinetic distortions vanish.

The simplicity of this problem makes it another good test to see our algorithm has been programmed correctly. In addition, this problem tests the efficiency of the underlying representation to approximate a solution. Results showing the ion and electron temperatures, as well as the average temperature, which is constant when energy is conserved, are given in Fig. 5.15. Contour plots of the electron kinetic distortion at different times throughout thermalization are given in Fig. 5.16. This demonstrates the role of the kinetic distortion in the process. As discussed in the previous section, ion-electron energy exchange sets the longest collisional timescale, which is on the order, $\mathcal{O}\left(\left(\frac{m_i}{m_e}\right)^2 \tau_{ee}\right)$. A time step of $1\mu\text{s}$ gave a solution, which was numerically stable over the time to equilibration. Using this small of a time step required 40,000 steps to produce Fig. 5.15.

This calculation took approximately four hours to complete using 48 processors on Hopper, the world's 8th fastest supercomputer housed at Lawrence Berkeley National Laboratory. The temperatures can be seen to approach the correct average temperature, although over longer timescales imperfect energy conservation is seen. As in the conductivity problem, the long timescale evolution seems to suffer from an accumulation of numerical errors. Improving the results of this calculation is a goal of future research.

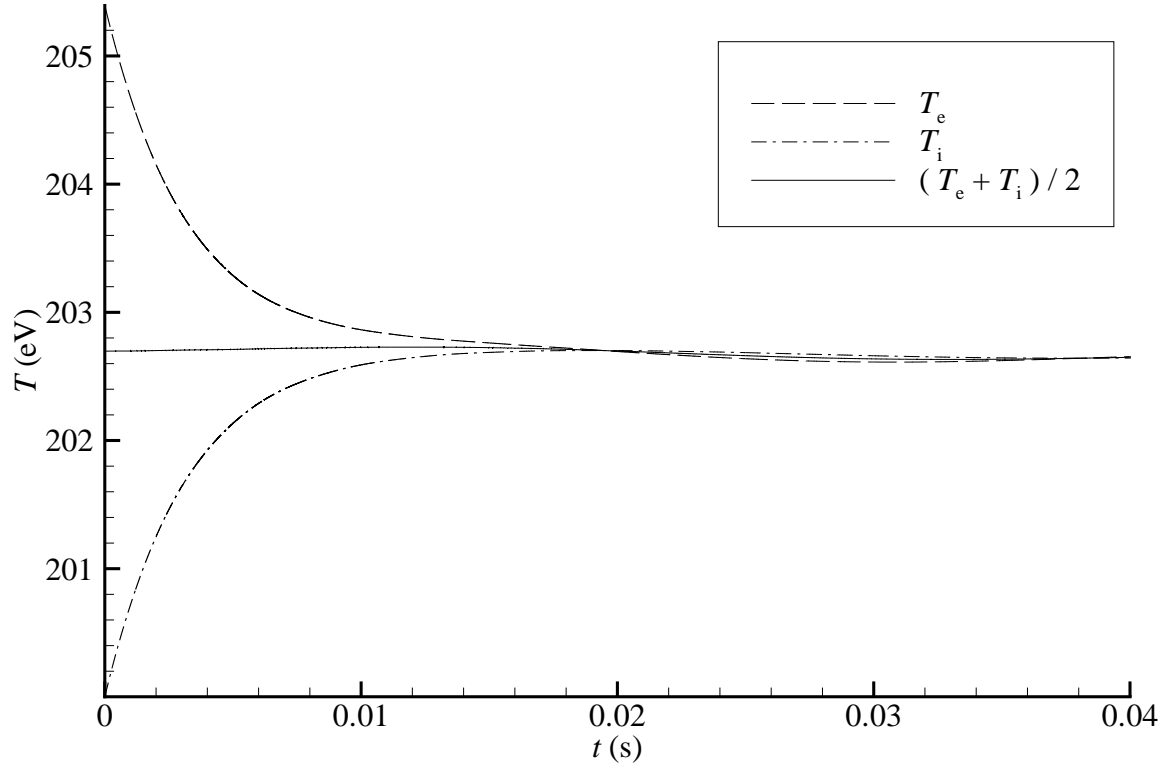


Fig. 5.15: Thermalization of electrons and ions with different initial temperatures. A 6×8 grid (3×8 cells packed into a radius of $3v_{Ta}$) over a semicircular domain with maximum speed of $10v_{Ta}$ was used. In this case, $p = 2$, and 40,000 steps of $\Delta t = 1 \mu s$ were taken using the implicit time discretization scheme. The initial ion temperature is 200eV, and the initial electron temperature is 205.4eV. We also see the total energy is very nearly conserved.

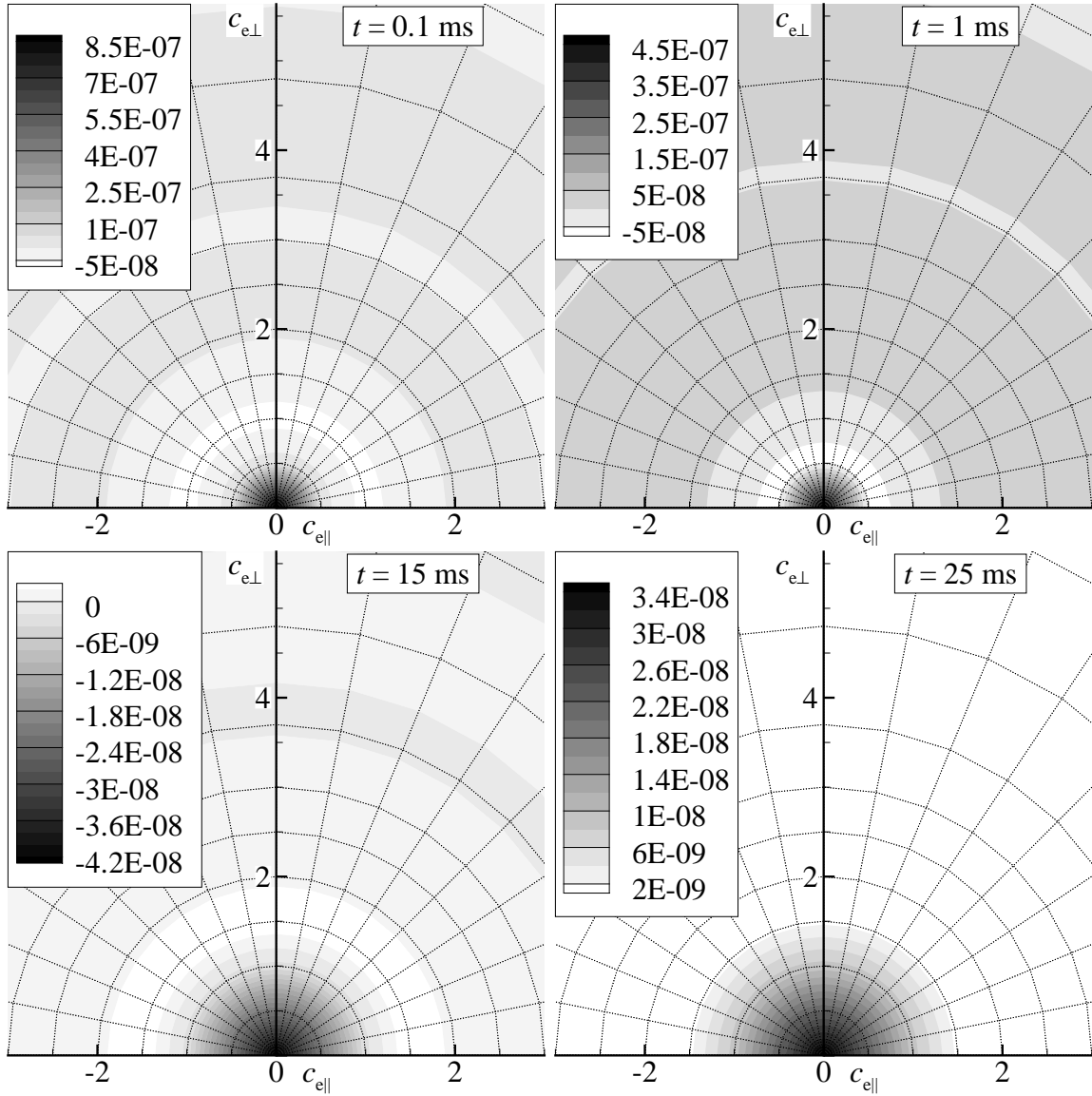


Fig. 5.16: Contours of electron kinetic distortion, F_e , at particular time steps of the thermalization of electrons and ions with different initial temperatures in Fig. 5.15. Note the kinetic distortion decays as the temperatures reach a common value.

CHAPTER 6

CONCLUSION AND FUTURE WORK

In this work we presented an approach to solving the plasma kinetic equation, which describes the evolution of spatially homogeneous, fully ionized plasmas. The NIMROD code, which implements a finite element/Fourier approximation to fluid quantities coupled to Maxwell's equations, was adapted to the purpose of providing numerically efficient solutions of the Fokker-Planck equation. Existing NIMROD machinery included data structures that hold the coefficients of the FEM/Fourier expansion, routines that interpolate and store quadrature point data used for numerical integration, and routines that implement the GMRES solver. This work required adaptation of this machinery for the purpose of solving the kinetic equation including creating new storage for the distribution functions, creating a weak formulation of the collision operators, and implementing this formulation into integration routines used by the GMRES solver for a θ -centered implicit time advance. In addition, I played a fundamental role in parallelizing the additional code, and creating a semicircular grid to pack cells near the origin of velocity space.

The first step taken toward adapting the NIMROD code to solve the kinetic equation was to employ the simplest form of the collision operator, the test particle operator. The δf approach, which yields a Fokker-Planck equation that uses the test particle operator, was described in Chapter 3. Then in Chapter 4, the δf approach was tested by solving several different problems with known solutions. The resistivity of a plasma with immobile ions was computed demonstrating the powerful convergence properties of p -type refinement with its exponential convergence. The resistivity was also shown to converge very quickly to the analytic value.

Next, the problem of a test particle distribution coming into thermal equilibrium with a hotter/cooler background was explored. This problem was chosen to correspond with the same problem in Ref. [8], which implemented a finite volume method. Comparison of

accuracy and degrees of freedom between the two different representations for distribution functions were made. Our algorithm was found to be much more efficient at solving the thermalization problem. This problem also provided us with insight as to how a truncated domain can be a source of error when representing a distribution function defined over the infinite domain of velocity space. When the domain was too small, heating and cooling of the test particle distribution allowed particles to escape/appear. The domain truncation error was found to be easily mitigated by increasing the domain to a reasonable size. This also provided an appropriate point to talk about the intrinsic density conservation property of the test particle operator. It was shown the density was conserved with the FEM/Fourier representation, provided the domain truncation errors were mitigated.

The next simulation discussed in Chapter 4 was the equilibration of a beam of test particles scattering off a flowing background plasma. This demonstrated the basic properties of the collision operator to produce diffusion and drag on the velocity distribution function. The next problem considered in Chapter 4 tested the efficiency of the Fourier representation in azimuthal (or gyro) angle. This section discussed a Maxwellian test particle distribution with a different perpendicular flow than the background. Collisions cause the test particle distribution to heat and accelerate until the flows match and thermal equilibrium is achieved. It was found that a relatively small number of Fourier coefficients were needed to effectively represent the solution. This was demonstrated from an analytical perspective and a numerical one.

Chapter 5 provided insight into two very important problems, plasma conductivity and thermalization of two Maxwellians with different initial temperatures. In order to conserve momentum and energy, the field operator was included and the CEL approach was adopted. The CEL kinetic equation involves both the test particle and field operators, as well as terms involving the collisional friction and collisional energy exchange. Because it is integro-differential, the field operator was more difficult to implement and computation-

ally expensive to use in simulations than the test particle operator. It requires the calculation of the TR potentials using the kinetic distortion. The TR potentials must be computed at each time step throughout the evolution. In addition, a θ -centered implicit time advance requires the calculation of the TR potentials at every iteration of the GMRES solver. Finally, the coupling of the ion and electron distribution functions through the field operator require a simultaneous advance of both distribution functions.

The field operator was first tested in a computation of plasma conductivity. The important difference between this problem and the conductivity calculation in Chapter 4 was the ions were mobile, the primary concern being to conserve momentum throughout the simulation. It was found a semicircular grid with packing near the origin of velocity space was necessary for numerical accuracy of the ion-electron collisional effects over long timescales. Using this grid convergence to the steady-state conductivity was obtained. The section on the conductivity problem also took a detailed look at how the numerical accuracy of the TR potentials may be responsible for errors in the conservation properties and hence secular errors in the conductivity. Different weak forms of the field operator were also considered and shown to have different long timescale accuracy. Again this is likely tied to the numerical accuracy of the TR potentials calculation.

The last simulation in Chapter 5 showed the equilibration of ion and electron distributions with different initial temperatures. Collisional effects between the two distribution functions, initially Maxwellian, drive kinetic distortions, which mediate the equilibration process, then decay as the two Maxwellians reach an average temperature. Although the basic features of this type of evolution were seen in the results, the long timescale errors seen in the conductivity problem were present.

Recall what Chang and Cooper [22] wrote about solving the FP equation, “The underlying objectives of any practical numerical scheme are the following: (1) large time and velocity steps, (2) accuracy and stability, and (3) preservation of any intrinsic properties im-

plied by the Fokker-Planck equation.” In this regard, the implementation of the test particle operator, was extremely successful in fulfilling the first two objectives. Using a θ -centered implicit time advance allowed for large time steps in the δf scheme. Furthermore, using relatively course grids in velocity space still gave accurate results. The intrinsic density conservation property of the test particle operator was well preserved as long as domain truncation errors were mitigated by using a suitably large domain. The intrinsic properties of the full Coulomb collision operator of momentum and energy conservation, cannot be satisfied with the test particle operator alone, and hence the need for including the field operator via the CEL approach. The conservation of momentum is critical for the conductivity problem. This requires grid packing near the origin of the electron velocity domain to prevent error accumulation over long timescales. The source of this error seems to be tied to the numerical accuracy of the TR potentials calculation.

Future work includes a long list of ways to improve the numerical accuracy and efficiency, and expanding the functionality of our algorithm as it is presently coded. The first item is to find a more accurate way of calculating the TR potentials. This will likely solve the long timescale conservation problems discussed in Chapter 5. Increasing accuracy may be to compute the collision term, $C(f_a^M, f_b^M)$, using an exact, analytic form. Another possibility is to find an analytic form for the Fourier coefficients of \mathbf{u} , or else compute the diffusion tensor, in the field operator, rather than the TR potentials. In terms of computational efficiency, the calculation of the TR potentials dominates simulations that include the field operator. Future research will improve the efficiency of this calculation by finding ways to precompute quantities, which are used repetitively in the time advance. This includes consolidation of calls to FFT routines, which could reduce the time to set up communication between processors.

There are several ways of expanding the functionality of the present Fokker-Planck algorithm. A fully nonlinear approach might eliminate the need of distinguishing between

test particles and the background field, eliminating the need for multiple collision operators. Future research might also include introducing spatial dimensions. A logical progression towards this goal would be to introduce one spatial dimension at a time. In tokamak simulations, the preferred spatial dimension would be a radial flux label, which is typically one of two spatial coordinates used in existing Fokker-Planck codes [28].

- [1] E.M. Epperlein, Implicit and conservative difference scheme for the Fokker-Planck equation, *J. Comput. Phys.* 112 (1994) 291–297.
- [2] L. Chacon, D.C. Barnes, D.A. Knoll, G. Miley, An implicit energy-conservative 2D Fokker-Planck algorithm: I. Difference scheme, *J. Comput. Phys.* 157 (2000) 618–653.
- [3] L. Chacon, D.C. Barnes, D.A. Knoll, G. Miley, An implicit energy-conservative 2D Fokker-Planck algorithm: II. Jacobian-free Newton-Krylov solver, *J. Comput. Phys.* 157 (2000) 654–682.
- [4] M. Lemou, Numerical algorithms for axisymmetric Fokker-Planck-Landau operators, *J. Comput. Phys.* 157 (2000) 762–786.
- [5] L. Pareschi, G. Russo, G. Toscani, Fast spectral methods for the Fokker-Planck-Landau collision operator, *J. Comput. Phys.* 165 (2000) 216–236.
- [6] X. Antoine, M. Lemou, Wavelet approximations of a collision operator in kinetic theory, *C. R. Acad. Sci. Paris, Ser. I* 337 (2003) 353–358.
- [7] I.K. Khabibrakhmanov, G.V. Khazanov, The spectral collocation method for the kinetic equation with the nonlinear two-dimensional coulomb collisional operator, *J. Comput. Phys.* 161 (2000) 558–575.
- [8] Z. Xiong, R.H. Cohen, T.D. Rognlien, X.Q. Xu, A high-order finite-volume algorithm for Fokker-Planck collisions in magnetized plasmas, *J. Comput. Phys.* 227 (2008) 7192–7205.
- [9] J. Crank, P. Nicolson, A practical method for numerical evaluation of solutions of partial differential equations of the heat conduction type, *Math. Proc. Cambridge Philos. Soc.* 43 (1947) 50–67.
- [10] C.R. Sovinec, A.H. Glasser, T.A. Gianakon, D.C. Barnes, R.A. Nebel, S.E. Kruger, D.D. Schnack, S.J. Plimpton, A. Tarditi, M.S. Chu, Nonlinear magnetohydrodynamics simulation using high-order finite elements, *J. Comput. Phys.* 195 (2004) 355–386.
- [11] W.R. Martin, C.E. Yehnert, L. Lorence, J.J. Duderstadt, Phase-space finite element methods applied to the first-order form of the transport equation, *Ann. Nucl. Energy* 8 (1981) 633–646. *Finite Element Methods in Radiation Physics*.
- [12] D.A. McQuarrie, *Statistical Mechanics*, University Science Books, 2000.
- [13] M.N. Rosenbluth, W.M. MacDonald, D.L. Judd, Fokker-Planck equation for an inverse-square force, *Phys. Rev.* 107 (1957) 1–6.
- [14] B.A. Trubnikov, Particle interactions in a fully ionized plasma, *Rev. Plasma Phys.* 1 (1965) 105–204.
- [15] L.D. Landau, *J. Exptl. Theoret. Phys. USSR* 7 (1937) 203.
- [16] S. Chandrasekhar, Stochastic problems in physics and astronomy, *Rev. Mod. Phys.* 15 (1943) 1–89.
- [17] Z. Chang, J.D. Callen, Unified fluid/kinetic description of plasma microinstabilities. Part I: Basic equations in a sheared slab geometry, *Phys. Fluids B* 4 (1992) 1167–1181.

- [18] R.J. Kingham, A.R. Bell, An implicit Vlasov-Fokker-Planck code to model non-local electron transport in 2-D with magnetic fields, *J. Comput. Phys.* 194 (2004) 1–34.
- [19] G.E. Karniadakis, S.J. Sherwin, *Spectral/hp Element Methods for CFD*, Oxford University Press, 1999.
- [20] Y. Saad, *Iterative Methods for Sparse Linear Systems*, Society for Industrial and Applied Mathematics, 2003.
- [21] M. Abramowitz, I.A. Stegun, *Handbook of Mathematical Functions*, Dover Publications, Inc., New York, 1972.
- [22] J.S. Chang, G. Cooper, A practical difference scheme for Fokker-Planck equations, *J. Comput. Phys.* 6 (1970) 1–16.
- [23] L. Spitzer, *Physics of Fully Ionized Gases*, John Wiley and Sons, Inc., New York, 1956.
- [24] R. Landshoff, Transport phenomena in a completely ionized gas in presence of a magnetic field, *Phys. Rev.* 76 (1949) 904–909.
- [25] L. Spitzer, R. Härm, Transport phenomena in a completely ionized gas, *Phys. Rev.* 89 (1953) 977–981.
- [26] S.I. Braginskii, Transport processes in a plasma, *Rev. Plasma Phys.* 1 (1965) 205–311.
- [27] R.D. Hazeltine, J.D. Meiss, *Plasma Confinement*, Dover Publications, Inc., 2003.
- [28] R.W. Harvey, M.G. McCoy, The CQL3D Fokker-Planck code, General Atomics report GA-A20978 (1992).

APPENDIX

MAXWELLIAN TRUBNIKOV-ROSENBLUTH POTENTIALS

In Chapter 2 the diffusion tensor, cf. Eq. (2.49), was calculated using a Maxwellian distribution in the test particle operator. By defining $\bar{h}_b^M = \int d\mathbf{c}'_b f_b^{M'} \bar{u}_b^{-1}$ and $\bar{g}_b^M = \int d\mathbf{c}'_b f_b^{M'} \bar{u}_b$, one can employ similar integration techniques to get the following results:

$$\bar{h}_b^M = \frac{n_b}{v_{Tb}^3} \frac{E(z_b)}{z_b}, \quad (\text{A.1})$$

$$\nabla_{\mathbf{c}_b} \bar{h}_b^M = -2 \frac{n_b}{v_{Tb}^3} G(z_b) \frac{\mathbf{z}_b}{z_b}, \quad (\text{A.2})$$

$$\bar{g}_b^M = -\frac{n_b}{v_{Tb}^3} \left\{ \frac{E(z_b)}{z_b} + z_b [E(z_b) - G(z_b)] \right\}, \quad (\text{A.3})$$

$$\nabla_{\mathbf{c}_b} \bar{g}_b^M = -\frac{n_b}{v_{Tb}^3} [E(z_b) - G(z_b)] \frac{\mathbf{z}_b}{z_b}, \quad (\text{A.4})$$

where $E(z_b)$ and $G(z_b)$ are the error function and Chandrasekhar function, respectively.

Contour plots, for the $\gamma = 0$ plane, are given in this appendix for several of the TR potentials listed in Eqs. (A.1 - A.4). For comparison, contour plots of both the exact potentials, and potentials calculated using my algorithm are shown. The contour plots of the $\hat{\gamma}$ component of the gradients of \bar{h}_e^M and \bar{g}_e^M have been omitted from these figures since they are identically zero. The contour levels for each potential are the same and are set by the exact solutions,

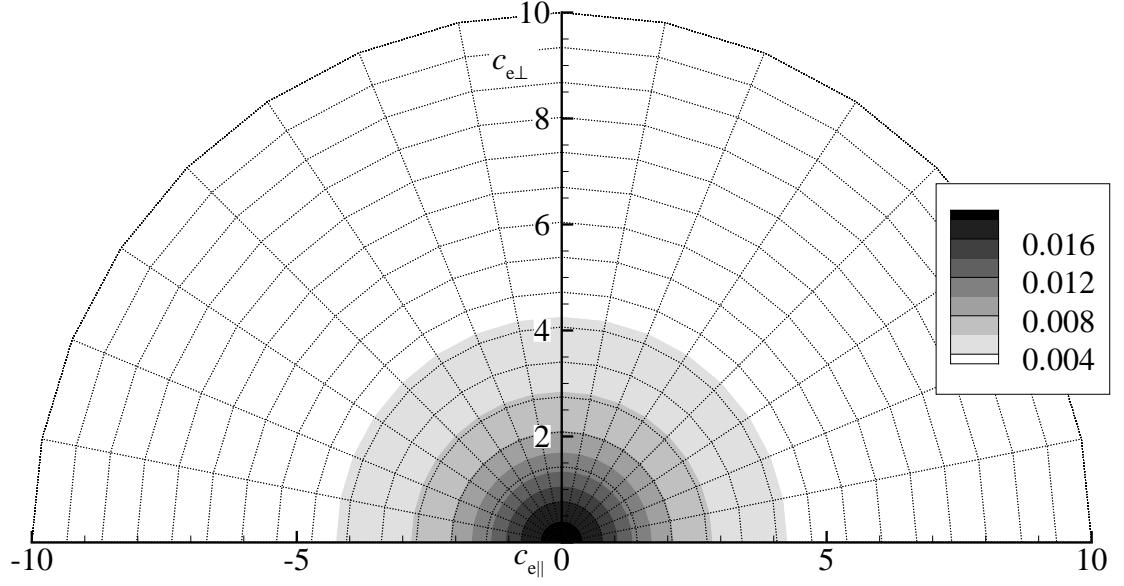


Fig. A.1: Contour plot of \bar{h}_e^M , defined in Eq. (5.11).

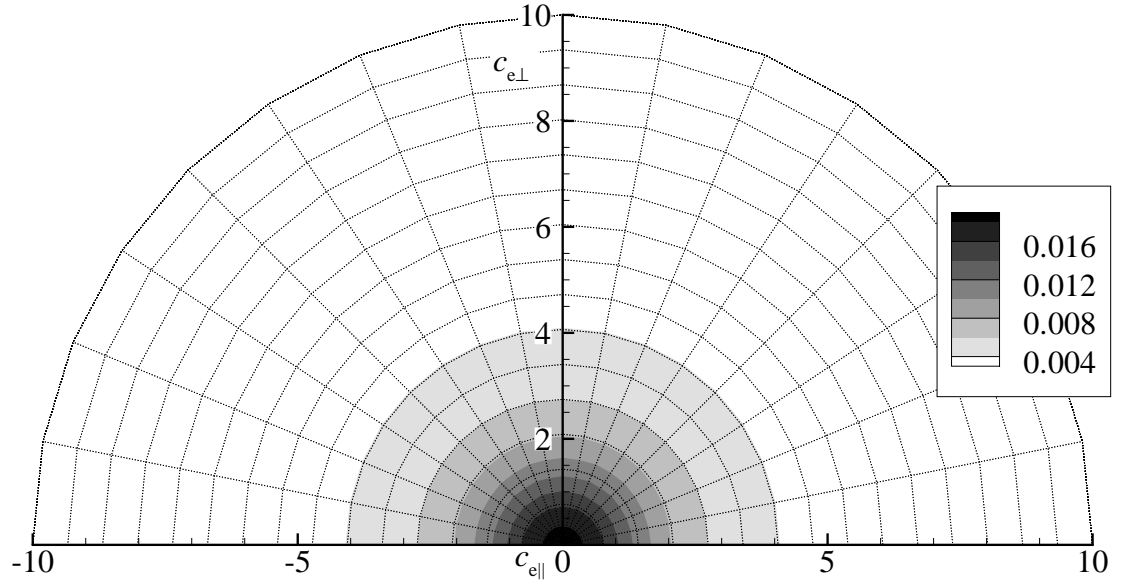


Fig. A.2: Contour plot of \bar{h}_e^M , calculated by our Fokker-Planck code.

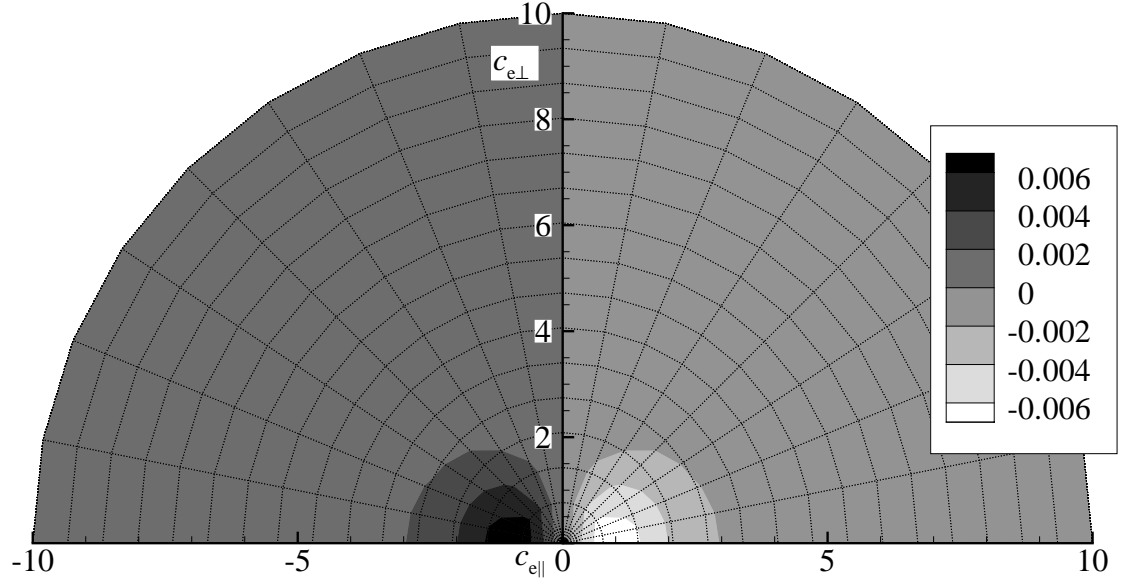


Fig. A.3: Contour plot of parallel component of $\nabla_{\mathbf{c}_e} \bar{h}_e^M$, defined in Eq. (5.12).

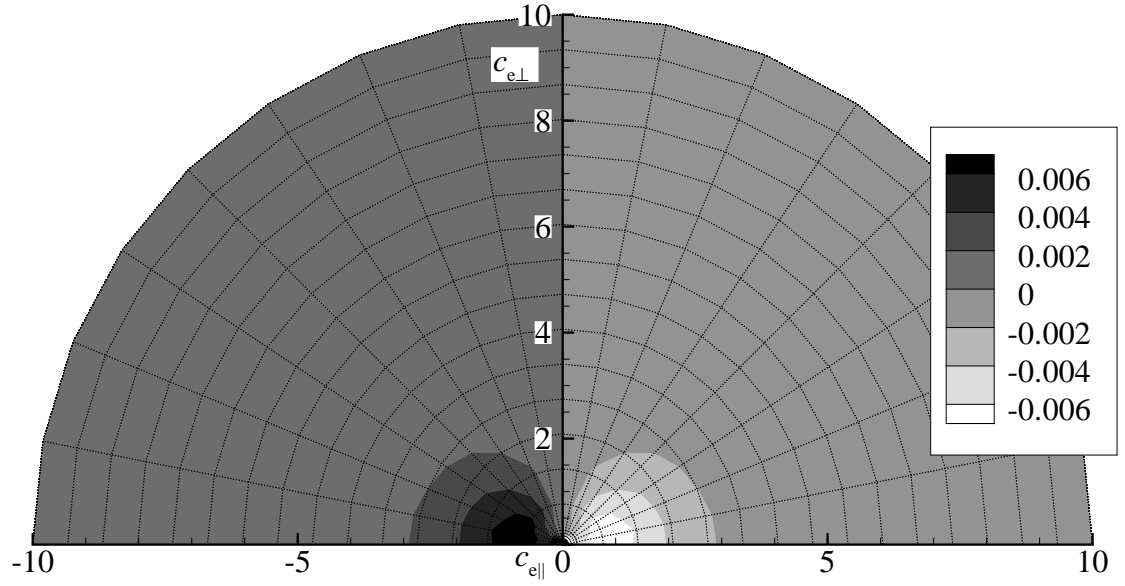


Fig. A.4: Contour plot of parallel component of $\nabla_{\mathbf{c}_e} \bar{h}_e^M$, calculated by our Fokker-Planck code.

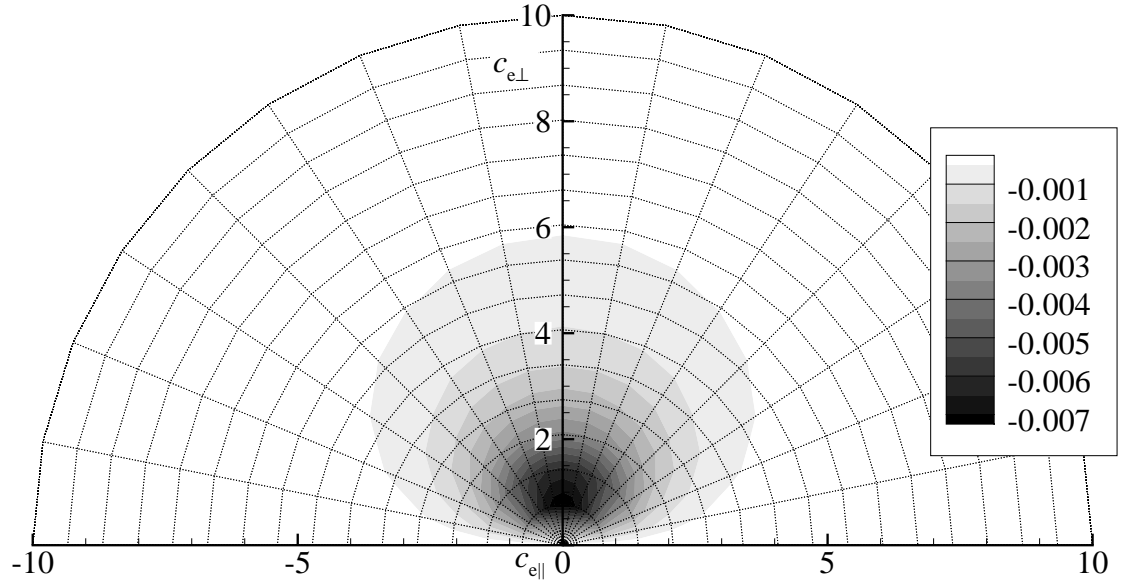


Fig. A.5: Contour plot of perpendicular component of $\nabla_{\mathbf{c}_e} \bar{h}_e^M$, defined in Eq. (5.12).

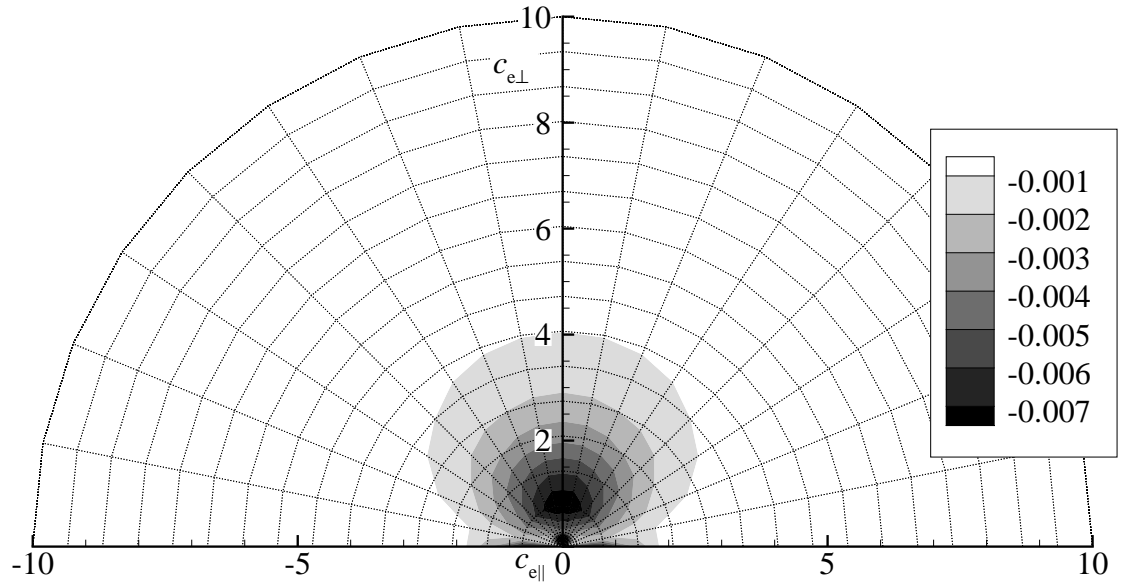


Fig. A.6: Contour plot of perpendicular component of $\nabla_{\mathbf{c}_e} \bar{h}_e^M$, calculated by our Fokker-Planck code.

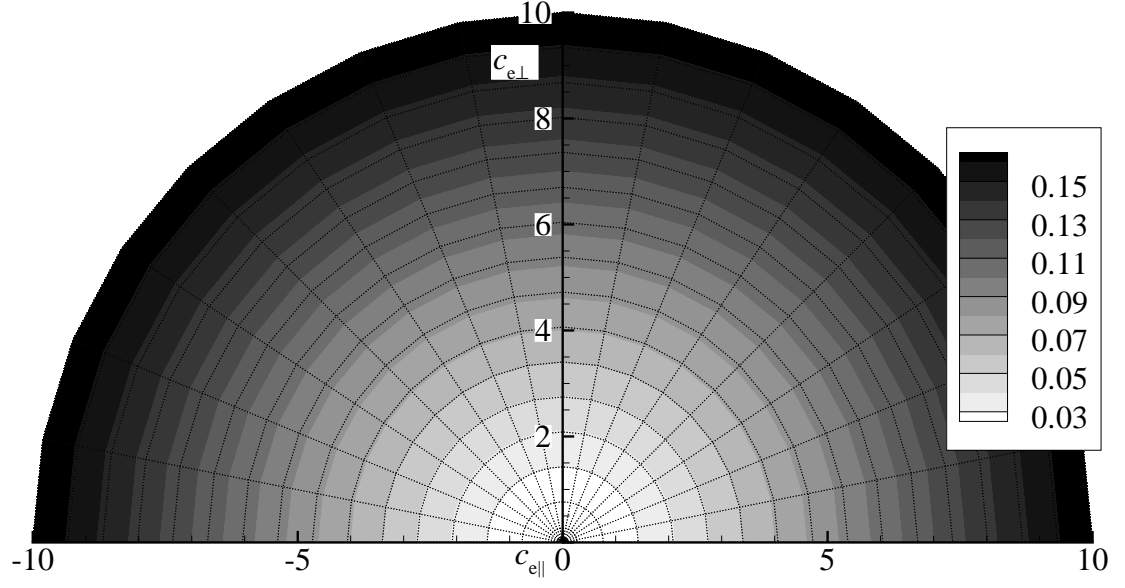


Fig. A.7: Contour plot of \bar{g}_e^M , defined in Eq. (5.13).

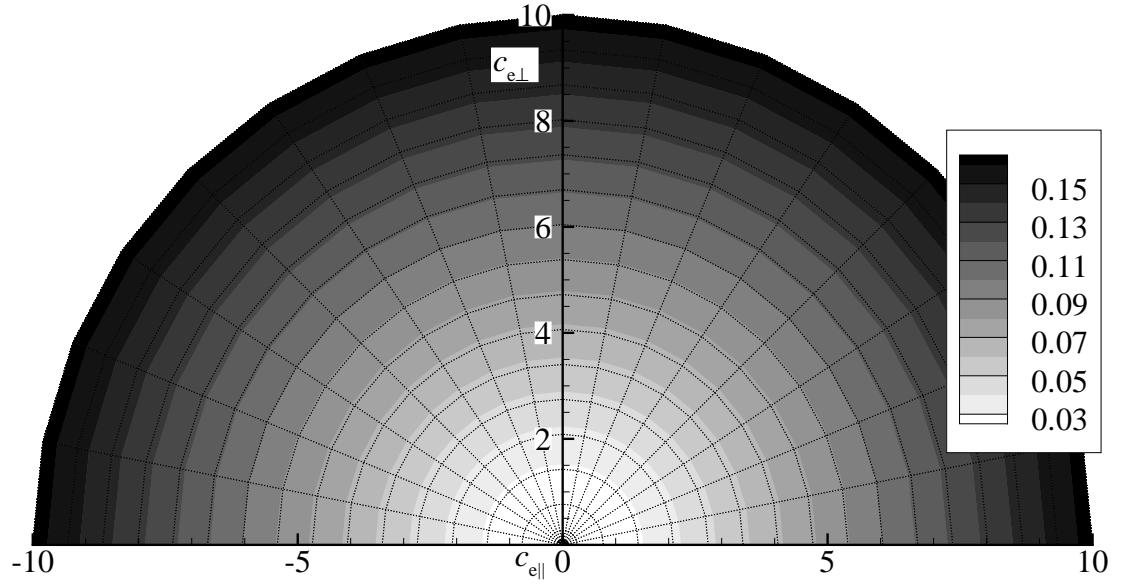


Fig. A.8: Contour plot of \bar{g}_e^M , calculated by our Fokker-Planck code.

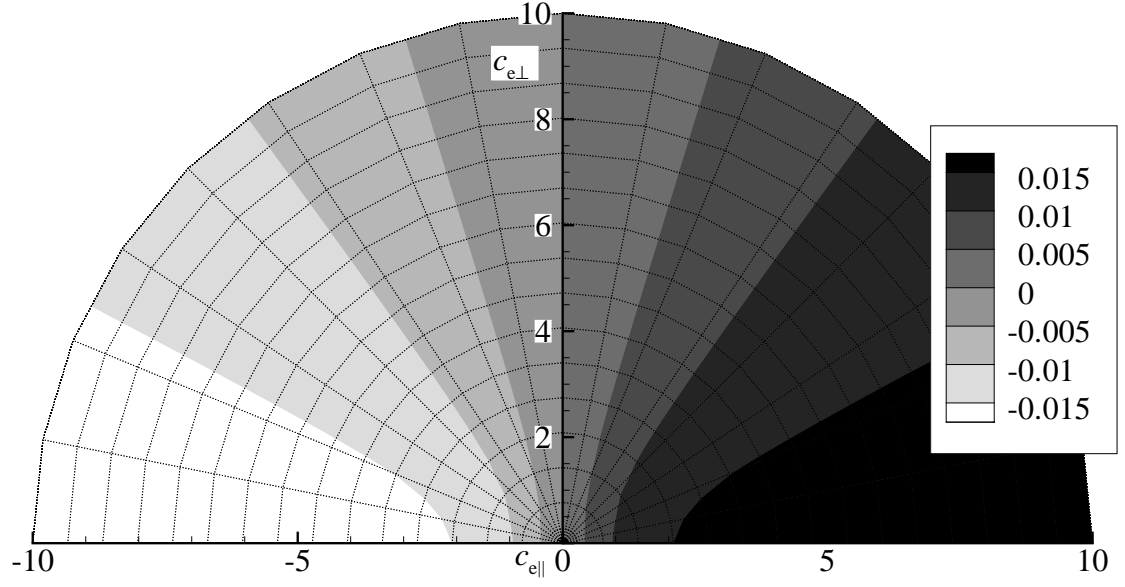


Fig. A.9: Contour plots of parallel component of $\nabla_{\mathbf{c}_e} \bar{g}_e^M$, defined in Eq. (5.14).

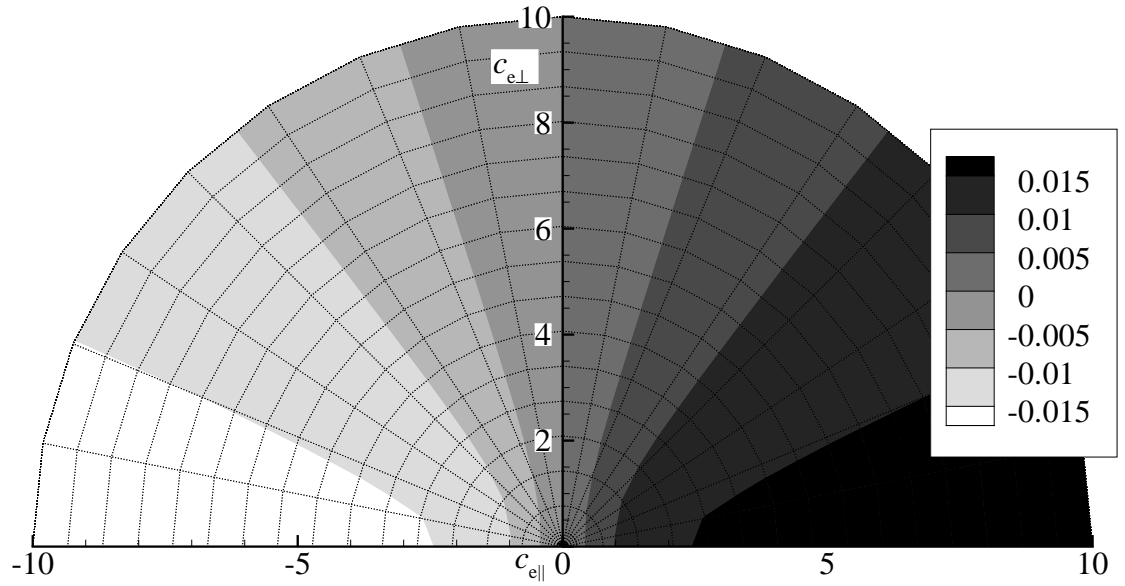


Fig. A.10: Contour plot of parallel component of $\nabla_{\mathbf{c}_e} \bar{g}_e^M$, calculated by our Fokker-Planck code.

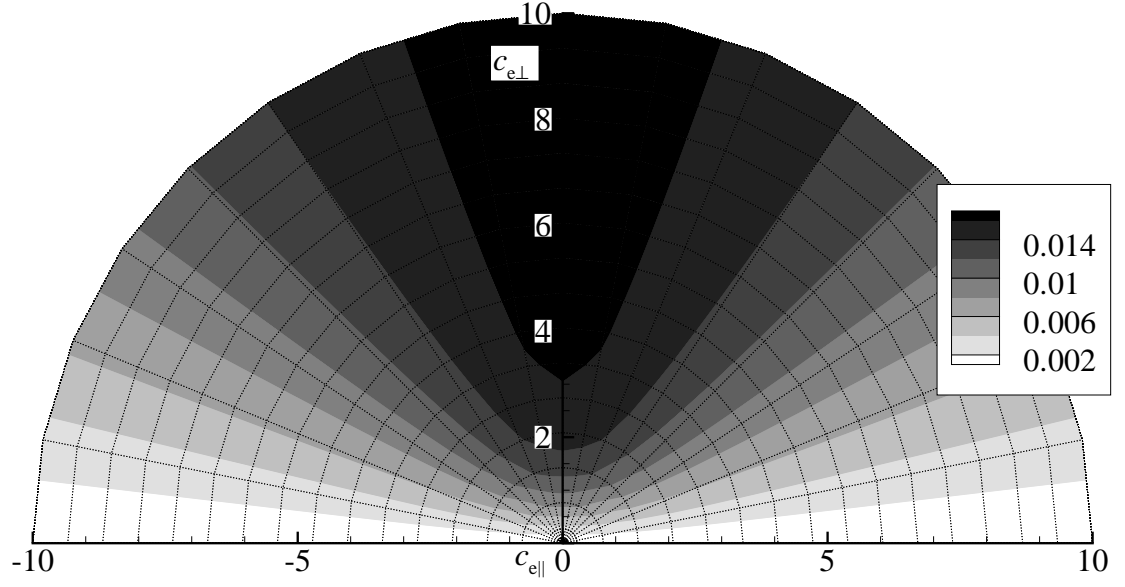


Fig. A.11: Contour plot of perpendicular component of $\nabla_{\mathbf{c}_e} \bar{g}_e^M$, defined in Eq. (5.14).

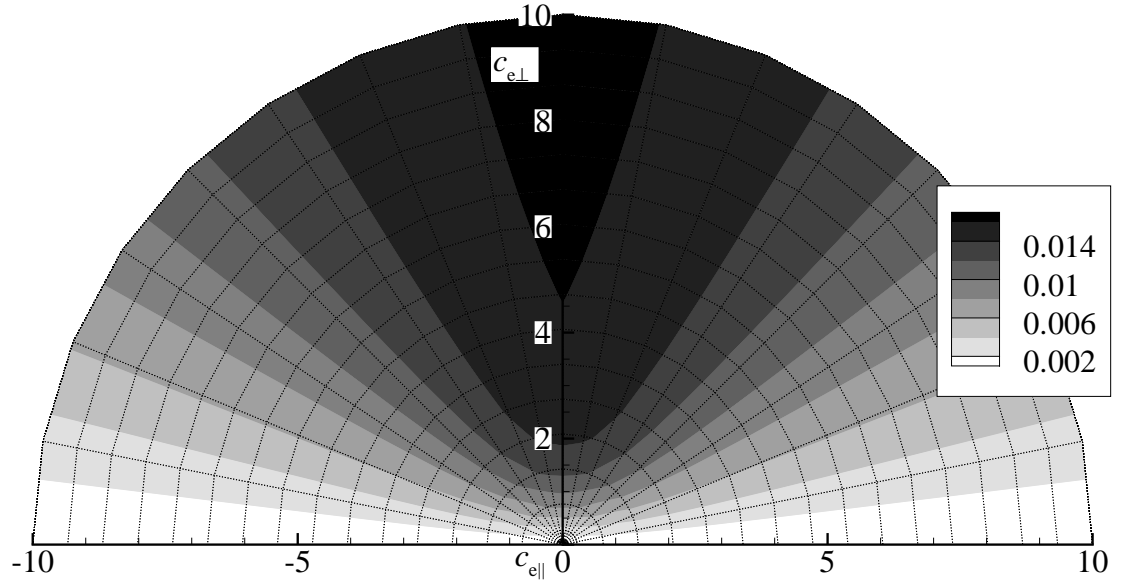


Fig. A.12: Contour plot of perpendicular component of $\nabla_{\mathbf{c}_e} \bar{g}_e^M$, calculated by our Fokker-Planck code.

CURRICULUM VITAE

Joseph Andrew Spencer
(April 2012)

133 W. 1260 S.
Logan, UT 84321

(435) 512-6956
andy.spencer@aggiemail.usu.edu

EDUCATION

Ph.D. (expected 5/12)	Utah State University , Logan, UT Physics. GPA: 4.0 (4.0 = A) Dissertation: <i>A 2D finite element/1D Fourier solution to the Fokker-Planck equation.</i> Major Professor: Eric D. Held
B.S. May 2006	Utah State University , Logan, UT Mathematics. GPA: 3.91 <i>Magna Cum Laude</i>
B.S. May 2005	Utah State University , Logan, UT Physics. GPA: 3.97 <i>Summa Cum Laude</i>

RESEARCH SKILLS

I am currently a graduate student, conducting research with the plasma group in the Dept. of Physics at Utah State University, under the tutelage of Dr. Eric Held since 2008. I have been developing a Fokker-Planck code that utilizes a 2D finite element/1D Fourier series representation of the velocity space distribution function. Our group works on various developments of plasma kinetic theory and codes, which implement those developments. In this position I have familiarized myself with plasma fluid equations, the kinetic, drift-kinetic and gyro-kinetic equations, and corresponding collision operators. Additionally, I am familiar with various analytic and numerical treatments of these equations, including the velocity moment expansion, finite element and Fourier series expansions, finite difference method, and the Legendre polynomial expansion. Most of the analytic work

that has been done by the team has eventually taken some form in the NIMROD code. I have adapted the data structures and subroutines of NIMROD to solve the Fokker-Planck equation for the electron and ion velocity space distribution functions, and have become intimately acquainted with the NIMROD code. Some of the technical skills I use on a daily basis are writing parallel FORTRAN code including MPI calls, building complex code using autotools and the make utility, and working in LYX to write down all of my analytic calculations.

Prior to working in plasma physics, I did research with Dr. James Wheeler in the high energy field theory group in the same department. I became familiar with general relativity, gauge theory, and conformal field theory. My focus was studying a class of geometries with Lorentz and conformal symmetry, called biconformal spaces, their connection to quantum gravity and the emergence of time as a unique dimension.

This combination of analytical and computational skills, as well as my breadth of knowledge in physics and mathematics, enable me to carry out cutting-edge research in almost any physics discipline. Additionally, the time I have spent teaching and tutoring has made me a skilled communicator.

TECHNICAL SKILLS

Operating Systems	Linux, Mac, Windows	Programming	FORTRAN 90, C/C++, MPI, SVN, Autotools, make, Shell scripting, HTML
Scientific Computing	NIMROD, Maple, Tecplot, NERSC	Typography	L ^A T _E X, L ^Y X

EMPLOYMENT

Jan. 2010 - current	Graduate Student Research Assistant , <i>Utah State University</i> . Reference: Eric Held. Studying plasma kinetic theory with the plasma physics group; writing code for plasma simulations.
Aug. 2007 - May 2011	Graduate Student Teaching Assistant , <i>Utah State University</i> . Teaching recitation sections and labs, and tutoring for the introductory physics class.
Fall 2010	Tutor , <i>Utah State University</i> . Reference: Karalee Ransom. One-on-one tutoring a student in the graduate level classical mechanics class.
Summer 2009	Instructor , <i>Utah State University</i> . Reference: Karalee Ransom. Instructing the introductory physics class.
May 2007 - May 2009	Tutor , <i>Utah State University, UBBC</i> . Reference: Patricia Hayes. Tutoring trigonometry and calculus students over the Distant Education satellite system.
Summer 2008	Continuing Education Instructor , <i>Utah State University</i> . Reference: Eric Rowley. Instructing a pre-algebra class.
2006 - 2007	Graduate Research Fellow , <i>Utah State University</i> . Reference: James T. Wheeler. Awarded the Vice President of Research Graduate Research Fellowship for research in biconformal field theory.
2005 - 2006	Undergraduate Research Fellow , <i>Utah State University</i> . Reference: James T. Wheeler. Awarded the Willard L. Eccles Undergraduate Research Fellowship for research in biconformal field theory.
2005 - 2006	Mathematics Grader , <i>Utah State University</i> . References: Ian Anderson & LeRoy Beasley. Grading assignments in differential geometry, ordinary differential equations and cryptography.
2004 - 2005	Undergraduate Teaching Fellow , <i>Utah State University</i> . Reference: David Peak. Substitute teaching and grading classical mechanics and modern physics classes.
2003 - 2004	Atmospheric Lidar Observatory , <i>Utah State University</i> . Reference: Vincent Wickwar. Operating the Lidar and creating the group's website.
2003 - 2004	Laboratory Instructor , <i>Utah State University</i> . Reference: Charles Torre & Mark Riffe. Instructing laboratory sections for the introductory physics class.

HONORS

- W. Farrell Edwards Award
- VP for Research Graduate Fellow
- Eccles Undergraduate Teaching Fellow
- National Deans List
- Golden Key Int'l Honour Society
- $\Sigma\Pi\Sigma$
- $\Phi K \Phi$
- USU College of Science Scholarship
- Seely-Hinckley Scholarship
- National Society of Collegiate Scholars

PUBLICATIONS

2012
(under review)

A Finite Element/Fourier Treatment of the Fokker-Planck Equation.

J.A. Spencer, E.D. Held, J-Y. Ji, under review at the *Journal of Computational Physics*.

I was the primary author of this paper, writing the code and performing the calculations referred in the paper under the direction of Dr. Eric Held. I also wrote the text with the guidance and editorial contributions of the other authors.

2011

The Existence of Time.

J.T. Wheeler, J.A. Spencer, *International Journal of Geometric Methods in Modern Physics*, 8 (2011), 273-301.

I performed all of the calculations that make up the theoretical results of this paper parallel to the primary author, contributed portions of and edited the text, and was involved with the review and revision process.

CONTRIBUTED WORKS

- 2011: Talk **A 2D FE + 1D Fourier Treatment of the Fokker-Planck Equation.**
NIMROD meeting at APS-DPP, Salt Lake City, Utah, 2011.
- 2011: Talk **Adapting NIMROD to solve the Fokker-Planck Equation.**
NIMROD Summer meeting, Logan, Utah, 2011.
- 2010: Poster **Novel Numerical Solution to the Plasma Kinetic Equation.**
APS 4CS meeting, Utah State University, 2010.
- 2009: Poster **Novel Numerical Solution to the Plasma Kinetic Equation.**
APS 4CS meeting, Colorado School of Mines, 2010.
- 2006: Essay **Closing a Loophole in Time.**
Submitted to FQXi: The Nature of Time Essay Contest, Dec. 2006.
- 2005: Talk **Biconformal Yang-Mills Gravity.**
APS 4CS meeting, University of Colorado, Boulder, 2005.
- 2005: Poster **Biconformal Yang-Mills Gravity.**
USU Student Showcase, Utah State University, 2005.